UNIVERSITY
OF LATVIA

FACULTY OF PHYSICS, MATHEMATICS AND OPTOMETRY

Andrejs Česnokovs

The effect of point defects and their local structure on the conductivity of wide-gap materials: cases of CeO_2 and ZnO

A thesis presented for the Doctoral degree in physics
Subfield of Solid state physics

Riga
2023

The doctoral thesis was carried out at the Institute of Solid State Physics, University of Latvia from 2016 to 2023.
The thesis contains the introduction, four chapters, conclusions and thesis, reference list.
Form of thesis: dissertation in Physics and Astronomy, subfield of solid state physics.

Scientific supervisor:

Dr. Rer. Nat. Deniss Grjaznovs, senior researcher of the Laboratory of kinetics in self-organizing systems at Institute of Solid State Physics, University of Latvia.

Reviewers:

1. *D. Sc. (Tech.)* **Andris Guļāns**, University of Latvia
2. *Dr.* **José Serra**, Technical University of Valencia, Spain
3. *Dr.* **Mikhail Brik**, University of Tartu, Estonia

The thesis will be defended at the public session of Doctoral Committee of Physics, Astronomy and Mechanics, University of Latvia at 15:00 on Thursday, 16 November 2023, in the conference hall at the Institute of Solid State Physics, University of Latvia.

The doctoral thesis and its summary are available at the Library of the University of Latvia (Kalpaka blvd 4., Riga) and Latvian Academic Library (10 Rupniecibas Str, Riga).

Chairman of the Doctoral Committee *Dr. phys.* **Anatolijs Šarakovskis**
Secretary of the Doctoral Committee **Sintija Siliņa**

ABSTRACT

Conductivity is a very broad term, used to describe a material's capacity to transport various objects – electrons, holes, ions, atoms, deformations, excitations, – through itself via some mechanism. It is an intrinsic property of any material and is affected by the material's composition and structure. Subtle changes in either can have a profound impact on conductivity and understanding this causality is vital to material design.

In this thesis two multifunctional materials, cerium dioxide (CeO_2) and zinc oxide (ZnO) are studied with density functional theory (DFT) methods. Both materials are known for their response to point defects, such as the formation of vacancies, or introduction of substitution defects: CeO_2 is a model material for small polaron conductivity, which is heavily impacted by oxygen vacancy formation, while ZnO is a well-known n-type semiconductor, with possibly untapped potential for p-type conductivity. At the root of this thesis is the development of robust, traceable, transparent computational models for tracking changes in local structure and electronic localization, and assessing their effects on the conductivities of these materials.

The work presented in this thesis shows how to build a causal link between experimentally observed data and computed properties of CeO_2 and ZnO. It is shown how to apply symmetry analysis in order to get all possible electronic localization solutions. An example of statistical thermodynamics coupled with DFT calculations is shown to yield predictions of dopant solubility. The ability to create experimentally grounded models such as those shown in this thesis is an important aspect of the material design process.

ANOTĀCIJA

Vadāmība ir visaptverošs termins, kuru pielieto lai aprakstītu materiāla spēju pārvietot, izmantojot kādu vadāmības mehānismu, dažādus objektus: elektronus, elektroniskus caurumus, jonus, atomus, deformācijas, ierosinājumus. Šī ir jebkura materiāla īpatnēja spēja, un ir atkarīga no materiāla sastāva un struktūras. Pat nelielas izmaiņas jebkurā no šiem parametriem var manāmi ietekmēt vadāmību, tāpēc izpratne par šo cēlonību ir svarīga materiālu inženierijā.

Šajā darbā, pielietojot blīvuma funkcionāla teorijas (DFT) metodes, tiek pētīti divi daudzfunkcionāli materiāli: cērija dioksīds (CeO_2) un cinka oksīds (ZnO). Abi materiāli ir pazīstami ar savām reakcijām uz punktveida defektiem, tādiem kā vakanču izveidošanās, vai aizvietošanas defektu ievešana: CeO_2 ir paraugmateriāls mazā rādiusa polaronu vadītspējai, kuru stipri ietekmē skābekļa vakanču izveide, savukārt, ZnO ir labi pazīstams n-tipa pusvadītājs ar potenciāli neizsmeltu p-tipa vadāmību. Šī darba pamatā ir robusto, izsekojamo, pārskatāmo skaitlisko modeļu izstrāde un to pielietošana ar mērķi izsekot izmaiņas lokālā struktūrā un elektronu lokalizācijā un novērtēt to efektu uz materiālu vadāmību.

Šis darbs parāda, kā izveidot cēloņsakarību starp eksperimentāli novērotiem datiem un pētamo materiālu aprēķinātām īpašībām. Ir parādīts, kā pielietot simetrijas analīzi lai atrastu visus iespējamus atrisinājumus elektronu lokalizācijai. Ir sniegts piemērs DFT aprēķinu apvienošanai ar statistisko termodinamiku, lai dabūtu prognozi par piemaisījuma šķīdību. Spēja izveidot eksperimentāli pamatotus modeļus, līdzīgus šajā darbā izmantotiem, ir materiālu izstrādes procesam svarīgs aspekts.

CONTENTS

LIST OF ABBREVIATIONS

Abbreviations

AO	Atomic orbital
$ca.$	Circa
CO	Crystalline orbital
CW	Concentration wave
DFT	Density functional theory
DOS	Density of states
$EXAFS$	Extended x-ray absorbtion fine structure
fcc	Face-centred cubic
GGA	Generalized gradient approximation
GTF	Gaussian type function
HF	Hartree-Fock
HSE	Heyd-Scuseria-Ernzerhof [exchange-correlation functional]
KS	Kohn-Sham
LDA	Local density approximation
LRO	Long range order
OS	Oxidation state
PAW	Projector-augmented wave
PBE	Perdew-Burke-Ernzerhof [exchange-correlation functional]
RSH	Range-separated hybrid [exchange-correlation functional]
SCF	Self-consistent field
SIE	Self-interaction error
$TZVP$	Valence triple-zeta polarization [basis set]
$w.r.t.$	With respect to
XC	Exchange-correlation [functional]

LIST OF FIGURES

LIST OF TABLES

1.INTRODUCTION

1.1 General introduction and motivation

Conductivity, colloquially and broadly, is a material's innate ability to transport charge carriers. In solids specifically, charge carriers can be ions, electrons, or holes (a hole is a quasiparticle associated with the absence of an electron where it would normally be in an atom or atomic lattice). Material's dominant conducting mechanism defines its utility and application limits. Thus, materials with very high electronic conductivity are best suited for transmitting power or signals in the form of electrical flow, materials with very low electrical conductivity are best at separating the flow of electrical power from places it is not supposed to reach, materials whose conductivity depends on external conditions such as temperature or potential, are optimal for controlling the flow of energy, and materials with ionic conductivity mechanisms are suited for energy conversion.

Being an innate ability of the material, conductivity is affected by its composition and structure. For instance, pure water does not conduct electricity, but the addition of table salt makes it conductive, and carbon nanotubes, while having the same atomic constitution, may or may not conduct electrical current depending on their geometry [1]. This work is devoted to predicting the behaviour of point defects from the first-principles calculations.

Point defects are crystallographic defects that occur only at or around a single lattice point. While crystals are infinitely periodical in all directions, point defects do not extend in either dimension. In this work, three types of defects are investigated:

- vacancy defects, which are lattice sites that are normally occupied, but are empty;
- substitution defects, i.e. atoms of different chemical species (impurity or a dopant) occupying a regular lattice site;
- interstitial defects, or atoms that occupy a regular lattice position which is normally vacant.

Formation of these defects changes the distribution of electronic density and introduces distortions to the crystalline structure such as changes in bond lengths and atomic positions. Crucially, these changes do not propagate indefinitely in the crystalline structure, and as such their description can be contained to a relatively small-radius region (in comparison to the infinite crystal), i.e. to a local structure of the defect. This work explores point defects and their impact on conductivity in two materials with different conductivity modes and different applications.

The first material is cerium dioxide, CeO_2 (chapter 4), which is a wide-gap semiconductor, but also an ionic conductor, whose ionic conductivity depends on the energetics of oxygen vacancy formation. This work explores symmetry aspects of this defect and its effect on the material's surroundings, specifically, the localization of electrons and the associated magnetic properties, and provides a theoretical background for the observed small polaron formation. Another principal defect of interest is the cerium-substituting terbium (Tb) ion. Not only are lanthanides known to improve electronic and ionic conductivities of CeO_2 (see section 3.1), but Tb specifically has very promising solubility thermodynamics (see section 4.3.5). Tb's presence drastically lowers energetics of oxygen

vacancy formation (section 4.3.6), thus improving CeO_2's ionic conductivity.

The second material of interest is zinc oxide, ZnO (chapter 5), also a wide-gap semiconductor, and a very promising material for transparent electronics, among its numerous other applications (section 3.2). This work explores whether the presence of Ir–O complexes may cause a measurable p-type conductivity in this material, and what are the associated structural changes when these complexes are created in ZnO.

1.2 Aim and objectives of the work

The **aim** of this study is to explore and explain, using first-principles quantum chemistry calculations, the relationship between local and electronic structures of point defects in wide-gap materials such as CeO_2 and ZnO, and their conductivities–ionic, in the case of CeO_2, and electronic in the case of ZnO.

The **objectives** of the study are

- to develop robust, valid, and experimentally grounded computational models for analysing point defects in CeO_2 and ZnO;
- to perform calculations and gather data on point defects in CeO_2 and ZnO;
- to analyse the obtained data to interpret how changes in structure impact electronic distribution in the studied materials;
- to put forward a model that explains the emergence of observed properties in the studied materials.

1.3 The scientific novelty of the work

The results of research presented in this thesis are of scientific novelty and have been published in several international journals.

This study is among the first to use a site-symmetry approach to model polaronic and magnetically ordered point defects in CeO_2.

The solubility of Tb in CeO_2 for the entire range of Tb concentration has been predicted for the first time.

It was demonstrated that the computationally cost-effective PBE+U approach allows for exploring the localization of electronic defects and describing reduced lanthanide cations in a highly ionic environment.

A theoretical model for the phenomenon of emergent p-type conductivity in Ir-doped ZnO has been proposed.

1.4 Author's contribution

Data acquisition and analysis using a range of computational tools was performed by the Author at the Institute of Solid State Physics, University of Latvia (ISSP, UL). First-principles calculations have been carried out by the Author with the computational resources provided by LASC (Riga, Latvia), the HPC centre of Max Planck Institute for solid state research (Stuttgart, Germany), and PDC Center for High-Performance Computing at KTH (Stockholm, Sweden). Interpretation of the

obtained results was performed in collaboration with the supervisor.

During the course of this study, the Author has submitted and completed a research project under the HPC-Europa3 initiative called "First Principles Calculations of Dopants in Transparent Conducting Oxide ZnO-based Thin Films". The project was carried out in KTH (Stockholm, Sweden), its results are included in this Thesis and have been published as a paper in a peer-reviewed journal.

The Author has participated in 4 international schools during 2016-2023. The results of the research have been presented at 8 international conferences and workshops. During the preparation of this thesis, Author has contributed to 9 published peer-reviewed papers. The main results of this thesis have been published in 4 papers, and the Author is the first contributor to 2 of them. At the time of writing, Author's h-index is 4.

[A1] R. A. Evarestov, D. Gryaznov, M. Arrigoni, E. A. Kotomin, **A. Chesnokov**, and J. Maier, "Use of site symmetry in supercell models of defective crystals: Polarons in CeO_2", Phys. Chem. Chem. Phys. **19**, 8340–8348 (2017). The author has performed basis optimisation calculations for Ce and O, calculations of CeO_2 (both with- and without oxygen vacancy), has gathered the data and has contributed his writing to the paper.

[A2] D. Fuks, D. Gryaznov, E. Kotomin, **A. Chesnokov**, and J. Maier, "Dopant solubility in ceria: Alloy thermodynamics combined with the DFT+U calculations", Solid State Ion. **325**, 258–264 (2018). The author has performed most calculations of cerium and terbium oxides, has contributed text and figures to the paper.

[A3] **A. Chesnokov**, D. Gryaznov, and E. Kotomin, "First principles calculations on CeO_2 doped with Tb^{3+} ions", Opt. Mater. **90**, 76–83 (2019). The author has conducted all calculations on Tb-doped CeO_2, has conducted all calculations of all oxides related to parametrisation and validation of the model, has gathered the data, has contributed texts and figures to the paper, beginning with the original draft.

[A4] **A. Chesnokov**, D. Gryaznov, N. V. Skorodumova, E. A. Kotomin, A. Zitolo, M. Zubkins, A. Kuzmin, A. Anspoks, and J. Purans, "The local atomic structure and thermoelectric properties of Ir-doped ZnO: Hybrid DFT calculations and XAS experiments", J. Mater. Chem. C. **9**, 4948–4960 (2021). The author has conducted all calculations related to parametrisation and validation of the model, has conducted calculations of all systems and all properties, has gathered and interpreted all data, has prepared figures and the first draft of the paper.

2.THEORY

2.1 Crystallography fundamentals

By a textbook definition, a crystal is periodic structure created by infinitely repeating identical groups of atoms (a motif) across some lattice [2]. One way to define a lattice in three dimensions is by three vectors a_1, a_2, a_3 such that the arrangement of atoms does not change when an arbitrary point $\mathbf{r}$ is translated by an arbitrary integral multiple of these vectors:

$$r' = r + u_1 a_1 + u_2 a_2 + u_3 a_3 \tag{2.1}$$

All possible integer values of u_i define the set r', or the lattice. Equally, a crystal is invariant under any translation $\mathbf{T}$ of the form

$$\mathbf{T} = u_1 a_1 + u_2 a_2 + u_3 a_3, \tag{2.2}$$

and so are all the local physical properties of the crystal, such as the charge concentration, average electron density, magnetic moment density, and so on. Vectors a_1, a_2, a_3 form the crystallographic basis of the direct lattice. These primitive translations $\mathbf{T}$ form an invariant subgroup of every crystallographic space group. This group is of utmost importance, because from it the Brillouin zone is derived, which determines crystalline energy levels.

A parallelepiped built on the vectors a_1, a_2, a_3 is the unit cell of a crystal. The International Union of Crystallography distinguishes in the *International Tables for Crystallography* [3] the *unit* cell, the *conventional* cell, and a *primitive* cell:

- Primitive cell is a unit cell built on the primitive basis vectors. Primitive cell contains only one lattice point, and its volume is equal to the triple scalar product: $a_1 \cdot (a_2 \times a_3)$.
  - If the basis is non-primitive, the unit cell is a multiple cell and it contains more than one lattice point. Non-primitive bases are used conventionally to describe centred lattices[1]. The multiplicity of the cell is given by the ratio of its volume to the volume of a primitive cell.
- Conventional cell can be defined for each lattice and must obey the following conditions:
  - its basis vectors define a right-handed axial setting;
  - its edges are along symmetry directions of the lattice;
  - it is the smallest cell compatible with the above condition.

Figure 2.1 shows difference between the primitive and conventional cell using CeO_2 as an example. CeO_2 crystal has fluorite structure (space group No. 225, $Fm\bar{3}m$, face-centred cubic lattice), and its conventional cell is also face-centred cubic. It has 4 lattice points, and as such it has 4 Ce atoms, and 8 O atoms. The primitive cell, on the other hand, is trigonal (sometimes called rhombohedral): each pair of its basis vectors forms a 60° angle, and all vectors have the same length. Figure 2.2 shows a way for constructing a primitive cell from the CeO_2's conventional cell.

[1] A lattice being an infinite, symmetric and periodic collection of zero-dimensional nodes, is neither primitive nor centred. The expression *centred lattice* should be interpreted as "lattice whose conventional cell is centred" [4].

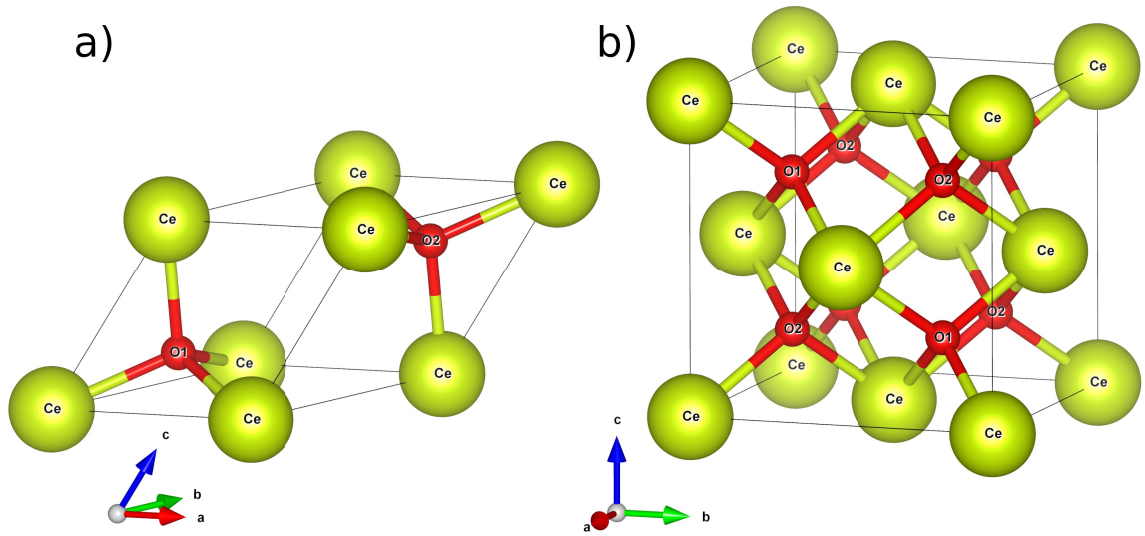

Figure 2.1: Primitive (a) and conventional (b) cells of CeO_2. Primitive cell has 1 Ce atom and 2 oxygen atoms. Conventional cell has 4 symmetrically equivalent Ce atoms (all occupying the same Wyckoff position with multiplicity 4), and 8 symmetrically equivalent O atoms (occupying a Wyckoff position with multiplicity 8, different numbers are for clarity)

The finite list of all symmetry operations which leave the given point invariant taken together make up another group, which is known as the site symmetry group of that point. By definition, all points with the same site symmetry group (or a site symmetry group in the same conjugacy class) are assigned the same Wyckoff position [3]. A related but not strictly synonymous concept is that of crystallographic orbit, which is a set of all points generated from any given point in space by action of the space group. Two crystallographic orbits of a given space group belong to the same Wyckoff position if and only if the site-symmetry groups of any two points from the first and the second orbit are conjugate subgroups of the space group. By convention, each Wyckoff positon of a space group is labelled by a letter which is called the Wyckoff letter. The number of different Wyckoff positions of each space group is finite, the maximal numbers being 9 for plane groups (realized in $p2mm$) and 27 for space groups (realized in $Pmmm$). Letters closer to beginning of the alphabet correspond to positions with higher site symmetry. In case of the group $P1$ the *only* position a is the general position, and in the case of $Pmmm$ the 27^{th} position (also the general position) is assigned the letter A [3, 5].

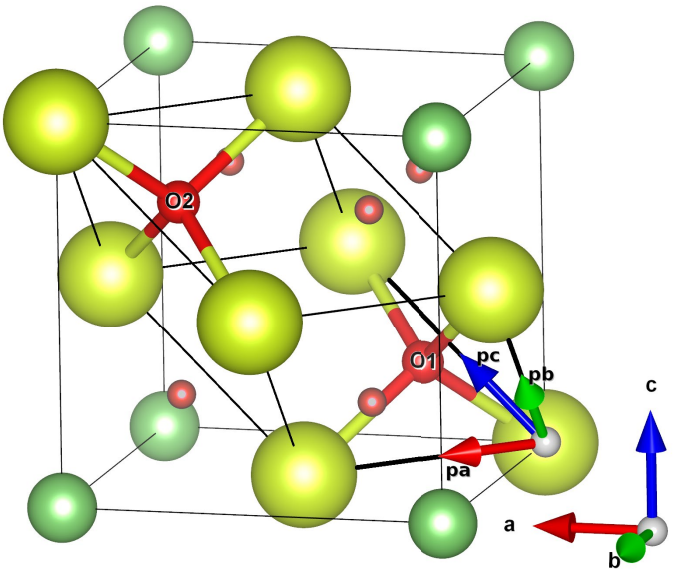

Figure 2.2: Relation between CeO_2's conventional cell (with *a, b, c* basis) and a primitive cell (with *pa, pb, pc* basis). All red spheres represent oxygen atoms, with labelled atoms belonging to the primitive cell; all other spheres represent Ce atoms, with larger ones belonging to the primitive cell

2.2 Supercell model and splitting of Wyckoff positions

Supercell model is an excellent tool for modelling point defects in crystalline solids. A point defect cannot be introduced into the unit cell because then the concentration of the defect will be too high, at which point it will no longer be a point defect, but an entirely new material, or some exotic phase. The concept of a supercell has been introduced in a work by A. M. Dobrotvorskii and R. A. Evarestov [6, 7], and initially was named the *quasi-molecular large unit cell model*. In a nutshell, the idea of this approach is to expand the motif, effectively replacing the unit cell with a larger fragment of the crystal, corresponding to a practical concentration of the studied defect. This larger fragment, created with the same translational symmetry as the parent crystal, is the supercell, which, when combined with periodic boundary conditions, represents the entire crystal with its defects. A later work by Evarestov and Smirnov [8] lists for each crystal class transformations that generate the most symmetrical supercells with regards to both direct and inverse lattices.

Contrary to naïve intuition, atoms of the same chemical species in the supercell are not necessarily identical by symmetry, even though they originate from identical atoms of the unit cell. Consider an example of CeO_2 (figure 2.3). Two transformations of its basis vectors keep the full symmetry of its space group [8], one is isotropic expansion:

$$\begin{bmatrix} n & 0 & 0 \\ 0 & n & 0 \\ 0 & 0 & n \end{bmatrix}, \tag{2.1}$$

and the other is a transformation from face-centred cubic cell to primitive cubic cell with an isotropic

expansion:

$$\begin{bmatrix} -n & n & n \\ n & -n & n \\ n & n & -n \end{bmatrix}. \tag{2.2}$$

Both transformations yield cells with the same number of symmetry operations, yet divide all Ce atoms into those with high point symmetries (in the fig. 2.3 b&c these are positions a and b, belonging to the O_h point group), and those with low symmetry (in the same figure, positions d and c, with point groups D_{2h} and D_{4h} respectively). O atoms have a different splitting pattern: in the same space group (fig. 2.3 b) oxygens are split into two groups, each belonging to the Wyckoff position f (point group C_{3v}), while in a different space group (fig. 2.3 c) all oxygens belong to the same Wyckoff position g (point group C_{3v}).

This loss of symmetry equivalence is called splitting of symmetry orbits, and it is governed by group-subgroup relations. Several papers by Wondratschek *et al.* provide mathematical foundation to this phenomenon [9, 10]. They describe a generalized case of group-subgroup relations that may occur as a result of structural changes in crystals caused by chemical interactions or continuous phase transitions.

In the realm of supercell model, because creation of a supercell replaces the primitive crystallographic motif with a larger one, the crystallographic pattern is distorted. By definition, the symmetry group of a crystal pattern is its space group, so the symmetry group of a different crystal pattern (supercell) is some subgroup of the parent space group. Practically it means that supercells cannot have more symmetry operations than the primitive cell, but they can have fewer symmetry operations. Consequently, since creation of a supercell can change the point group of the space group (figure 2.3 C), points of the new supercell can also have fewer associated symmetry operations, and hence may be assigned new Wyckoff positions.

As a result, within the supercell model, creation of a supercell may move the same atomic species to different Wyckoff positions, making them symmetrically inequivalent. This has huge implications for modeling point defects, especially substitution defects, because, if accounted for, local site symmetry influences the distribution of electronic density, effectively allowing or disallowing certain localisation of electrons, affecting possible magnetic orientations, etc. Specifically, results obtained in chapter 4 rely heavily on this concept.

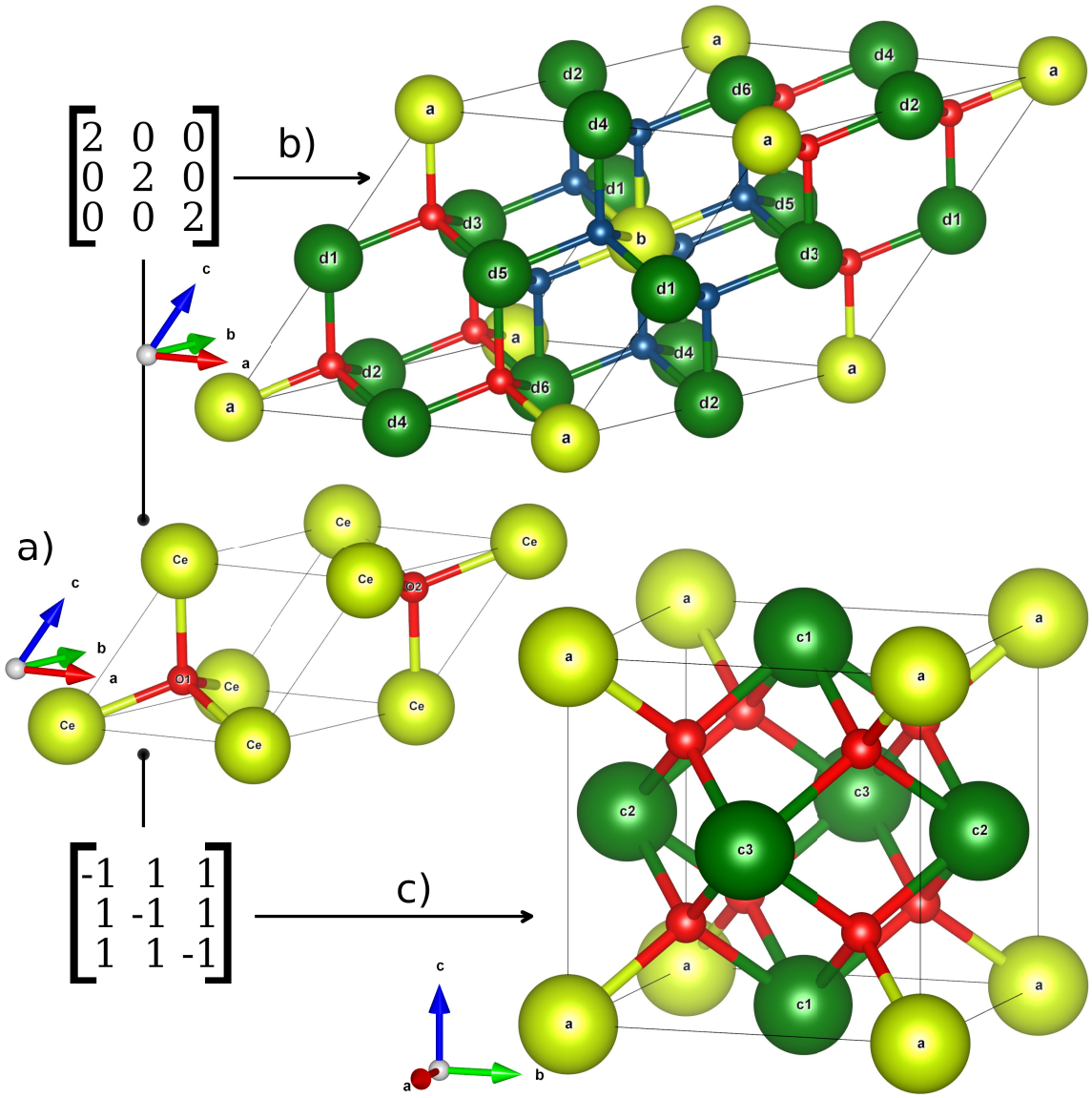

Figure 2.3: Splitting of Wyckoff positions in some CeO_2 supercells.
a: primitive cell.
b: $2 \times 2 \times 2$ (L8) supercell. Light green sites are high-symmetry Ce sites (Wyckoff positions a and b), dark green sites are low-symmetry Ce sites (Wyckoff position d), red and blue spheres represent symmetrically inequivalent O sites belonging to the doubly degenerate Wyckoff position f.
c: mapping of the primitive cell to the conventional $1 \times 1 \times 1$ (L1) cell, or, equivalently, mapping of the space group No. 225 to the space group No. 221 ($Fm\bar{3}m \rightarrow Pm\bar{3}m$); light green spheres are high-symmetry Ce sites (Wyckoff position a), dark green spheres are low-symmetry Ce sites (Wyckoff position c), red spheres are oxygen sites (Wyckoff position g)

2.3 Basics of DFT approximation

In this work, the electronic structure is calculated from first principles by using the fundamental Schrödinger equation along with a set of approximations. Unless specified otherwise, the principal approximation is the use of Density Functional Theory (DFT). Dozens of books as well as every other thesis—bachelor's, master's and doctor's,—cover theoretical foundations of DFT from every possible angle. For a brief summary, in the Kohn-Sham (KS) formulation of DFT, the total energy is given by

$$\begin{aligned} E_{tot}^{KS-DFT} = & -\frac{1}{2}\sum_i \int \psi_i^*(\mathbf{r})\nabla^2\psi_i(\mathbf{r})d^3r && \text{non-interacting kinetic energy of electrons} \\ & -\sum_A \int \frac{Z_A}{|\mathbf{r}-\mathbf{R}_A|} n(\mathbf{r})d^3r && \text{electrons-nuclei attraction energy} \\ & +\frac{1}{2}\iint \frac{n(\mathbf{r})n(\mathbf{r}')}{|\mathbf{r}-\mathbf{r}'|} d^3r d^3r' && \text{classical Coulomb electron-electron repulsive energy} \\ & + E_{xc} && \text{–exchange-correlation energy} \\ & +\frac{1}{2}\sum_{A\neq B} \frac{Z_A Z_B}{|\mathbf{R}_A-\mathbf{R}_B|} && \text{nuclei-nuclei repulsion energy.} \end{aligned} \tag{2.1}$$

The orbitals ψ_i and the electron density $n = \sum_i |\psi_i|^2$ that are used to evaluate E_{tot} are obtained by solving self-consistently the KS equations

$$\left(-\frac{1}{2}\nabla^2 - \sum_A \frac{Z_A}{|\mathbf{r}-\mathbf{R}_A|} + \int \frac{n(\mathbf{r}')}{|\mathbf{r}-\mathbf{r}'|} d^3r d^3r' + v_{xc}(\mathbf{r})\right)\psi_i(\mathbf{r}) = \epsilon_i\psi_i(\mathbf{r}) \tag{2.2}$$

The only terms in E_{tot} and in the KS equations that are not known exactly are the exchange-correlation energy functional E_{xc} and potential $v_{xc} = \partial E_{xc}/\partial n(\mathbf{r})$. Therefore, the accuracy of the calculated properties depends mainly on the approximation used for E_{xc} and v_{xc}.

In this text, the focus is on the practical aspects of using this approximation – as implemented in the Vienna Ab Initio Simulation Package (VASP), and in CRYSTAL17 by University of Torino. The principal difference between these two implementations is in the way they expand the single particle wave functions. In the former, central quantities, like the one-electron orbitals, the electronic charge density, and the local potential are expressed in plane-wave basis sets, an idea that naturally arises when analysing wave equation of electron in a periodic potential [2]. In CRYSTAL17, each "crystalline orbital" (single particle wave function) is expanded as a linear combination of Bloch functions defined in terms of local functions (or atomic orbitals), which, in turn, are linear combinations of Gaussian type functions [11].

2.3.1 Generalized-gradient approximation

The original exchange-correlation approximation of the DFT has been the local density approximation (LDA), which is built on the idea that solids often can be approximated in the limit of a homogenous electron gas, where the exchange and correlation is local [12]. Due to its cost-effectiveness and numerical stability, LDA is a useful and widely adopted approximation. However, there is an important error in the LDA, the incomplete cancellation of the self-interaction term. This self-interaction

error (SIE) means that electrons will effectively "see" themselves, leading to a repulsion that may cause artificial delocalization. For simple cases the error is easily corrected, but the problem becomes very complex for many-particle systems. The effect is especially large in localized systems, such as *d*- or *f*-electron compounds [13].

The success of LDA has inspired development of improved approximations, like the various generalized-gradient approximations (GGAs). The GGA extends the local approximation by using the gradient of the density, Δn, in addition to the density. It was first included as a low-order expansion of the XC energy [14], but this did not lead to an overall enhancement of the LDA. The main issue is that the gradients in real materials are very large, which may cause the gradient expansion to fail. In fact, the "generalized" in the GGA's abbreviation is there to denote all the different methods that modify the behaviour of the functional at large gradients, while preserving functional's desired properties. There are many forms, but the most widely used ones are B88 ("B" is for Becke [15]), PW91 (Perdew and Wang [16]), and PBE (Perdew, Burke and Ernzerhof [17]). One of the most important features of the GGAs is the improvement of binding energies in molecules over the LDA, which has made DFT useful in chemistry. The LDA, on the other hand, typically results in overbinding. However, the GGA has a tendency to underbind crystals.

2.3.2 DFT+U

As stated in section 2.3.1, the LDA (and its spin-inclusive variant, LSDA) may lead to an erroneous ground-state for materials with strongly correlated (localized) electrons, such as *d*- and *f*-electron systems. One way to address this is to introduce a strong intraatomic interaction in a (screened) HF-like manner, as an on-site replacement of the L(S)DA, taking advantage of the fact that the KS orbitals themselves are functionals of the density [18, 19].

In this work, the rotationally invariant approach to DFT+U in the formulation introduced by Dudarev *et al.* [20] is used. This variant of the LSDA+U is of the following form:

$$E_{LSDA+U} = E_{LSDA} + \frac{U-J}{2} \sum_{\sigma} \left[\left(\sum_{m_1} n^{\sigma}_{m_1,m_1} \right) - \left(\sum_{m_1,m_2} \hat{n}^{\sigma}_{m_1,m_2} \hat{n}^{\sigma}_{m_2,m_1} \right) \right], \tag{2.3}$$

that can be understood as adding a penalty to the LSDA total energy expression that forces the on-site occupancy matrix in the direction of idempotency, that is, $\hat{n}^{\sigma} = \hat{n}^{\sigma}\hat{n}^{\sigma}$. Real matrices are only idempotent when their eigenvalues are either 1 or 0, which for an occupancy matrices translates to either fully occupied or fully unoccupied levels. The parameters U and J are not independent, only their difference is meaningful. Those are, respectively, effective Coulomb- and exchange parameters, that can be extracted from LSDA calculations, or even adjusted in a self-consistent manner [21].

2.3.3 Hybrid Functionals

Hybrid functionals intermix exact Hartree-Fock (HF) exchange, E_x^{HF} , with exchange and correlation from functionals like LDA or GGA, hence the name "hybrid". HF theory explicitly accounts for self-interaction and treats exchange exactly, but correlation effects are completely ignored. In the LDA and GGA on the other hand, correlation is fairly well described, so the two techniques complement each other, motivating a combination. Becke realized this [22], and was inspired by the adiabatic

connection formula

$$E_{xc}[n] = \int_0^1 E_{xc,\lambda}[n]d\lambda \tag{2.4}$$

which "connects" the non-interacting KS system ($\lambda = 0$) to the fully interacting real system $\lambda = 1$ through a continuum of systems with partial interaction ($0 \leqslant \lambda \leqslant 1$) which all have the same density n. The term $E_{xc,\lambda}[n]$ contains all the exchange and correlation for any coupling strength λ of electron-electron interaction. This formula is often used for functional development, and Becke used it first to combine LDA and HF in a linear approximation

$$E_{xc}[n] = (1-\lambda)E_x^{HF}[n] + \lambda E_{xc}^{LDA}[n]. \tag{2.5}$$

Inserting this into Equation 2.4 and integrating resulted in the first hybrid functional, the "half-and-half" hybrid functional[22]:

$$E_{xc}[n] = \frac{1}{2}E_x^{HF}[n] + \frac{1}{2}E_{xc}^{LDA}[n]. \tag{2.6}$$

This was later improved by Perdew *et al.* [23], who argued that $1/4$ is the optimal fraction of HF exchange, and introduced the parameter-free PBE0 hybrid functional using the PBE-GGA as a starting point:

$$E_{xc}^{PBE0} = \frac{1}{4}E_x^{HF} + \frac{3}{4}E_x^{PBE} + E_c^{PBE}. \tag{2.7}$$

To generalize, a constant fraction of the HF exchange (A) mixed with some flavour of LDA or GGA exchange and with some correlation functional creates an entire family of the so-called global hybrid (*GH*) functionals, where the portion of HF exchange is distributed evenly among all electronic interactions:

$$E_{xc}^{GH} = (1-A) \times E_x^{DFA} + A \times E_x^{HF} + E_c^{DFA}. \tag{2.8}$$

Notable examples of such functionals are PBE0 (eq. 2.7) [24], B3LYP (Becke's 3 parameter functional, 20% HF, Lee-Yang-Parr correlation functional) [25], B1WC (Wu-Cohen exchange functional, 16% HF exchange, Perdew-Wang GGA correlation functional) [26], WC1LYP (like B1WC, but with LYP correlation functional instead of PWGGA) [11, 27].

The inclusion of HF exchange cancels part of the SIE, improving the description of localized states, but results in a relatively high computational cost. Furthermore, in real materials, the exchange interaction is screened by the electrons, which means that the range of the exchange interaction is overestimated. One way to reduce the cost, while attempting to incorporate screening was proposed by Heyd *et al.* [28]. The nonlocal HF exchange can be range-separated and approximated with good accuracy by the short-range contribution. Heyd *et al.* used the error function $\mathrm{erf}(x)$ and $\mathrm{erfc}(x)$, due to the advantage of simple analytic integration, for the range-separation of the exchange part only of the Coulomb interaction. Heyd's variant of *range-separated hybrid* (RSH) functional used short-range and long-range separation, but in a general case this separation can be even more granular:

$$\frac{1}{r_{12}} = \overbrace{\frac{\mathrm{erf}(\omega_{SR}r_{12})}{r_{12}}}^{\text{short-range}} + \overbrace{\frac{1-\mathrm{erfc}(\omega_{SR}r_{12})-\mathrm{erf}(\omega_{LR}r_{12})}{r_{12}}}^{\text{mid-range}} + \overbrace{\frac{\mathrm{erf}(\omega_{LR}r_{12})}{r_{12}}}^{\text{long-range}}, \tag{2.9}$$

where ω is an adjustable parameter that controls the shape of the separation. This parameter was

empirically optimized for molecules to $\omega = 0.15$, and later for solids by Krukau *et al.* [29] resulting in $\omega = 0.11$. The two forms are known as the HSE03 and HSE06 (Heyd-Scuseria-Ernzerhof) functional, respectively, and may be expressed as

$$E_{xc}^{HSE} = \frac{1}{4}E_x^{HF,SR}(\omega) + \frac{3}{4}E_x^{PBE,SR}(\omega) + E_x^{PBE,LR}(\omega) + E_c^{PBE}, \tag{2.10}$$

or, for a general RSH functional:

$$E_{xc}^{RSH} = E_{xc}^{DFA} + c_{SR}(E_{x,SR}^{HF} - E_{x,SR}^{DFA}) + c_{MR}(E_{x,MR}^{HF} - E_{x,MR}^{DFA}) + c_{LR}(E_{x,LR}^{HF} - E_{x,LR}^{DFA}) \tag{2.11}$$

According to the values of $c_{SR}, c_{MR}, c_{LR}, \omega_{SR}$ and ω_{LR}, short-, middle- and long-range corrected RSH functionals can be defined [11].

2.4 Theoretical background of VASP calculations

In VASP, central quantities, like the one-electron orbitals, the electronic charge density, and the local potential are expressed in plane-wave basis sets. The interactions between the electrons and ions are described using norm-conserving or ultrasoft pseudopotentials, or the projector-augmented-wave method. According to its manual, VASP is a complex package for performing ab-initio quantum-mechanical molecular dynamics (MD) simulations. The approach implemented in VASP is based on the (finite-temperature) approximation with the free energy as variational quantity and an exact evaluation of the instantaneous electronic ground state at each MD time step. VASP uses efficient matrix diagonalization schemes and an efficient Pulay/Broyden charge density mixing. Forces and the full stress tensor can be calculated with VASP and used to relax atoms into their instantaneous ground-state.

The most notable advantages of VASP are:

- a library of highly optimized pseudopotentials that allow accurate description of bulk materials using as few as 50-100 plane waves per atom in a simulation cell;
- an efficient scaling for systems with up to 4000 valence electrons;
- fast numerical methods for evaluating the self-consistent solution of the Kohn-Sham functional.

2.4.1 Electronic groundstate in VASP

Most of the algorithms implemented in VASP use an iterative matrix-diagonalization scheme: the used algorithms are based on the conjugate gradient scheme [30, 31], block Davidson scheme [32], or a residual minimization scheme – direct inversion in the iterative subspace (RMM-DIIS) [33, 34]. For the mixing of the charge density an efficient Broyden/Pulay mixing scheme[34, 35] is used by default, although other approaches are also available. Figure 2.4 shows a typical flow-chart of VASP. Input charge density (ρ_{in}) and wavefunctions (ϕ_{n}) are independent quantities (at the start of a calculation these quantities are set according to user settings, with initial KS orbitals being random (unless precomputed ones are available), and with initial charge density being a superposition of atomic charge densities, unless a precomputed one is available). Within each self-consistency loop the charge density is used to set up the Hamiltonian, then the wavefunctions are optimized iteratively so that they get closer to the exact wavefunctions of this Hamiltonian. From the optimized wavefunctions a

new charge density is calculated, which is then mixed with the old input-charge density.

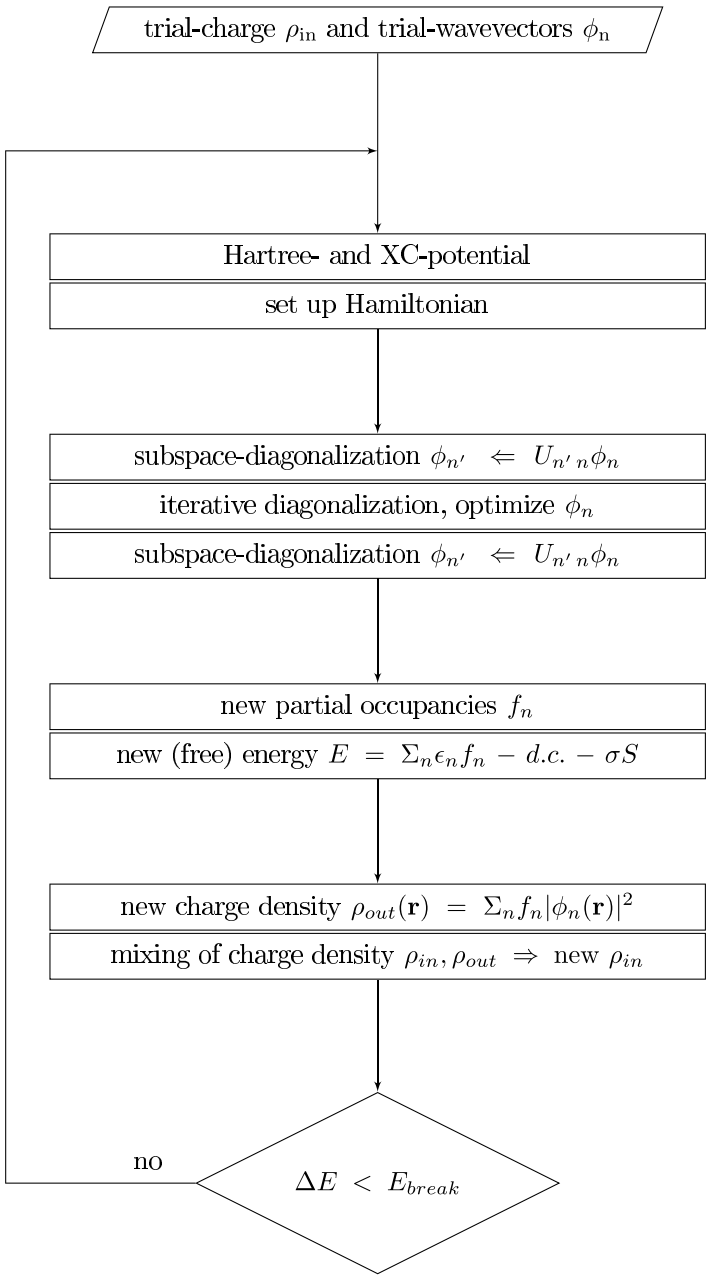

Figure 2.4: Calculation of KS-ground-state in VASP

The accuracy of calculation in general is controlled by several parameters: the maximal kinetic energy of plane wave included in the basis set (largely depends on the pseudopotentials used); grid sizes used for representation of the pseudo orbitals and for localized augmentation charges (in more precise calculations, those are two separate grids defined along lattice vectors, with the augmentation grid being much finer); and by accuracy of projector's representation in real space (the number of grid points within the integration sphere around each ion). The precision of calculation is determined by the self-consistency loop, which is broken when either consistency is reached (relaxation of the electronic degrees of freedom stops if the total energy change and the band-structure-energy change

between two steps are both smaller than a specified threshold), or when a specified number of SCF cycles has passed.

2.4.2 Projector-augmented wave potentials

Felix Bloch's theorem states that solutions to the Schrödinger equation in a periodic potential take the form of a plane wave modulated by a periodic function:

> The eigenfunctions of the wave equation for a periodic potential are the product of a plane wave $\exp(i\mathrm{k}\cdot\mathbf{r})$ times a function $u_{\mathrm{k}}(\mathbf{r})$ with the periodicity of the crystal lattice. [2, 36]

Functions of this form, Bloch functions, therefore, are a natural choice for creating a basis set for the wave functions in crystalline solids. However, wave functions of real materials have very different signatures in different regions of space: in the bonding region the wave function is fairly smooth, while close to the nucleus the wave function oscillates rapidly owing to the large attractive potential of the nucleus. To account for these variations in behaviour, pure plane-wave basis sets need to be very large, including both high-frequency (high energy) waves, and low-frequency functions. Several strategies have been developed to keep the number of functions computationally viable, most notably (and most relevant to VASP), the use of pseudopotentials, that divide the wave function into parts: a partial-wave expansion within an atom-centred sphere and envelope functions outside the spheres. The envelope function is expanded into plane waves or some other convenient basis set. Envelope function and partial-wave expansions are then matched with value and derivative at the sphere radius.

Norm-conserving pseudopotentials were first introduced in 1979 [37]. In this scheme, inside some core radius, the all-electron (AE) wave function is replaced by a soft nodeless pseudo-wave function, with the crucial restriction that the pseudo-wave function must have the same norm as the all-electron wave function within the chosen core radius; outside the core radius the pseudo- and AE wave functions are identical. Good transferability requires a core radius around the outermost maximum of the AE wave function, because only then the charge distribution and moments of the AE wave functions are well reproduced by the pseudo-wave functions. Therefore, for elements with strongly localized orbitals (like first-row, 3d, and rare-earth elements) the resulting pseudopotentials require a large plane-wave basis set. To work around this, compromises are made by increasing the core radius significantly beyond the outermost maximum in the AE wave function. But since the transferability is always adversely affected when the core radius is increased, for any new chemical environment, additional tests are required to establish the reliability of such soft pseudopotentials.

A solution to this problem was proposed by Vanderbilt [38]. In his method, the norm-conservation constraint is relaxed, and to make up for the resulting charge deficit, localized atom-centred augmentation charges are introduced. These augmentation charges are defined as the charge density difference between the AE and the pseudo-wave function, but for convenience they are pseudized to allow an efficient treatment of the augmentation charges on a regular grid. The core radius of the pseudopotential can now be chosen around half the nearest-neighbor distance—independent of the position of the maximum of the AE wave function. Only for the augmentation charges a small cutoff radius must be used to restore the moments and the charge distribution of the AE wave func-

tion accurately. The pseudized augmentation charges are usually treated on a regular grid in real space, which is not necessarily the same as the one used for the representation of the wave functions.

Blöchl's projector-augmented wave (PAW) method was outlined a few years after Vanderbilt's method [39]. He introduces a linear transformation from the pseudo- to the AE wave function and derives the PAW total energy functional in a consistent manner applying this transformation to the KS functional. The construction of PAW datasets is easier because the pseudization of the augmentation charges is avoided, i.e., the PAW method works directly with the full AE wave functions and AE potentials. This is achieved using radial support grids around each atom instead of regular grids. The decomposition into radial grid and regular grid is complete, insofar that no cross term between the grids must be evaluated. PAW method is an exact AE method for a complete set of partial waves. Therefore, the method should yield results that are indistinguishable from any other frozen core AE method. In their work, Kresse and Joubert [40] established the exact formal relationship between both the ultrasoft pseudopotentials and the PAW method.

For the VASP users PAW potentials are available for all elements in the periodic table. These are pseudopotentials for the PAW method and are stored in as external files, separate from other program modules. The distributed PAW potentials have been generated by G. Kresse following the recipes discussed in [40].

2.5 Theoretical background of CRYSTAL calculations

In CRYSTAL, each "crystalline orbital" (CO, a single particle wave function) is expanded as a linear combination of Bloch functions:

$$\psi_i(\mathbf{r};\mathbf{k}) = \sum_{\mu} a_{\mu,i}(\mathbf{k})\phi_\mu(\mathbf{r};\mathbf{k}), \tag{2.1}$$

defined in terms of local functions (or atomic orbitals, AO):

$$\phi_\mu(\mathbf{r};\mathbf{k}) = \sum_{\mathbf{g}} \varphi_\mu(\mathbf{r}-\mathbf{A}_\mu-\mathbf{g})\; e^{i\mathbf{k}\cdot\mathbf{g}}. \tag{2.2}$$

AOs, in turn, are linear combinations of Gaussian type functions (GTF, see below). This approximation is inspired by the Slater-type orbitals (which are analytical solutions of the stationary Schrödinger equation of hydrogen-like atoms), but uses GTFs, which ensures, by virtue of the Gaussian product theorem, that the product of two such orbitals centred on two different atoms is a finite sum of Gaussians centred on a point along the axis connecting them [41], i.e. a two-centre distribution can be replaced by a one-centre distribution, simplifying integration. Analogously, a four-centre integral (which depends on two-centre distributions of two different electrons) is reduced to a two-centre integral, and so on. Although combination of GTFs increases the number of functions and integrals in the calculation, the integrals involving Gaussian functions are quicker to compute than those involving exponentials (Slater-type orbitals), so there is a net gain in the efficiency of the calculation.

The core feature of CRYSTAL that sets it apart from any other computational tool is its handling of space symmetry: 230 space groups, 80 layer groups, 99 rod groups, 45 point groups, and special cases for polymers (helical structures–translation followed by a rotation around the periodic axis),

are automatically applied and used in analysis. This in-depth symmetry-based approach is used not only for generating and analysing geometries, but also in the creation of Bloch functions: when these are created from a basis of local functions, they are symmetry-adapted, drastically reducing computational effort [42, 43].

Output of the program follows optimization steps. Figure 2.5 shows a simple scheme of the optimization process. Each step in figure 2.5 involves calculating energy. From equation 2.1 one can see that 3 out of 5 terms in the KS formulation of energy involve Coulomb interactions, i.e. those of electron-nucleus, electron-electron and nucleus-nucleus, which for a model of a crystalline solid are individually divergent, due to the infinite size of the system. To simplify calculations of these integrals, the program code defines computational thresholds which can be modified by a user.

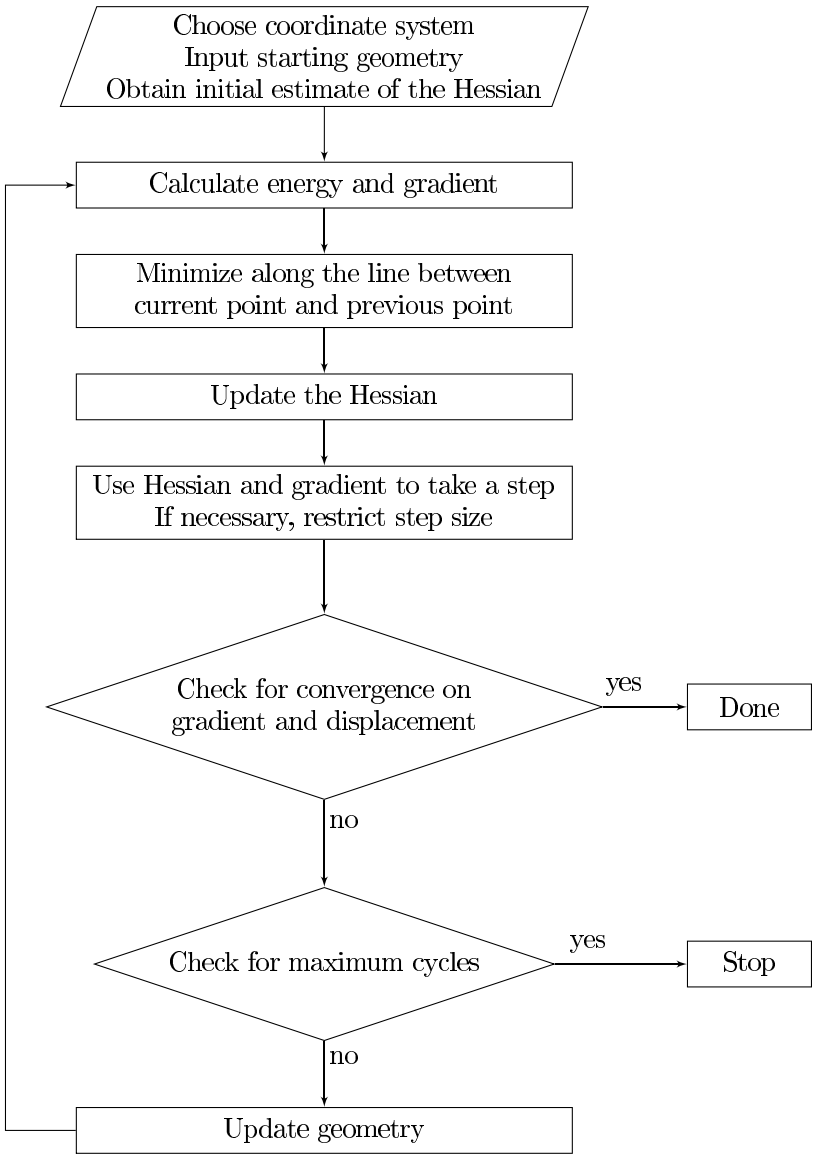

Figure 2.5: Geometry relaxation in CRYSTAL17

Numerical accuracy is controlled by several tolerances for the evaluation of two-electron integrals in the HF reference solution, with five most important parameters. The first is *overlap*

threshold for Coulomb integrals that determines whether overlap between two spatial charge distributions constructed from basis functions is significant enough to calculate. The second parameter, called *penetration threshold for Coulomb integrals*, is based on the distance between two interacting distributions, and divides interactions between charge distribution into exact, short-range or to the approximate, long-range zones. The third parameter is the overlap threshold for HF exchange integrals. The final two parameters exploit the different range of valence and core elements, and truncate summations when their pairwise overlaps are small enough. These two parameters help predicting complicated behaviour of the density matrix elements, in particular in metallic systems when density matrix oscillates.

In summary, the approach adopted for the treatment of the Coulomb and exchange series is based on a few simple ideas and on a few general tools, which can be outlined as follows:

- where possible, terms of the Coulomb series are aggregated so as to reduce the number of integrals to be evaluated;
- exchange integrals which will combine with small density matrix elements are disregarded;
- integrals between non-overlapping distributions are approximated;
- approximations for large integrals must be very accurate; for small integrals large percentage errors can be accepted;
- selection must be very efficient, because a large number of possible terms must be checked (adjoined Gaussians, i.e. single, normalized, s-type GTFs, are very useful from this point of view).

2.5.1 Construction of atomic orbitals in CRYSTAL

Equations 2.1 and 2.2 show how CRYSTAL constructs COs from AOs. The latter are expressed as linear combination of a certain number of Gaussian type functions (GTF):

$$\varphi_\mu(\mathbf{r} - \mathbf{A}_\mu - \mathbf{g}) = \sum_j^{n_G} d_j \, G(\alpha_j; \mathbf{r} - \mathbf{A}_\mu - \mathbf{g}), \tag{2.3}$$

where the sum over μ is limited to the number of basis functions; A is the centre (defined by atomic coordinates), $\mathbf{r}$ is the coordinate of an electron, $\mathbf{g}$ is the direct lattice vector (the sum over $\mathbf{g}$ in eq. 2.2 is extended to all lattice vectors of (periodic) direct lattice), $\mathbf{k}$ is lattice vector defining a point in the reciprocal lattice. Coefficients *a, d* and α are constants defined in the basis set. Coefficients a (eq. 2.1) are variational coefficients for multiplying Bloch functions; d are coefficients of the primitive gaussians in the contraction, fixed for a given basis set (the sum over j is limited to the number of functions in the contraction), and α are the exponents. Large values of α are used to construct narrow GTOs (in the limit of infinite α a GTO approximates the Dirac delta function), i.e. it restricts electron to a small region around the centre (atomic nucleus), while small values of α generate diffuse (spread out) functions, and can describe electrons in chemical bonds (far from the nucleus).

The AOs belonging to a given atom are grouped into shells. The shell can contain either all AOs with the same quantum numbers, n and l (for instance 3s, 2p, 3d shells), or all the AOs with the same principal quantum number n and different l (sp shells; exponents of s and p gaussians

are the same, but their coefficients are different). Table 2.1 illustrates a typical basis set layout, as understood by CRYSTAL. While being technical and specific to CRYSTAL (other software may and does use alternative basis set layouts albeit *information* and its meaning remains the same), table 2.1 is necessary, because in chapters 4 and 5 basis sets as used in actual calculations are be given for results' reproduceability.

Table 2.1: How to interpret a basis set presented in CRYSTAL format

Basis set for hydrogen [44]	Interpretation
1 4	Conventional atomic number; Number of electronic shells in the set
	If conventional atomic number (NAT) is increased by 200, this part of input is reserved for the effective core potential. NAT = 99 signifies the end of basis set input. For each shell (in this case, 4):
0 0 5 1.0 1.0	5 codes and values that define each shell: • type of basis set • code for shell type (0) • number of GTFs in the shell (5, n in eq. 2.3) • formal electron charge attributed to the shell (1.0) • scale factor a (1.0, eq. 2.1)
120.0 0.000267 40.0 0.002249 12.8 0.006389 4.0 0.032906 1.2 0.095512	Exponents (α) and contraction coefficients (d) of each normalized primitive GTF.
0 0 1 0.0 1.0 0.5 1.0 0 0 1 0.0 1.0 0.13 1.0 0 2 1 0.0 1.0 0.3 1.0	Three empty (charge = 0.0) shells with 1 GTF per shell

Each shell, depending on its type, and regardless of n, is used to generate a fixed number of AOs: s shells (type 0) generate 1 AO, sp (type 1) – 4 AOs, p (type 2) – 3, d (type 3) – 5, and f (type 4) – 7. The formal shell electronic charge is the number of electrons attributed to each shell as initial electronic configuration. The electronic configuration of the atoms is used in the calculation of the atomic wave function only (and only when the guess for SCF is a superposition of atomic densities). The formal charge may correspond to a neutral atom or to an ion.

2.5.2 Boltzmann transport equation in CRYSTAL

With CRYSTAL it is possible to post-process DFT wavefunctions for evaluating the electron transport properties by solving the Boltzmann equation in the relaxation time approximation. Classically, it has the following form [2]:

$$\frac{\partial f}{\partial t} + \alpha \cdot \mathrm{grad}_v f + v \cdot \mathrm{grad}_r f = -\frac{f - f_0}{\tau}, \tag{2.4}$$

where r are Cartesian coordinates, v is velocity, α is acceleration dv/dt, $f(r,v)$ is a distribution function, such that

$$f(r,v)drdv = \text{number of particles in } drdv,$$

$\tau(r,v)$ is relaxation time, defined by the equation

$$\left(\frac{\partial f}{\partial t}\right)_{coll} = -(f - f_0)/\tau, \tag{2.5}$$

where f_0 is the distribution function in thermal equilibrium.

Solution of the classical Boltzmann transport equation provides the classical distribution function that describes positions and velocities of classical particles. In CRYSTAL, the semiclassical Boltzmann transport theory is used. Solution of the semiclassical transport equation yields a distribution function that describes electrons in an energy band. From the distribution function macroscopic quantities of interest, such as Seebeck coefficient and electronic conductivity, are derived [45].

At the core of the equations coded into CRYSTAL for obtaining transport coefficients is the transport distribution function, cast as the energy projected tensor:

$$\Xi_{qr}(E) = \tau \sum_{\mathbf{k}} \frac{1}{N_k} \frac{1}{V} \sum_{i,j} v_{i,q}(\mathbf{k}) \delta(E - E_i(\mathbf{k})), \tag{2.6}$$

where $N_{\mathbf{k}}$ is the number of $\boldsymbol{k}$-points used in sampling the reciprocal space, $v_{i,q}(\mathbf{k})$ is the velocity of the i^{th} (j^{th}) band, calculated along the direction $q(r)$, and defined as the derivative of the band energies $E(i,\mathbf{k})$ w.r.t. a reciprocal space vector k_q:

$$v_{i,q}(\mathbf{k}) = \frac{\partial E_i(\mathbf{k})}{\partial k_q}. \tag{2.7}$$

In equation 2.6, δ is an approximation to Dirac's delta function, and τ is the electronic relaxation time, which is assumed to be not dependent on k (constant relaxation time approximation). Relaxation time is temperature-dependent and cannot be obtained from first-principles calculations, and, therefore, must be either fitted or obtained experimentally [11, 46].

By integrating conductivity distributions written with tensors of equation 2.6, it is possible for CRYSTAL to obtain conductivity tensors, for instance, the electrical conductivity σ:

$$\sigma_{qr}(T;\mu) = e^2 \int dE \left(-\frac{\partial f_0}{\partial E}\right) \Xi_{qr}(E), \tag{2.8}$$

where μ is the chemical potential or Fermi level, E is the energy, f_0 is the Fermi-Dirac distribution, and T is the temperature. Thermoelectric coefficient σS, where S is the Seebeck coefficient, is cast as:

$$[\sigma S]_{qr}(T;\mu) = \frac{e}{T} \int dE \left(\frac{\partial f_0}{\partial E}\right) (E - \mu) \Xi_{qr}(E). \tag{2.9}$$

From equations 2.9 and 2.8, the Seebeck coefficient is then calculated for each value of μ. Computationally, precision of these calculations is determined, mainly, by the pre-computed wavefunctions. Accuracy depends on the density of k-points: too few points results in sparse evaluation

of $v_{i,q}(\mathbf{k})$, which yields a coarse transport distribution function. Ranges and exact values of chemical potential (μ) and temperature (T), being essentially free parameters, do not affect the quality of the calculations. Relaxation time (τ), being a scalar pre-factor, only affects values of transport coefficients, and does not have a meaningful impact on the physical description of the system.

3.EXPERIMENTAL PROPERTIES OF THE MATERIALS

3.1 Cerium dioxide

Cerium dioxide (CeO_2, ceria) is a material whose utility stems from its ionic and polaronic conductivities. Thus, it is not surprising that the polaron properties of ceria were the subject of numerous experimental and theoretical studies [47–51]. The applications based on these properties of CeO_2 include the use of it as an electrolyte in solid oxide fuel cells [52], membranes for oxygen separation [53, 54], oxygen sensors [54, 55], it has a high electrostriction coefficient, making it useful in micro-electro-mechanics [56] and other electromechanical applications [57], and it is a well-known catalyst [58]. Ceria-based membranes offer competitive oxygen permeation fluxes at temperatures below 1123 K as compared with perovskite-based membranes [59, 60]. This work focuses on interaction between oxygen vacancies and the lattice of CeO_2, including other point defects that may be present in the material.

Usually, CeO_2 exists in a fluorite structure (space group No. 225, $Fm\bar{3}m$, face-centred cubic lattice) with Ce^{+4} occupying a high-symmetry position, neighboured by eight O^{2-} ions. Pure ceria has a characteristically low small polaron conductivity [61]. In this material, polarons are created when electrons re-localize to distinct Ce^{+3} ions, affected by formation of oxygen vacancies.

Conductivity of ceria is improved when CeO_2 is doped with lanthanide ions. For example, Gd- or Tb-doped CeO_2 demonstrates higher electrical conductivity relative to undoped samples [62, 63]. Trivalent rare earth dopants, e.g. Gd^{+3}, Sm^{+3}, and Pr^{+3} promote oxygen vacancy formation and, thus, enable ionic conductivity [64–68]. Trivalent ions, specifically, Gd^{+3} have limited solubility in ceria [69] and introduce a lot of strain to the structure.

Unlike Gd and Sm, Pr and Tb ions in CeO_2 matrix can be in either $+3$ or $+4$ oxidation state, which enhances electronic conductivity of these materials. Ceria doped with Tb is a prospective material for mixed-conductive membranes for oxygen separation [53, 70]. It is attractive due to a combination of fast transport of oxygen ions, favourable redox catalytic properties and pronounced chemical compatibility with water and carbon dioxide at high temperatures. Since Tb is much more compatible with the lattice of CeO_2 than trivalent ions, it has a much better solubility (section 4.3.5), and its ability to change oxidation state affects energetics of oxygen vacancy formation (section 4.3.6).

3.2 Zinc oxide

Zinc oxide (ZnO) is a multi-functional material. Despite more than two decades of intensive research, the capabilities of ZnO are still not exhausted, and new insights for materials science can still be learned by studying this compound and its defects. The form of ZnO is no less versatile than its function: it can be grown as large single crystals of high purity, deposited as thin films, or made amorphous [71–73]. It has a 3.4 eV wide band gap, strong room temperature luminescence, high electron mobility, high thermal conductivity and large exciton binding energy [74].

This material has found uses in a large variety of applications, including but not limited to: thin film transistors, solar cells, diodes, displays [75–78], transparent conductors, sensors/emitters of blue and UV light, and to functional coatings [74, 79]; ZnO also has pigmental, (photo) catalytic, piezoelectric, antibacterial, and varistor properties [80–82] that are being explored for their application across many fields of industry.

A shared fundamental aspect for these application is the fact that creating an n-type semiconductor from ZnO is a relatively straightforward task because, among its intrinsic defects, oxygen vacancies are the most stable [83–86]. This, combined with its large band gap, electron mobility, and dopant-induced n-type conductivity [87–89] make it a very good material for transparent electronics.

Still novel applications emerge in various domains but they often require the preliminary stabilization of a p-type ZnO counterpart to the natural n-type ZnO to be stimulated. Obtaining p-type ZnO thin films would be an important milestone in transparent electronics, allowing the production of wide band gap p–n homo-junctions [90–92], opening doors to revolutionary technologies in light emitting diodes, lasers, etc. [79, 93, 94]. Unfortunately the lack of p-type ZnO slows down the launch of this promising new market activity.

Because of its considerable technological interest, a lot of research was made on the formation of local and extended defects in ZnO that might be able to produce p-type conductivity [80, 95]. In summary, all experiments and first-principle calculations carried out on ZnO bulk agree that large amount of Zn vacancies, an intrinsic p-type defect, are difficult to stabilize [96–98], even though such defects and their complexes are expected to play a pivotal role in the generation of p-type charge carriers [95].

At the same time, p-type doping in ZnO thin films is hindered by a self-compensation effect from native donor defects (V_O and Zn_i) and/or hydrogen incorporation and mostly requires elevated growth temperatures [99]. The conductivity of p-type ZnO thin films is substantially lower compared to n-type ZnO. The cause of lower conductivity is the large effective mass and thus the low mobility of the holes in the valence band, which is mainly composed of p-orbital levels of oxygen. A new approach to obtain p-type ZnO instead of doping is to produce a significant number of Zn vacancies and their complexes in order to generate p-type charge carriers [100, 101].

Among other difficulties related to achieving p-type conductivity through doping, is a strange behaviour of oxygen-substituting nitrogen. Extensive theoretical investigations clearly stipulate that nitrogen, that is considered so far as the most natural substituent for oxygen to trigger the appearance of "p-typeness" in ZnO, cannot lead to p-type conductivity at ambient conditions because of too deep acceptor levels [74, 102–104]. These assertions clearly point out the recurring problem in engendering p-type ZnO in a reproducible way. In that context, a recent discovery of nitrogen-doped zinc-deficient ZnO nanoparticles that clearly exhibit p-type properties for periods longer than 2 years and half on samples stored at ambient conditions is very surprising [105].

As a result of advances in growing methods, current research on p-type conductivity in ZnO-related topics is shifting towards complex materials such as In-Ga-Zn-O thin films [106–110], In-Zn-Sn-O [111], mixes of oxides or spinels [95, 112–114], and to amorphous phases of ZnO and related materials [89, 92, 115–118].

4.THE CASE OF CERIUM DIOXIDE

4.1 Introduction

Polaronic conductivity of cerium dioxide (CeO_2, ceria) has been a subject of numerous thorough investigations, for this property of ceria is at the root of its industrially important applications as an electrolyte in solid oxide fuel cells. Specifically, reduced ceria, CeO_{2-x}, is "one of the clearest examples of hopping conduction and the small polaron mechanism". [119]

Polarons are often defined as "the confinement of an electron within a specific region in the lattice accompanied by local lattice deformation around it". [120] Polarons form when the energy gained by trapping charge carriers exceeds the energy required to displace the surrounding atoms from their equilibrium sites. The resulting local lattice deformation is quantified by a characteristic radius: a small distortion with respect to the unit cell parameters is defined as a small polaron, while a large polaron is associated with local deformation extending beyond one unit cell. [120]

In this work the investigated system is reduced ceria, i.e. cerium dioxide with oxygen vacancies. To model this system, a supercell of CeO_2 is created, from which one oxygen atom is then extracted, together with its 8 electrons. Ce ions adjacent to the vacancy become reduced (they no longer have to share some of their electrons with the extracted oxygen, so they gain them back). This work explores how relaxation of such system with DFT methods depends on the choice of supercell (local symmetry of the defect), and which mode of electronic (de)localization is more probable in such system.

This chapter consists of two major parts: modelling oxygen vacancies in undoped CeO_2, and modelling polarons in Tb-doped CeO_2.

4.2 Oxygen vacancy in undoped CeO_2

Small polaron conductivity is typical for undoped CeO_2 [61]. Ceria intrinsically forms oxygen vacancies that are modelled here as positively charged w.r.t. undisturbed system (a region of space where an oxygen atom used to be, when vacant, has a lower electronic density), and, to compensate this charge, Ce^{3+} ions are formed. Reducing a Ce^{4+} ion to Ce^{3+} partially fills cerium's f orbital.

Localized d- or f-orbitals are typical examples for strongly correlated electronic states [19]. By extension, materials with partially filled d or f electron shells, such as transition and rare-earth metals Co, Fe, Ni, Ce, La etc., and their oxides are known as "strongly correlated materials" [121, 122]. It is common for computational studies to treat strong electronic correlation effects, necessary for describing such defects in these materials, using DFT+U approach (section 2.3.2). Particularly, in case of reduced CeO_2, it is necessary to use DFT+U method, for the use of pure LDA or GGA functionals results in metallic behaviour of the system (a typical problem in strongly correlated systems) [51, 123].

The accuracy of DFT+U calculations is critically affected by choice of the +U parameter [48, 123], which might require fitting or some self-consistent tuning [21]. Another option, presented

here, is the use of hybrid exchange-correlation DFT functionals (section 2.3.3), coupled with the site-symmetry approach, which, for any given supercell, enables identification of all possible electronic localizations for a complete comparison.

4.2.1 Supercell selection

An unsophisticated way of modelling a point defect is to place it in a high-symmetry position, and, if that does not produce a desired effect (for instance, due to symmetry, electrons might be delocalized over defect's nearest neighbours), to introduce, then, a random distortion or suppress the use of symmetry operations altogether. Either is arbitrary and as such, difficult to justify, and deliberate inclusion of randomness to the model introduces additional uncertainty to the final results of such calculations. Sometimes, however, a simple change of supercell may introduce low-symmetry sites (section 2.2) without any additional artificial restrictions.

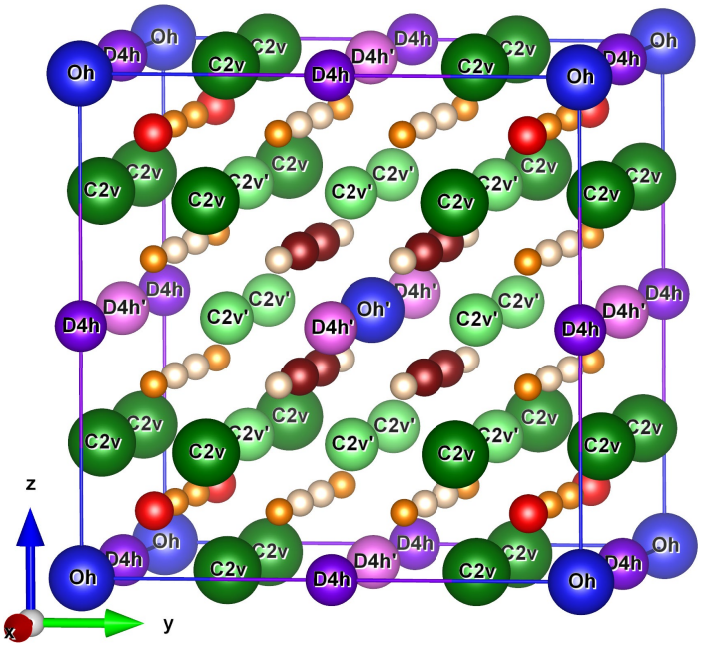

Figure 4.1: Distribution of symmetry orbits in a 96-atom CeO_2 supercell. Cationic sites are labelled. Colours and labels represent orbits of the same symmetry, see text and tables 4.1 – 4.2

Because introduction of a point defect nullifies the "inner" translations of the supercell (combinations of the host crystal primitive translations), the point group of the defective crystal is defined by the site symmetry group of the defect. Figure 4.1 illustrates this point with a 96-atom supercell of CeO_2, created with equation 2.2, where $n = 2$. If all atoms belonging to the same symmetry orbit (same colour) are substituted with a different atomic species, the entire symmetry of the supercell remains intact, including "inner" translations that exist only within this symmetry orbit and do not coincide with lattice translations. However, if the substitution is partial, changing only some atoms in the orbit, then the "inner" translations are violated and the number of symmetry operations is reduced. In effect, all possible symmetry-compatible solutions to electron localization depend on the choice of the defect placement. In addition, such symmetry analysis allows for a much more fair comparison of defects' formation energies, as no random distortions are involved.

CeO_2 crystal has fluorite structure (space group No. 225, $Fm\bar{3}m$, face-centred cubic lattice), and therefore only two transformations of its basis vectors keep the full symmetry of its space group [8]: $\left(\begin{smallmatrix} n & 0 & 0 \\ 0 & n & 0 \\ 0 & 0 & n \end{smallmatrix}\right)$, which is an isotropic expansion (eq. 2.1), and the second is transformation from face-centred cubic cell to primitive cubic cell ($F \rightarrow P$) coupled with isotropic expansion, $\left(\begin{smallmatrix} -n & n & n \\ n & -n & n \\ n & n & -n \end{smallmatrix}\right)$ (eq. 2.2). In the following sections, a symbol $\mathbf{L}\boldsymbol{V}\mathbf{(}\boldsymbol{A}\mathbf{)}$ will be used to identify supercells. L marks the type of Lattice (F for face-centred cubic, P for primitive), V is Volume expansion factor (determinant of the transformation matrix, the number of unit cells in a supercell), and A is Atom count. For instance, F64(192) means "a face-centred cubic supercell consisting of 64 unit cells, totalling 192 atoms". It also means that equation 2.1 with $n = 4$ was used to create this supercell. P32(96) means a supercell created with equation 2.2, where $n = 2$.

Using the program WYCKSPLIT [124] of the Bilbao Crystallographic Server[1] [125], it is possible to identify all symmetry-allowed splittings of Wyckoff positions. Tables 4.1 and 4.2 list distribution of oxygen and cerium atoms over the symmetry orbits for reasonably small supercells (under 200 atoms).

Table 4.1: Oxygen site symmetry in different supercells

F1(3)	F8(24)	F27(81)	F64(192)	P1(12)	P32(96)
T_d (S24)[i]	$2 \times C_{3v}$ (S6)	C_s (S2); C_{2v} (S4); $2 \times C_{3v}$ (S6); T_d (S24)	$4 \times C_s$ (S2); $4 \times C_{3v}$ (S6)	C_{3v} (S6)	$2 \times C_s$ (S2); $2 \times C_{3v}$ (S6)

i. SN is the number of point symmetry operations in a given orbit in the supercell

Table 4.2: Cerium site symmetry in different supercells

F1(3)	F8(24)	F27(81)	F64(192)	P1(12)	P32(96)
O_h (S48)	D_{2h} (S8); $2 \times O_h$ (S48)	C_{2v} (S4); C_{3v} (S6); C_{4v} (S8); O_h (S48)	C_s (S2); $2 \times C_{2v}$ (S4); D_{2h} (S8); C_{4v} (S8); T_d (S24); $2 \times O_h$ (S48)	D_{4h} (S16); O_h (S48)	$2 \times C_{2v}$ (S4); $2 \times D_{4h}$ (S16); $2 \times O_h$ (S48)

Based on this initial symmetry assessment for the purpose of modelling oxygen vacancy, not only is F27(81) the smallest supercell with a low-symmetry C_s position, it is also the most inclusive supercell, representing all possible point symmetries an oxygen position can have. Therefore, this supercell has been used in all the following calculations. As an additional note, C_s is the lowest-symmetry point group of the $Fm\bar{3}m$ space group, which further solidifies the choice of F27(81).

4.2.2 Computational details

All calculations were made using CRYSTAL [11]. Tolerance factors of 8, 8, 8, 8, and 20 for the Coulomb and exchange integrals were used. The SCF convergence threshold for the total electron energy was set to 10^{-9} Hartree, and the threshold for change in energy between consecutive geometry optimization steps was set to 10^{-8} Hartree.

[1] https://www.cryst.ehu.es

Two hybrid exchange-correlation functionals were used: PBE0 [24] and HSE06 [17, 29]. All calculations of defective cells were spin-polarized. The reciprocal space was sampled with Monkhorst-Pack [126] k-point grids of varying densities: $2 \times 2 \times 2$ for all calculations of the F27(81) supercell; $3 \times 3 \times 3$ for calculations of the primitive cell, and $32 \times 32 \times 32$ for calculating elastic constants with the primitive cell. For calculating vibrational frequencies the frozen phonon method (direct method) [127, 128] was used. Frequencies were evaluated at the **Γ**-point.

The high-frequency dielectric constant was estimated using the coupled perturbed HF/Kohn–Sham method as implemented in the CRYSTAL code [129–131]. In CRYSTAL, the total energy E of a crystal in a constant static electric field ε is expressed as

$$E(\varepsilon) = E(0) - \sum_t \mu_t \varepsilon_t - \frac{1}{2!}\sum_{tu} \alpha_{tu}\varepsilon_t\varepsilon_u - \frac{1}{3!}\sum_{tuv} \beta_{tuv}\varepsilon_t\varepsilon_u\varepsilon_v - \frac{1}{4!}\sum_{tuvw} \gamma_{tuvw}\varepsilon_t\varepsilon_u\varepsilon_v\varepsilon_w + \dots \quad (4.1)$$

with $E(0)$ the field-free energy, and $\mu, \alpha, \beta, \gamma \dots$ the total energy derivative tensors of order 1, 2, 3, 4... w.r.t. the electric field (Cartesian components indicated by subscripts *t, u, v, w*). These tensors represent, respectively, the dipole moment (μ), polarizability (α), first hyperpolarizability (β), and second hyperpolarizability (γ). In this work, only second-order effects were included (series 4.1 were truncated at the second order, and only the second energy derivatives were calculated). In this case, the accuracy of coupled perturbed HF/Kohn–Sham method is controlled by threshold on α variation ($|\Delta\alpha| <$ threshold) between two self-consistent coupled-perturbed iterations, which is set to 10^{-3} Hartree by default. In this work, it was set to 10^{-4} Hartree.

Basis sets were adopted from literature. Oxygen atoms were represented with an all-electron 8-4111G basis set taken from Bredow *et al.* [132], and for Ce atoms a basis with quasi-relativistic effective-core pseudopotential with 28 core and 30 valence electrons was adopted from [133]. Prior to the main calculations both basis sets were partially modified using the program OPTBAS [134] and HSE06 functional. Modified basis sets are given in table 4.3.

Oxygen vacancies were introduced in supercells by removing oxygen atoms from various lattice positions. Oxygen-rich conditions were assumed, as these are the operational conditions that CeO_2 is subject to as electrolyte in solid oxide fuel cells and in oxygen-separating membranes, and it is under these conditions that bulk diffusion of oxide ions is rate limiting. Therefore, formation energy of a V_O^{+2} in a neutral supercell was calculated as

$$E_F = E_{tot}^{V_O^{+2}} - E_{tot}^{p} + \mu_O, \quad (4.2)$$

where superscripts p and V_O^{+2} respectively denote a perfect supercell, and a supercell with one oxygen vacancy; E_{tot}^{X} is the total electron energy, and μ_O is the chemical potential of an oxygen atom, calculated as half of the total electron energy of a O_2 molecule.

4.2.3 Validating the model and defining baselines

Table 4.4 compares basic bulk properties of CeO_2 obtained with different computational methods to corresponding experimental values. LDA functionals systematically underestimate lattice constant, while GGA functionals, even with +U correction, tend to overestimate it. Meanwhile, hybrid functionals, while slightly underestimating the lattice constant, consistently yield values that are close to

Table 4.3: Final optimized basis sets for Ce and O. *Emphasized coefficients* have been optimized with the OPTBAS program

Ce	O
258 9	8 5
INPUT	0 0 8 2.0 1.0
30. 0 1 1 1 1 1	8020.0 0.00108
20.137829 580.083457	1338.0 0.00804
15.998482 310.302833	255.4 0.05324
14.974187 167.813944	69.22 0.1681
23.402455 -49.390229	23.90 0.3581
16.570553 -21.331879	9.264 0.3855
0 1 4 8. 1.	3.851 0.1468
101.7 0.00726 0.002188	1.212 0.0728
44.8 -0.09923 -0.008290	0 1 4 6.0 1.0
24.5 0.50636 0.08332	49.43 -0.00883 0.00958
12.306 -1.01163 -0.39978	10.47 -0.0915 0.0696
0 1 3 8. 1.0	3.235 -0.0402 0.2065
6.7756 -0.1859 0.2271	1.217 0.379 0.347
3.2632 1.0045 0.6945	0 1 1 0.0 1.0
1.564 0.4841 0.3529	*0.43361514863819* 1.0 1.0
0 1 2 4. 1.	0 1 1 0.0 1.0
0.75964890198940 0.633 0.6035	*0.14503375742163* 1.0 1.0
0.34489331807625 0.9051 0.6571	0 3 1 0.0 1.0
0 1 1 0. 1.	*0.40124357802175* 1.0
0.12946372835605 1. 1.	
0 3 6 10.0 1.0	
40.79 0.0083	
15.24 -0.0583	
6.827 0.219	
3.78 0.4152	
2.041 0.3666	
1.034 0.1445	
0 3 1 0.0 1.0	
0.495974993386773 1.	
0 4 4 0. 1.0	
83.88 0.005	
30.04 0.0442	
12.92 0.1352	
5.851 0.2670	
0 4 3 0. 1.0	
2.635 0.3490	
1.17 0.3327	
0.54100633274158 0.221	
0 4 1 0. 1.	
0.35173856451657 1.	

those experimentally observed ones. Bulk moduli and elastic constants are generally well-reproduced by all methods, except those that severely overestimate the lattice constant.

In CeO_2 the valence band top is mainly of O $2p$ character, and the band gap between the O $2p$ band and unoccupied Ce $5d$ states (O$2p$–Ce$5d$) is estimated as 8.2 eV in our PBE0 calculations. In table 4.4 we also give the energy distance between the O $2p$ band and an unoccupied (polaronic) Ce $4f$ band (O $2p$–Ce $4f$) lying between these two band gaps [48].

Table 4.4: Basic bulk and mechanical properties of defect-free CeO_2

Property	Exp.	PBE0 (HSE06), this work	GGA+U	LDA(GGA)
Conventional cell parameter (Å)	5.406[135] 5.411[136]	5.393 (5.396)	5.494[47] 5.429[137] 5.426[138] [i]	5.330[139], 5.366[140] (5.430[139])
Band gap (O $2p$–Ce $4f$) (eV)	$\sim$ 3[141]	4.32 (3.64)	2.35[47] 2.50[138]	—
Band gap (O $2p$–Ce $5d$) (eV)	$\sim$ 6[141]	8.24 (7.57)	5.31[47] 5.50[138]	—
Bulk modulus (GPa)	204[142] [ii] –220[136]	219[ii] (218)[ii]	181[47] 216[138]	219[139][ii], 211[140][ii] (184[139])[ii]
C_{11} (GPa)	403[142]	426 (423)	391[138]	400[139], 386[140] (354[139])
C_{12} (GPa)	105[142]	116 (116)	129[138]	128[139], 124[140] (99[139])
C_{44} (GPa)	60[142]	65 (65)	57[138]	64[139], 73[140] (51[139])
Cohesive energy (eV)	-21[143]	-19 (-19)	—	—

i. Ref. [138] includes spin orbit effects
ii. Bulk modulus calculated as $(C_{11} + 2C_{12})/3$

In Table 4.5 calculated phonon frequencies and dielectric constants are compared to experimental values and to prior results. Frequencies of T_{1u} and T_{2g} vibrational modes calculated with hybrid DFT functionals are very consistent with those obtained experimentally. Thus, hybrid functionals have proved themselves to be useful for proper calculations of the phonon frequencies.

In conclusion, hybrid DFT functionals with the selected basis sets generally outperform LDA and GGA(+U) functionals, yielding results that are, on average, more consistent with experimentally observed properties of CeO_2. Both functionals reproduce basic properties of bulk ceria reasonably well, and, while HSE06 better reproduces the band gap of this material in comparison to PBE0, the latter is computationally less demanding, and produces more accurate vibrational frequencies. For these reasons the subsequent calculations for F27(81) supercells with oxygen vacancy were performed exclusively with PBE0 functional.

Table 4.5: Phonon properties[i] of defect-free CeO_2

Property	Exp.	PBE0 (HSE06) this work	HSE [144]	LDA [140]
Static dielectric constant ϵ^0	~23.0 [145][ii] 25.0 [146]	22.7	—	23.0
High frequency dielectric constant ϵ^∞	5.31 [146]	5.28	5.70	6.23
T.O. T_{1u} vibration (cm^{-1})	272[146] 283 [145]	295 (293)	264	301
T_{2g} vibration (cm^{-1})	465 [146]	470 (293)	451	—
L.O. vibration (cm^{-1})	590 [146]	612	573	579

i. Vibrations are evaluated at the **Γ**-point.
ii. ϵ^0 taken at room temperature

4.2.4 Oxygen vacancies and electronic localization

Normally, cerium dioxide is ionic enough to safely assume that all Ce ions, having donated all their outer shell electrons ($4f^1 5d^1 6s^2$), are in the 4+ oxidation state, and all oxygen ions are 2–. Therefore, creation of an oxygen vacancy by removing an oxygen atom from the supercell together with its own valence electrons, leaves behind the two donated electrons that tend to localize in the conduction sub-band formed by Ce's $4f$ orbitals. One way of modelling experimentally observed formation of small polarons [61] is to consider the four Ce ions which are nearest neighbours to an oxygen vacancy, and to compare different modes of electronic localization over these ions. In the text below, electrons' localization over two neighbouring Ce ions will be considered as representation of a small polaron, and localization over three and more Ce ions—a large polaron, for such localization, together with atomic displacements w.r.t. their original positions, exceeds the boundaries of CeO_2 primitive cell, even though it is still confined to the supercell.

Table 4.6 presents all possible[2] configurations of these localizations. The first column names the site symmetry of the removed oxygen ion, and categorizes symmetry equivalence of the neighbouring Ce ions. For instance, the label $C_s(S2)$/(Ce1,Ce2)(Ce3)(Ce4) means that an oxygen vacancy at a C_s site that has two symmetry operations, is surrounded by three distinct groups of Ce ions, one of which has two symmetrically equivalent ce ions (Ce1 and Ce2). Label $C_{3v}(S6)$/(Ce1)(Ce2,Ce3,Ce4) marks an oxygen vacancy at a C_{3v} site with 6 symmetry operations, surrounded by two groups of Ce ions, one of which has three symmetrically equivalent Ce's. For each allowed magnetic configuration, all symmetrically equivalent Ce ions must have the same spin projection, either $1/2$, $-1/2$, or 0.

Columns 2-4 of table 4.6 describe the magnetic properties of each solution. Second column lists the total projected spin (S_z) for each starting magnetic configuration, as well as the distribution of electrons: '+' marks a Ce ion with a non-zero net magnetic moment (*some* degree of electronic localization), and '–' marks a Ce ion without an associated magnetic moment. In the 3rd column, N is the number of displaced Ce ions with a non-zero magnetic moment. The next column lists values of the magnetic moments (μ) of these ions after relaxation (signs denote spin orientation).

[2]Computationally viable, see text below

Columns 5-6 list bond lengths between displaced Ce ions and their closest O [d(Ce–O)], and relative displacements of all V_O^{+2}-encircling Ce ions with respect to their distances in a perfect crystal (positive sign of Δd(Ce–Ce) means an outward motion). For $N = 2$ (S2 and S4) there are 3 values: the change in distance between the Ce ions closest to the V_O^{+2}, the change of distance between the other two Ce ions, and the change of distance between these two pairs of ions. For $N = 3$ (S2) these three values are: distance change in the closest pair, distance change for the next closest ion, and distance change between Ce with non-zero μ, same as for $N = 4$ (S4), except all values refer to pairs of ions. For $S6$ two values are given: changes of distances between the three equivalent ions, and the distance change between the other ion and the three equivalent ones. For S24 there is only one value, the distance change between the 4 equivalent ions.

Formation energies according to equation 4.2 are in the 7^{th} column, and are given with respect to solution with the lowest energy (first row of the table, $C_s(S2)$ with $S_z = 0$, and $E_F = 4.10$ eV). The last column lists volumes of the relaxed supercells.

Table 4.6 clearly demonstrates that exploiting symmetry is necessary for exploring all possible magnetic configurations. At the time of publishing [147], this has been a novel approach to modelling point defects in symmetric supercells. Another symmetry-related conclusion is that symmetry reduction is necessary to obtain a solution with the lowest energy: the highest vacancy formation energies correspond to the most symmetrical solutions, where the two leftover electrons are delocalized over the four neighbouring Ce cations, forming a large polaron.

In contrast, for symmetry configurations with 2 Ce ions neither of which is symmetrically equivalent to either of two remaining cations, it is possible to obtain a small polaron, with vacancy electrons localizing on 2 Ce cations. Three such solutions that are listed in table 4.6 as $C_s(S2)$ with $S_z = 0$, $C_s(S2)$ with $S_z = 1$, and $C_{2v}(S4)$ with $S_z = 1$, have low vacancy formation energies, with the first one, corresponding to opposite-spin solution, being the lowest. Crucially, the opposite-spin solution is only available for the $C_s(S2)$ configuration, in which the 4 Ce atoms are split into 3 symmetry orbits. Small energy differences between spin-aligned and opposite-spin solutions are consistent with previous results [50].

Notably, table 4.6 is missing two entries: $C_s(S2)$ with $S_z = 2$, and $C_{3v}(S6)$ with $S_z = 1/2$. These solutions are unstable and correspond to large polarons, i.e. are energetically unfavourable.

Structural changes are consistent across the entirety of results: Ce ions move away from the vacancy and closer to the other O ions, while volume of the supercell increases, with largest expansion corresponding to small polaron-like solutions. This result corresponds well to experimental data: Marrocchelli *et al.* [148, 149] has attributed volume increase in CeO_2 to chemical expansion caused by larger cation size of reduced Ce ions.

Results presented in this section are published in ***[A1]***. The author has performed basis optimisation calculations for Ce and O, calculations of CeO_2 (both with- and without oxygen vacancy), has gathered the data and has contributed his writing to the paper.

Table 4.6: All magnetic configurations allowed by point symmetries in the F27(81) supercell

Site symmetry/ symmetry equivalence of Ce atoms	Spin projection (S_z)	N	μ, μ_B	d(Ce–O)[i], Å	Δd(Ce–Ce)[ii], Å	ΔE_F[iii], meV	Volume[iv], Å^3
$C_s(S2)$/ (Ce1,Ce2)(Ce3)(Ce4)	0 (–,–)(+)(+)	2	0.96 -0.96	2×2.30	0.17 0.23 0.30	0	1068.07
	1/2 (+,+)(–)(+)	3	2×-0.49 0.96	2×2.24 2.30	0.20 0.22 0.20	306	1067.47
	1 (–,–)(+)(+)	2	2×0.96	2×2.30	0.17 0.23 0.30	0.2	1068.06
	3/2 (+,+)(–)(+)	3	2×0.50 0.96	2.25 2.25 2.31	0.21 0.23 0.21	338	1067.27
$C_{2v}(S4)$/ (Ce1,Ce2)(Ce3,Ce4)	0 (+,+)(+,+)	4	$2 \times +0.49$ 2×-0.49	2×2.25	0.22 0.22 0.23	610	1066.56
	1 (–,–)(+,+)	2	2×0.96	2×2.30	0.17 0.23 0.30	0.2	1068.08
	2 (+,+)(+,+)	4	4×0.49	4×2.25	0.22 0.22 0.23	611	1066.50
$C_{3v}(S6)$/ (Ce1)(Ce2,Ce3,Ce4)	1 (+)(+,+,+)	4	-0.95 3×0.35	2.30 3×2.23	0.21 0.24	432	1066.67
	3/2 (–)(+,+,+)	3	3×0.65	3×2.27	0.22 0.26	396	1067.82
	2 (+)(+,+,+)	4	0.97 3×0.35	2.30 3×2.23	0.21 0.24	431	1066.82
$T_d(S24)$/ (Ce1,Ce2,Ce3,Ce4)	2 (+,+,+,+)	4	4×0.49	4×2.24	0.25	768	1066.71

i. 2.34 Å in the perfect crystal
ii. 3.82 Å in the perfect crystal
iii. As calculated by eq. 4.2, w.r.t. the first row of this table with $E_F = 4.10$ eV
iv. 1059.19 Å^3 for the perfect crystal

4.3 Tb in CeO_2

Lanthanide doping generally improves performance of ceria-based materials (section 3.1). Ionic conductivity in $Ce_{1-c}Tb_cO_{2-\delta}$ increases with Tb content, and this system's electronic conductivity (p-type) reaches noticeably high values at 50% Tb. However, utility of some lanthanides is limited by their solubility. For instance, calculated phase diagrams of $Ce_{1-c}Gd_cO_{2-c/2}$ [69, 150] show that the phase separation into Gd_2O_3 and CeO_2 occurs below certain transition temperature that weakly depends on Gd concentration.

Experiments on solid solutions with Tb content up to 60% [151] do not indicate a second phase formation. On the other hand, the electron energy loss spectroscopy and transmission electron microscopy measurements [152] demonstrated the formation of domains containing Tb^{3+} and oxygen vacancies, in the range of Tb concentration from 0 to 50% with a secondary phase formation observed in x-ray diffraction spectra for Tb concentrations higher than 80% [153]. Thus, understanding solubility data of Tb^{4+} is missing as well and may be important for the use of $Ce_{1-c}Tb_cO_2$ for oxygen separation, because, as was observed in [154], the increase in Tb content leads to an increase in the oxygen uptake.

At the time of conducting this research, no reliable, unionised, gaussian-type orbital basis set was available for Tb, therefore, a PW basis set was used in this part of the study. This section answers two questions about Tb in CeO_2: how well is Tb soluble in this system, and how does its presence affect formation energetics of V_O^{+2} and its local and electronic structure.

4.3.1 Supercell selection

Four structures were used to analyse Tb solubility in CeO_2: two unit cells for the cases of pure CeO_2 and TbO_2 in fluorite structure, representing a +4 oxidation state of either ion. The other two are superstructures (ordered solid solutions), representing two different (absolutely ordered) Tb distribution modes at 50% substitution. The first superstructure is a primitive cell, P1(12), with Tb layers ordered in the [001] direction, fig. 4.2(a). The second superstructure is a 8-fold isotropic expansion of the face-centred cubic cell, F8(24), with Tb layers ordered in the [111] direction, fig. 4.2(b).

These four structures make up a representation of $(Ce_{1-c}Tb_c)O_2$ solid solution with a varied fraction of Tb atoms in the fluorite structure, where Ce or Tb atoms occupy sites of fcc lattice immersed in a field of oxygen atoms that form the background lattice. In the analysis of fcc sublattice's phase stability, varying the Tb concentration c is equivalent to moving along the quasibinary cross-section of the ternary Ce–Tb–O phase diagram.

Thermodynamics of such solid solutions may be formulated as in Ref. [156], in terms of the effective interatomic mixing potential in A–B alloys, which in this case is $(Ce_{1-c}Tb_c)$. Tb's concentration variation affects interaction of the Ce—Tb sub-system with the oxygen background, which also changes Ce—Ce, Ce—Tb, and Tb—Tb interactions, meaning that the latter differ from these in binary Ce—Tb solid solutions. This change of interaction is automatically accounted for in the DFT+U calculations because of their self-consistent character.

This model is only applicable for absolutely ordered structures. To further investigate be-

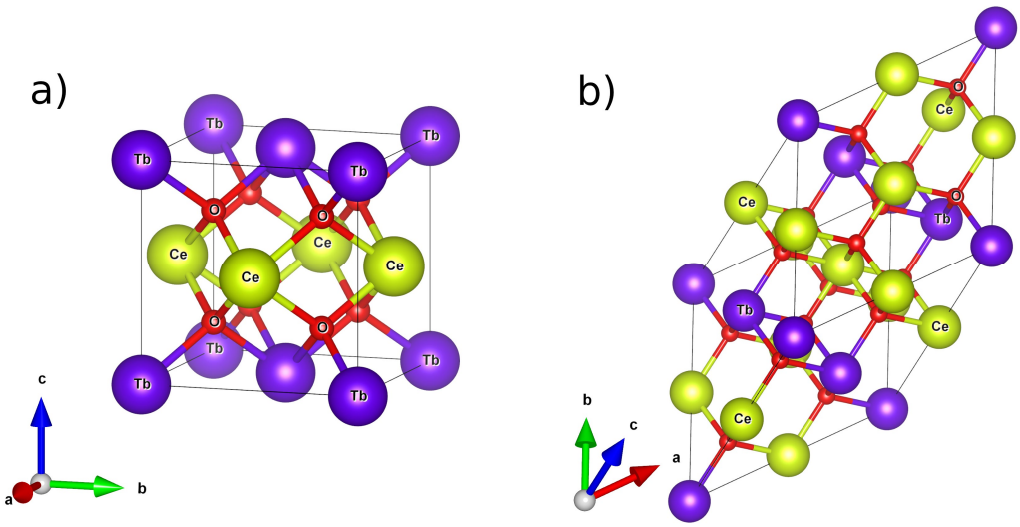

Figure 4.2: Two superstructures, representing different orderings in $Ce_{0.5}Tb_{0.5}O_2$ solutions, corresponding to (a): P1(12), and (b): F8(24) supercells, adopted from [155]

haviour of the $(Ce_{1-c}Tb_c)O_2$ system at finite temperatures from calculations of the ordered phases at T=0 K, it is necessary to re-formulate the problem in a way that allows to extract the energy parameters for further thermodynamic analysis of the relative stability of the structures beyond T=0 K. These parameters may be used for studying disordered or partly ordered solid solutions.

A detailed analysis of Tb properties in CeO_2 matrix, including Tb's effect on oxygen vacancy formation and the associated electronic localization, was performed using a 96-atom supercell P32(96). The choice of this supercell is motivated by a balance between reasonable concentration (ca. 3 at.%), relatively small size, and a good variety of sites for Tb placement, see tables 4.1 and 4.2.

4.3.2 Computational details

DFT calculations were performed using VASP 5 with PBE PAW potentials generated by Georg Kresse, following methods suggested by Peter Blöchl [39, 40]. PBE exchange-correlation functional [17] was used with an on site +U correction, as formulated by Dudarev *et al.* [20]. U values were chosen based on available data in literature: for Ce $4f$ electrons, U=5.0 was used [50, 157], while U=6.0 was applied to Tb $4f$ electrons [138]. Both values were applied simultaneously. Plane-wave cutoff energy was set to 520 eV, all calculations were spin-polarized, convergence threshold for difference in total energy was set to 10^{-6} eV. Integration in the reciprocal space was done using the following Γ-centred Monkhorst-Pack meshes of k-points: $4 \times 4 \times 4$ for primitive cells and P1(12) supercell (fig. 4.2(a)), $3 \times 3 \times 3$ for F8(24) supercell (fig. 4.2(b)), and $2 \times 2 \times 2$ for P32(96) supercell. Charges of ions were calculated using Bader's space-partitioning scheme [158, 159].

To link DFT results with the analysis of the relative stability of phases at $T \neq 0$ K, Concentration Waves method (CW), as formulated in refs. [156, 160] was used. It has several advantages over other statistical theories of alloys. One such advantage is that the distribution of B atoms in a binary A–B alloy is described by a single occupation probability function, $n(\vec{R})$. This function gives the probability to find the atom B (Tb, in this case) at the site $\vec{R}$ of the lattice. Such approxima-

tion is based on the treatment of the ordering phases in the crystalline structure of solid solution which are stable with respect to the formation of antiphase domains. The choice of these ordered structures does not depend on the type of interatomic interactions and is dictated only by symmetry considerations [161, 162].

The method of concentration waves is known to take into consideration long-range interactions in an alloy and to predict the structure of an ordered phase from a knowledge of the set of interatomic interaction energies. This method formulates the structure determination problem in terms of the reciprocal lattice through the analysis of CW amplitudes which are, on the one hand, structure amplitudes of the superlattice reflections and, on the other hand, long-range order (LRO) parameters. The occupation probability $n(\vec{R})$ for atoms at position $\vec{R}$ can be represented in a Fourier series by linear superpositions of static concentration waves:

$$n(\vec{R}) = c + \frac{1}{2}\sum_j [Q(\mathbf{k}_j)\exp(i\mathbf{k}_j\vec{R}) + Q^*(\mathbf{k}_j)\exp(-1\mathbf{k}_j\vec{R})] \tag{4.1}$$

A static CW is represented as $\exp(i\mathbf{k}_j\vec{R})$, where $\mathbf{k}_j$ is a nonzero wave vector defined in the first Brillouin zone of the disordered alloy, $\vec{R}$ is a site vector of the lattice, and the index j denotes the wave vectors in the Brillouin zone. $Q(\mathbf{k}_j)$ is amplitude of a static CW, and c is the atomic fraction of the alloying element. The star set of wave vectors $\mathbf{k}_j$ is formed by several interpenetrating Bravais lattices that can be brought in coincidence with each other by the superlattice rotation and reflection symmetry operations. Usually, the term refers only to sublattice sites that form the Bravais lattice.

The concentration waves are eigenfunctions of the matrix formed by pairwise interatomic energies $\tilde{V}_{pq}(\vec{R},\vec{R}\prime)$. In an AB binary system, $\tilde{V}(\vec{R},\vec{R}\prime)$ is the interaction energy for atoms at lattice sites $\vec{R}$ and $\vec{R}\prime$ [156, 160, 163]:

$$\tilde{V}\left(\vec{R},\vec{R}'\right) = V_{AA}\left(\vec{R},\vec{R}'\right) + V_{BB}\left(\vec{R},\vec{R}'\right) - 2V_{AB}\left(\vec{R},\vec{R}'\right). \tag{4.2}$$

4.3.3 Formation energy

Gibbs formation energy for oxygen vacancy in Tb-doped CeO_2 was calculated as

$$\Delta G_F^{V_O^{+2}} = E_{tot}^{Tb,V_O} - E_{tot}^{Tb} + \mu_O(T, p_{O_2}), \tag{4.3}$$

where $E_{tot}^{Tb,V_O}, E_{tot}^{Tb}$ are total electronic energies of supercells, with, respectively, co-presence of Tb and V_O^{+2}, and that which only has a Tb ion. Oxygen chemical potential $\mu_O(T, p_{O_2})$ was calculated according to a method published in [164], which casts it as

$$\mu_O(T, p_{O_2}) = \mu_O^0(T) + \frac{1}{2}k_BT\ln\frac{p_{O_2}}{p^0} = E_{tot}^{AO} - E_{tot}^{A} - \Delta G^{AO}(T^0) + \Delta\mu_O(T) + \frac{1}{2}k_BT\ln\frac{p_{O_2}}{p^0}, \tag{4.4}$$

where $\mu_O(T)$ is the standard chemical potential, superscripts AO and A denote, respectively, a reference oxide, and its metal; $\Delta G^{AO}(T^0)$ is the oxide's standard heat of formation, taken from a database of experimentally obtained values [165]. $\Delta\mu_O(T)$ is difference between chemical potential at a temperature T and that in the standard state ($T^0 = 298.15$ K), which is also taken from the database. k_B is the Boltzmann constant, p_{O_2} and p^0 are partial oxygen pressure and start pressure,

respectively.

Values of E_{tot}^{AO} and E_{tot}^{A} were calculated with DFT method; computational treatment of oxides included van der Waals correction by Grimme *et al.* [166], since inclusion of these corrections yielded more precise values of lattice constants (especially for lighter metal oxides), and produced a smaller root mean square deviation for the whole dataset. The final value of $\mu_O(T, p_{O_2})$ was obtained by averaging the values computed for different oxides, see table 4.7. This approach does not rely on O_2 calculations, is computationally cost-effective (in comparison to hybrid DFT in PW approximation and to calculating an isolated O_2 molecule), and enables comparison between experimental data and computational results.

Table 4.7: Reference oxides for evaluating μ_O

Crystal	Lattice constant, Å	Lattice constant (D3), Å	Lattice constant (exp), Å	Formation energy (D3), $eV \cdot mol^{-1}$	Formation energy (exp), $eV \cdot mol^{-1}$
Li_2O	4.634	4.554	4.619 [167]	-5.895	-6.205 [165]
Na_2O	5.539	5.464	5.55 [167]	-4.085	-4.332 [165]
MgO	4.233	4.200	4.211 [168]	-5.568	-6.235 [165]
Al_2O_3	4.809(a) 13.114(c)	4.787(a) 13.056(c)	4.761(a) 12.994(c)[169]	-15.432	-17.367 [165]
K_2O	6.487	6.439	6.436 [167]	-3.365	-3.764 [165]
CaO	4.839	4.801	4.811 [170]	-6.074	-6.582 [165]
Rb_2O	6.877	6.835	6.74 [171]	-3.04	-3.421 [172]
SrO	5.204	5.163	5.104	-5.617	-6.136 [165]
BaO	5.614	5.579	5.523 [171]	-5.066	-5.681 [165]
CeO_2	5.463	5.437	5.410 [173]	-10.455	-11.301 [174]
BeO	2.714(a) 4.405(c)	2.696(a) 4.381(c)	2.698(a) 4.380(c)[171]	-5.578	-6.305 [165]
SnO	3.859(a) 5.015(c)	3.841(a) 4.818(c)	3.802(a) 4.836(c)[171]	-2.696	-2.909 [165]
PbO	4.052(a) 5.387(c)	4.039(a) 5.052(c)	3.975(a) 5.023(c)[171]	-2.335	-2.274 [165]
ThO_2	5.619	5.589	5.5997 [171]	-11.694	-12.711 [165]
CdO	4.782	4.762	4.695 [171]	-2.119	-2.768 [165]
Ag_2O	4.811	4.793	4.718 [175]	-0.203	-0.322 [176]
SiO_2	5.022(a) 5.510(c)	4.946(a) 5.449(c)	4.913(a) 5.404(c) [177]	-8.466	-9.440 [165]
TiO_2 (anatase)	3.825(a) 9.660(c)	3.821(a) 9.547(c)	3.785(a) 9.514(c)[171]	-8.774	-9.729 [165]
TiO_2 (rutile)	4.660(a) 2.968(c)	4.643(a) 2.960(c)	4.594(a) 2.958(c)[171]	-8.731	-9.784 [165]

4.3.4 Validating model and defining baselines

Data in table 4.8 compares $(Ce_{1-c}Tb_c)O_2$ superstructures to fluorite structures of their parent oxides.

Table 4.8: Local environment of Tb in CeO_2 in comparison to pure structures

	CeO_2 F1(3) $(Fm\bar{3}m)$	$Ce_{0.5}Tb_{0.5}O_2$ P1(12) $(P4/mmm)$	$Ce_{0.5}Tb_{0.5}O_2$ F8(24) $(R\bar{3}m)$	TbO_2 F1(3) $(Fm\bar{3}m)$
Lattice constants, Å	5.50 5.41 [136]	5.51 5.29	7.69 18.75	5.35 5.22 [178], 5.31 [179]
Band gap, eV	O 2*p*–Ce 4*f*: 2.10 ∼ 3 [141] O 2*p*–Ce 5*d*: 5.20 ∼ 6 [141]	O 2*p*–Ce 4*f*: 1.59 O 2*p*–Tb 4*f*: 3.44 O 2*p*–Me 5*d*: 4.39	O 2*p*–Ce 4*f*: 1.41 O 2*p*–Tb 4*f*: 3.20 O 2*p*–Me 5*d*: 4.28	O 2*p*–Tb 4*f*: 2.93 O 2*p*–Tb 5*d*: 4.25
Bader charge	Ce: 2.34	Ce:2.35 Tb:2.18	Ce:2.38 Tb:2.17	Tb:2.18
Magnetic moment, μ_B	—	Tb:6.23	Tb:6.22	Tb:6.21

For the purposes of distinguishing oxidation states of Tb ion in CeO_2, two parent oxides with different oxidation states of Tb were calculated. Properties of Tb ions in these oxides form a baseline for further analysis. In TbO_2 Tb is in +4 oxidation state, however in literature the fluorite structure ($Fm\bar{3}m$ space group) is attributed to a range of compositions, from $TbO_{1.85}$ to TbO_2 [179], with lattice constants in the range between 5.213 and 5.31 Å, with Tb–O bond length of about 2.26–2.30 Å[178–180].

Tb_2O_3 crystallizes in the bixbyite structure (C-type, space group $Ia\bar{3}$), in which Tb ions occupy Wyckoff positions *b* and *d* (point groups S_6 and C_{2h} respectively), with lattice constant $a = 10.71$ Å. Tb ions at two different sites both have six adjacent oxygen ion, but each has different Tb–O bond lengths: $Tb^b_{S_6}$–O = 2.30 Å; $Tb^d_{C_{2h}}$–O = 2.28, 2.29, 2.32 Å[181–183]. Experimentally, terbium in TbO_2 has a magnetic moment of 6.25 ± 0.10 μB at 1.5 K. However, at 1.5 K, the total moment of Tb in Tb_2O_3 is 4.2 μB, appreciably lower than for the free ion. Below 3 K both structures are antiferromagnetically ordered, with Néel temperatures of 3 K and 7 K for TbO_2 and C-type Tb_2O_3, respectively [184].

Computationally, Tb ions in these two oxides have much more similar magnetic moments. Table 4.9 summarises the differences between Tb ions in TbO_2, Tb_2O_3, and embedded in P32(96) supercell of CeO_2. Calculated lattice parameters are 5.35 and 10.70 Å for TbO_2, and Tb_2O_3, respectively.

4.3.5 Tb solubility in CeO_2

The effective interatomic mixing potential is expressed in the form

$$\tilde{V}\left(\vec{R},\vec{R}'\right) = V_{CeCe}\left(\vec{R},\vec{R}'\right) + V_{TbTb}\left(\vec{R},\vec{R}'\right) - 2V_{CeTb}\left(\vec{R},\vec{R}'\right), \tag{4.5}$$

where $V_{CeCe}\left(\vec{R},\vec{R}'\right)$, $V_{TbTb}\left(\vec{R},\vec{R}'\right)$, and $V_{CeTb}\left(\vec{R},\vec{R}'\right)$ are effective pairwise interatomic potentials, and $\vec{R}$, $\vec{R}'$ are sites in the cationic sub-lattice. Configurational part of the free energy for a

Table 4.9: Calculated magnetic moments of Tb in various systems

Tb OS /System/Symmetry	$\mu(\mathrm{Tb})/\mu_\mathrm{B}$	Tb–O bond length/Å
$\mathrm{Tb}(^{+}4)/\mathrm{TbO_2}/\mathrm{O_h}$	6.21	2.32
$\mathrm{Tb}(^{+}4)/(\mathrm{Ce,Tb})\mathrm{O_2}/\mathrm{O_h}$	6.21	2.37
$\mathrm{Tb}(^{+}4)/(\mathrm{Ce,Tb})\mathrm{O_2}/\mathrm{C_{2v}}$	6.21[i]	2.37[i]
$\mathrm{Tb}(^{+}3)/(\mathrm{Ce,Tb})\mathrm{O_2}/\mathrm{C_{2v}}$	6.08[i]	2.39, 2.40
$\mathrm{Tb}(^{+}3)/\mathrm{Tb_2O_3}/\mathrm{C_{2h}}$	5.99[i]	Tb1: 2.30; Tb2: 2.27, 2.29, 2.36

i. Very close values of the property were obtained for all Tb ions in the supercell, even though Tb site symmetry is low.

solid solution (neglecting the phonon contribution) in CW approach is given in [156] as:

$$\begin{aligned} F = \frac{1}{2} \sum_{\substack{\vec{R},\vec{R}' \\ \vec{R}\neq\vec{R}'}} \tilde{V}\left(\vec{R},\vec{R}'\right) n\left(\vec{R}\right) n\left(\vec{R}'\right) \\ + kT \sum_{\vec{R}} \left[n\left(\vec{R}\right) \ln\left(n\left(\vec{R}\right)\right) + \left(1-n\left(\vec{R}\right)\right) \ln\left(1-n\left(\vec{R}\right)\right)\right] \\ - \mu \sum_{\vec{R}} n(\vec{R}). \end{aligned} \tag{4.6}$$

Summation in equation 4.6 runs over sites of the Ising lattice (fcc in this case), with Ce and Tb atoms distributed in it. The first term in equation 4.6 corresponds to the internal energy, the second one is entropy term (-TS), and μ is chemical potential (strictly, indefinite multiplier of Lagrange). The function $n\left(\vec{R}\right)$ that determines the distribution of solute atoms in the ordered superstructures that are stable with respect to the formation of antiphase domains may be expanded into the Fourier series:

$$n\left(\vec{R}\right) = c + \frac{1}{2} \sum_{s} \eta_s \sum_{j_s} \left[\gamma_s\left(j_s\right) \exp\left(i\vec{\mathbf{k}_{j_s}}\vec{R}\right) + \gamma_s^* \exp\left(-i\vec{\mathbf{k}_{j_s}}\vec{R}\right)\right], \tag{4.7}$$

where $\vec{\mathbf{k}_{j_s}}$ are vectors of the reciprocal lattice belonging to the star s, j_s numerates vectors of the star s, and $\gamma_s(j_s)$ are coefficients that determine symmetry of the function $n\left(\vec{R}\right)$ with respect to reflection and rotation operations. $n\left(\vec{R}\right)$ linearly depends on the long range order (LRO) parameters (η_s) of the superstructures that may be formed on the basis of the Ising lattice of the disordered solid solution. The LRO parameters are defined in such a way that they are equal to unity in a completely ordered state, where the occupation probabilities $n\left(\vec{R}\right)$ on all the lattice sites $\left\{\vec{R}\right\}$ are either unity or zero. To determine the LRO parameters, an additional normalization condition for $\gamma_s(j_s)$ should be used:

$$\sum_{j_s} \gamma_s(j_s) = 1 \tag{4.8}$$

For the disordered state all η_s are equal to zero. Substitution of equation 4.7 into equation 4.6 allows casting the free energy of formation of solid solution in terms of Fourier transforms of the

effective interatomic mixing potential, $\tilde{V}\left(\vec{\mathbf{k}_{j_s}}\right)$:

$$\tilde{V}\left(\vec{\mathbf{k}_{j_s}}\right) = \sum_a \tilde{V}\left(\vec{R_a}\right) \cdot \exp\left(i\vec{\mathbf{k}_{j_s}}\vec{R_a}\right). \tag{4.9}$$

The two superstructures (fig. 4.2) used here to represent $(Ce_{1-c}Tb_c)O_2$ solid solution are characterized by their $\vec{k_{j_s}}$ vectors: $\vec{k_1} = \frac{2\pi}{a}(0,0,1)$ for P1(12), and $\vec{k_1} = \frac{2\pi}{a}(\frac{1}{2},\frac{1}{2},\frac{1}{2})$ for F8(24), where a is the cubic lattice parameter. Substituting these vectors in equation 4.7 yields the following occupation probabilities for each superstructure:

$$n_1\left(\vec{R}\right) = c + \eta_1\gamma_1 \exp(2\pi i z) \tag{4.10}$$

$$n_2\left(\vec{R}\right) = c + \eta_2\gamma_2 \exp\left(i\pi(x+y+z)\right). \tag{4.11}$$

For both superstructures in this analysis $c = 0.5$, and LRO parameters are unitary, thus $\gamma_1 = \gamma_2 = 1/2$.

Substituting equations 4.10 and 4.11 into equation 4.5, free energies of formation for the superstructure 1 and 2 (per site of fcc sub-lattice), respectively, are obtained:

$$\begin{aligned} F_1 = {} & \frac{1}{2}\tilde{V}(0)c(c-1) + \frac{1}{8}\tilde{V}\left(\vec{\mathbf{k}_1}\right)\eta_1^2 \\ & + kT\left[\left(c+\frac{1}{2}\eta_1\right)\ln\left(c+\frac{1}{2}\eta_1\right) + \left(1-c-\frac{1}{2}\eta_1\right)\ln\left(1-c-\frac{1}{2}\eta_1\right)\right] \end{aligned} \tag{4.12}$$

$$\begin{aligned} F_2 = {} & \frac{1}{2}\tilde{V}(0)c(c-1) + \frac{1}{8}\tilde{V}\left(\vec{\mathbf{k}_2}\right)\eta_2^2 \\ & + kT\left[\left(c+\frac{1}{2}\eta_2\right)\ln\left(c+\frac{1}{2}\eta_2\right) + \left(1-c-\frac{1}{2}\eta_2\right)\ln\left(1-c-\frac{1}{2}\eta_2\right)\right], \end{aligned} \tag{4.13}$$

where $\tilde{V}(0)$ is is the Fourier transform of the effective interatomic mixing potential for $k = 0$. In these equations the first two terms are structures' mixing energies, and the last term is configurational entropy of mixing. These free energies F_i show energy (dis)advantage of the structures with respect to a standard state that is the mixture of their constituents, CeO_2 and TbO_2, which has the energy

$$E_{stand} = E_{CeO_2} \cdot (1-c) + E_{TbO_2} \cdot c, \tag{4.14}$$

where E_{CeO_2} and E_{TbO_2} are the total energies of these compounds, obtained from DFT+U calculations at $T = 0$ K. For absolutely ordered structures at $T = 0$ K, $c_{st} = 1/2$, and $\eta_{1,2} = 1$, mixing energies are

$$\Delta E_1 = \frac{1}{8}\tilde{V}(0) + \frac{1}{8}\tilde{V}\left(\vec{\mathbf{k}_1}\right) \tag{4.15}$$

$$\Delta E_1 = \frac{1}{8}\tilde{V}(0) + \frac{1}{8}\tilde{V}\left(\vec{\mathbf{k}_2}\right), \tag{4.16}$$

and may be obtained from DFT calculations as difference between the total energies of corresponding superstructures and the total energy of the mixture of constituents given by equation 4.14. From equation 4.9 it follows that

$$\tilde{V}\left(\vec{\mathbf{k}_1}\right) = -4\tilde{V}\left(\vec{R_1}\right) + 6\tilde{V}\left(\vec{R_2}\right) - 8\tilde{V}\left(\vec{R_3}\right) + \ldots, \tag{4.17}$$

$$\tilde{V}\left(\vec{\mathbf{k}_2}\right) = -6\tilde{V}\left(\vec{R_2}\right) + 12\tilde{V}\left(\vec{R_4}\right) + \ldots, \tag{4.18}$$

$$\tilde{V}\left(0\right) = 12\tilde{V}\left(\vec{R_1}\right) + 6\tilde{V}\left(\vec{R_2}\right) + \ldots \tag{4.19}$$

With the approximation of interactions in the two nearest neighbours on the Ce/Tb sub-lattice this yields

$$\Delta E_1 = \tilde{V}\left(\vec{R_1}\right) + \frac{3}{2}\tilde{V}\left(\vec{R_2}\right) \tag{4.20}$$

$$\Delta E_2 = \frac{3}{2}\tilde{V}\left(\vec{R_1}\right). \tag{4.21}$$

Calculated values of ΔE_1 and ΔE_2 are 0.228 eV and 0.056 eV respectively. Their positive sign means that both superstructures are energetically unfavourable in comparison with a mixture of constituents, CeO_2 and TbO_2, and do not exist. with these values obtained, however, it is possible to calculate $\tilde{V}(0)$, which is responsible for the behaviour of disordered Ce/Tb lattice. Solving equations 4.20 – 4.21, and substituting the result into equation 4.19, a value for $\tilde{V}(0) = 1.210$ eV is obtained.

Equations 4.12 and 4.13, for a case of absolutely disordered structures ($\eta_1 = 0,\ \eta_2 = 0$), are similar to a model of regular solid solution used for construction of phase diagrams in [185]. In this model, the free energy of mixing for the disordered solid solution is cast as $\Delta F_{mix} = \Delta E - T\Delta S$, where ΔS is the configurational entropy of mixing, and the mixing energy is $\Delta E = L \cdot c \cdot (1 - c)$. Here, $L = -\frac{1}{2}\tilde{V}(0)$.

This shows that a model which assumes that a mixture of CeO_2 and TbO_2 will have a fluorite structure with Ce/Tb atoms distributed over fcc sub-lattice, requires only two calculations of *absolutely ordered* structures to compute energy parameter that determines mixing energy of an absolutely disordered $(Ce_{1-c}Tb_c)O_2$ solid solution. A second important assumption that allows to calculate the free energy of mixing, and to predict solubility at different temperatures and concentrations, c, is based on a work by P. A. Žguns *et al.* [150], in which a decomposition of $(Ce_{1-c}Gd_c)O_{2-c/2}$ solid solutions was studied, using a cluster expansion method. Their finding is that cluster interaction parameters $V_{AA}, V_{BB}, \text{and} V_{AB}$ do not depend on the dopant concentration. Therefore, it is reasonable to assume that for $\vec{k_s} = 0$ (i.e. no vector in the reciprocal space can be symmetrized with respect to dopant distribution in the lattice), $\tilde{V}(0)$ is also concentration-independent, and that $L = const$ for the whole range of concentration.

Figure 4.3 presents mixing energy (ΔE), configuration entropy of mixing term ($-T\Delta S$), and the free energy of mixing ΔF_{mix} as functions of Tb concentration at $T = 1000$ K. The function of ΔF_{mix} is concave in the entire concentration range, thus at temperature(s) where fluoride structures of both CeO_2 and TbO_2 exist, an unlimited solubility of Tb in CeO_2 should be observed. According to binary Tb–O and Ce–O phase diagrams, this temperature region is above ca. 700 °C.

4.3.6 Reduced Tb and oxygen vacancy in CeO_2

Not only is Tb absolutely soluble in CeO_2, it can also exist in either 3+ or 4+ oxidation state. Table 4.9 shows two distinct magnetic moments of Tb ion in a CeO_2 supercell. Both solutions require Tb to be located at a low-symmetry site, and their energy difference is only 0.07 eV/cell in favour of the +4 oxidation state. This assertion of mixed OS coexistence is consistent with an experimental observation that in $Ce_{1-c}Tb_cO_{2-\delta}$, lattice constant's dependence on c is nicely approximated by

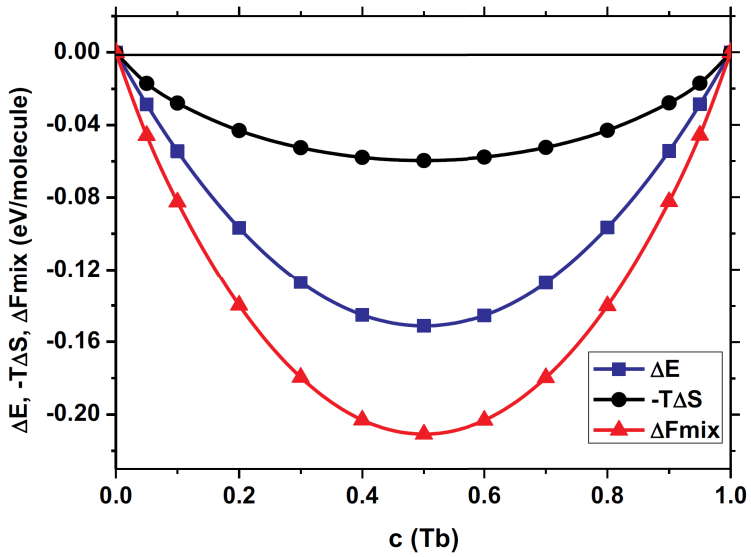

Figure 4.3: Thermodynamic parameters of CeO_2/TbO_2 mixture as functions of Tb concentration at $T = 1000$ K, adopted from [155]

averaging theoretically obtained dependencies for cases of pure Tb^{3+} and Tb^{4+} [151].

Naturally, Tb +3 has to be compensated by an electronic hole. In these calculations, its complementary hole is delocalized over the entire supercell, leading to an enhanced Fermi energy occupation by O $2p$ states, and, thus, enhanced hole conductivity. Increased hole conductivity is also consistent with the electrical conductivity measurements from the literature [151].

It was shown in the previous section (4.2) that in case of undoped $CeO_{2-\delta}$, localization of two electrons on $4f$ orbitals of two nearest Ce cations, corresponding to formation of a small polaron, is the most favourable case w.r.t. the defect formation energy, about 0.61 eV lower in energy than the large radius polaron with localization on all four Ce ions. So, the minimum energy state was observed for $S_z = 1$ at low symmetrical C_s(or, alternatively, at C_{2v}-position) of V_O^{+2} in the 81-atom supercell, with $\Delta G_F^{V_O^{+2}} = 4.10$ eV at 0 K (table 4.6). Repeating this calculation with PBE+U functional, a PW basis set, μ_O as defined in equation 4.3 and shown in fig. 4.4, and with p_{O_2} yielded $\Delta G_F^{V_O^{+2}} = 3.10$ eV (all at $T = 0$ K). At $T = 400$ K in undoped $CeO_{2-\delta}$ $\Delta G_F^{V_O^{+2}} = 2.64$ eV.

In Tb-doped CeO_2 formation of V_O^{+2} complicates electronic interactions, but it also simplifies behaviour of Tb ion. Tables 4.10 and 4.11 summarise these results. In both tables distance between an ion and a vacancy refers to an unrelaxed fluorite structure with lattice constant 5.41 Å. Distance between metal ions is measured after a full structure relaxation, S_z is the spin projection, μ is the magnetic moment, q is the atomic charge, and $\Delta G_F^{V_O^{+2}}$ is the Gibbs formation energy of an oxygen vacancy, calculated w.r.t. the chemical potential of oxygen μ_O at T = 400 K, and $p_{O_2} = p^0$ (eq. 4.3, and fig. 4.4). Table 4.10 lists results for systems, in which V_O^{+2} is among the nearest neighbours of Tb ($d(Tb - V_O) = 2.34$ Å). Table 4.11 lists results for the next nearest neighbours ($d(Tb - V_O) = 4.49$ Å), all of which have the same site symmetry, C_s.

First important conclusion drawn from this data is that presence of Tb ion lowers the $\Delta G_F^{V_O^{+2}}$ by a factor of 4: 0.66 eV (the most favourable case, table 4.10) vs. 2.64 eV for an undoped system.

Second, the key factor determining the magnitude of $\Delta G_F^{V_O^{+2}}$ is Tb oxidation state. All solutions with μTb > 6.2 μB (Tb +4) have very high formation energies, regardless of distances, spin orientation, and vacancy–ion distance. Third, localization on next-nearest Ce ions w.r.t. oxygen vacancy is more favourable than on the nearest neighbours or more remote metal ions.

The most favourable solution corresponds to a system in which oxygen vacancy is located next to Tb, and residual electrons localize on Tb and on a Ce ion from O's 3rd coordination sphere in an antiferromagnetic alignment.

Table 4.10: Effect of local symmetry and electronic localization on the energetics of oxygen vacancy formation near Tb ion †

Point symmetry	d(Ce^{+3}-V_O), Å	S_z	d(Tb-Ce^{+3}), Å	μTb, μB	qTb, e	μCe, μB	qCe, e	$\Delta G_F^{V_O^{+2}}$, eV
C_s	4.59	1	6.76	6.06	2.09	-0.93	2.13	0.66
C_s	$2\times$ 4.59	$-1/2$	$2\times$ 6.76	6.06	2.09	2×-0.51	2.31	1.00
C_{3v}	2.34	2	4.17	6.04	2.17	$3\times$ 0.37	2.3	1.10
C_s	2.34	1	4.13	6.03	2.09	-0.93	2.09	1.16
C_{3v}	$3\times$ 2.34	-1	$3\times$ 4.18	6.07	2.08	3×-0.35	2.32	1.28
C_{3v}	—	1/2	—	6.05	2.09	—	—	1.49
C_s	$2\times$ 4.56	1	$2\times$ 5.60	6.24	2.16	$2\times$ 1.00	2.14	2.19
C_{3v}	$3\times$ 4.56	3/2	$3\times$ 5.60	6.24	2.17	$3\times$ 0.70	2.28	2.43
C_{3v}	$3\times$ 2.34	3/2	4.18	6.25	2.17	$3\times$ 0.71	2.22	2.58
C_{3v}	$3\times$ 4.49	$-3/2$	$3\times$ 6.92	6.35	2.20	3×-0.47	2.33	2.74

† $d(Tb - V_O) = 2.34$ Å

Table 4.11: Energetics of oxygen vacancy formation at the next nearest site w.r.t. Tb ion †

d(Ce^{+3}-V_O), Å	S_z	d(Tb^{+3}-Ce^{+3}), Å	μTb, μB	qTb, e	μCe, μB	qCe, e	$\Delta G_F^{V_O^{+2}}$, eV
5.87	1	4.12	6.12	2.09	0.97	2.09	0.84
4.49	1	7.79	6.05	2.12	-0.97	2.14	0.95
2.34	1	6.76	6.05	2.12	-0.88	2.12	1.04
2.34	1	5.43	6.05	2.12	0.93	2.12	1.16
$2\times$ 4.58	-1	$2\times$ 6.75	6.05	2.12	2×-0.51	$2\times$ 2.31	1.21
$2\times$ 4.49	3/2	$2\times$ 6.74	6.05	2.12	$2\times$ 0.52	$2\times$ 2.31	1.25
$3\times$ 2.34	-1	$3\times$ 4.18	6.07	2.08	3×-0.35	$3\times$ 2.32	1.27

† $d(Tb - V_O) = 4.49$ Å; C_s symmetry

Calculated densities of states (DOS) show that reduced Ce +3 ions produce a new peak in the band gap (fig. 4.5). This is an electron trap induced by V_O^{+2}, located ~1.0 eV below the bottom of unoccupied Ce 4*f* band (the O 2*p*–Ce 4*f* band gap is 2.1 eV). Recombination of trapped electrons with holes in the valence band may explain the observed increase of luminescence in CeO_2 nanoparticles when doped with Tb [187, 188].

Results presented in this section are published in ***[A2]*** and ***[A3]*** . The author has performed

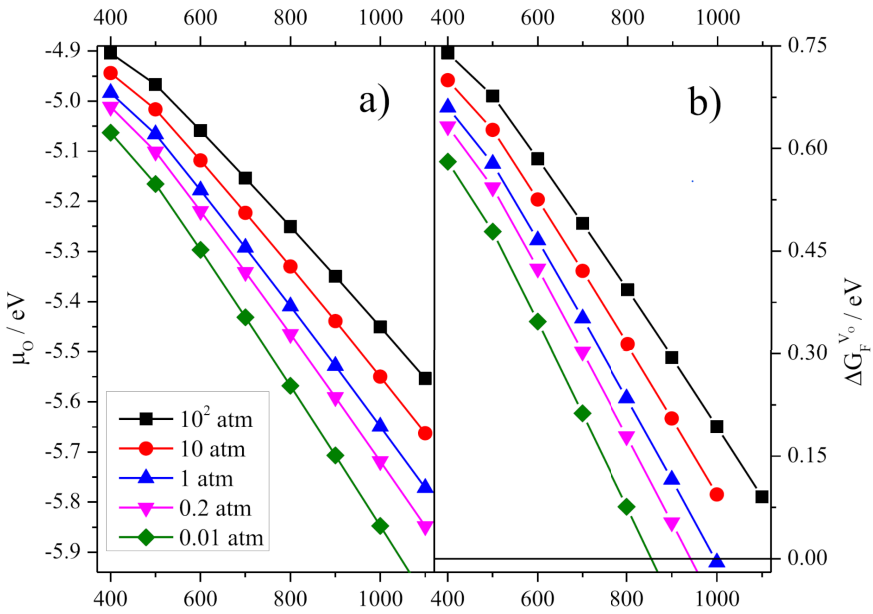

Figure 4.4: (a) oxygen chemical potential, as defined by equation 4.4, calculated from metal oxides; and (b) formation energy of $\Delta G_F^{V_O^{+2}}$ for the lowest-energy case, presented as functions of temperature; adopted from [186]

most calculations of cerium and terbium oxides, all calculations on Tb-doped CeO_2, has conducted all calculations related to parametrisation and validation of the model, has gathered the data, has contributed texts and figures to papers.

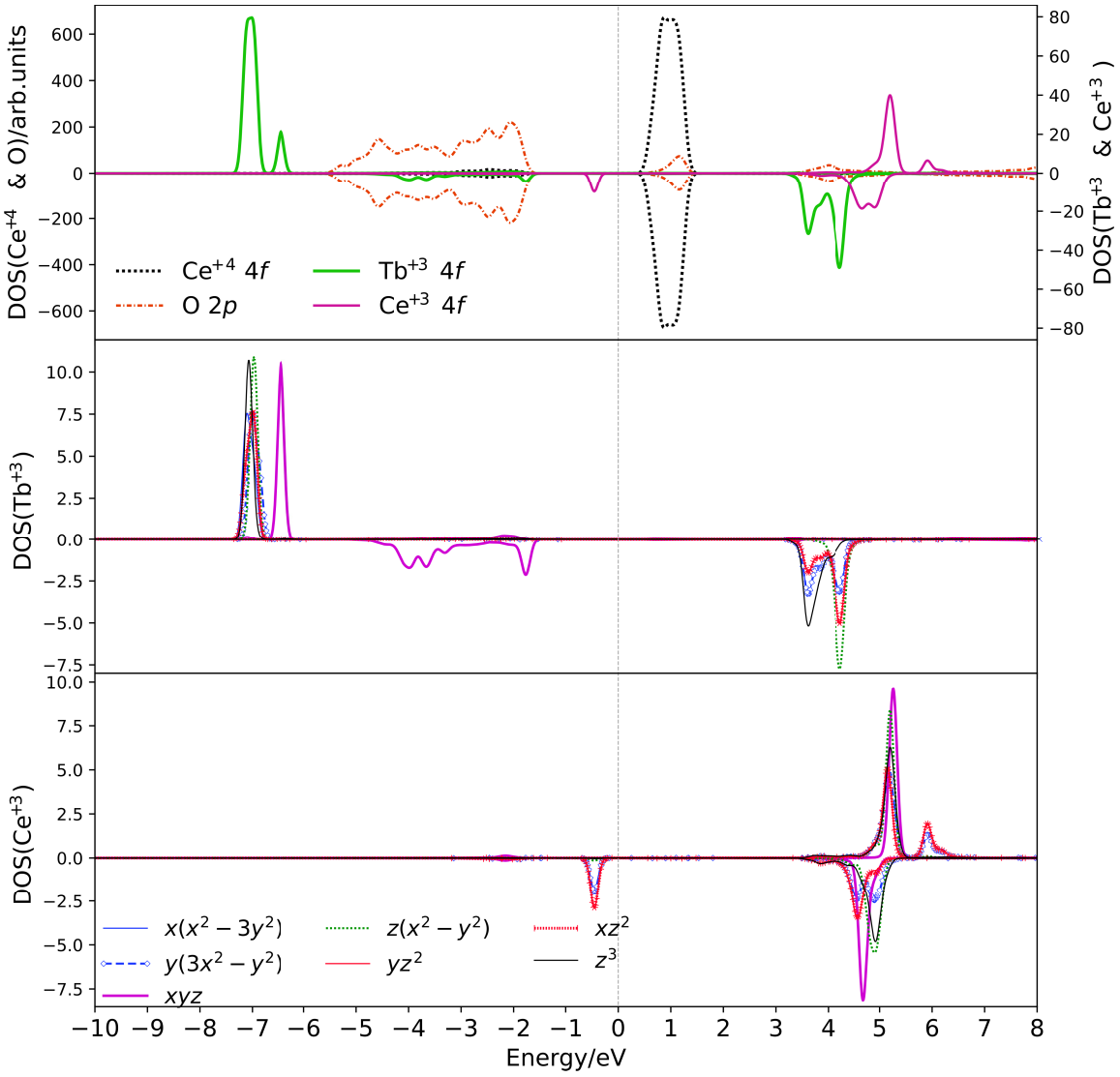

Figure 4.5: DOS of the groundstate solution for CeO_2:Tb+V_O^{+2} (case with=0.66 eV in Table 4.10), projected on $4f$ orbitals of Tb^{+3}, Ce^{+3}, Ce^{+4} and $2p$ orbitals of O, and its decomposition into all contributions from the $4f$ orbitals. Negative DOS values correspond to spin down electrons. Fermi energy is taken as zero. Adopted from [186]

5.THE CASE OF ZINC OXIDE

5.1 Introduction

The primary motivation for this investigation is the work by Mārtiņš Zubkins and his colleagues [189, 190]. They have shown that ZnO thin films, when doped with Ir, tend to become amorphous upon reaching a critical Ir concentration. Near this threshold, above 7 % Ir, the samples become amorphous in x-ray diffraction and EXAFS spectra, while computationally fitted structures of EXAFS spectra show the presence of 6-coordinated iridium ions [191]. Simultaneously, the samples start having a measurable electrical conductivity, and a sign change of the Seebeck coefficient is observed.

In the present study using the density functional theory (DFT) calculations we verify whether explanation for this effect can be attributed to interstitial oxygen defects, and test a hypothesis that 6-coordinated Ir is crucial for electrical properties observed in iridium-doped ZnO thin films.

5.2 Supercell selection

ZnO crystallizes in the wurtzite structure (space group No.186, $P6_3mc$), making it impossible to embed a six-coordinated Ir in a ZnO matrix by simply placing Ir atom in a regular lattice site or by substituting a Zn atom. Therefore, a model of a six-coordinated Ir requires presence of interstitial oxygen atoms in the wurtzite structure. The placement of these atoms is an important input parameter, and the entire system of atoms is sensitive to its changes, see section 5.5.1 for specific results related to the initial placement of interstitial atoms.

The inclusion of interstitial atoms disrupts the crystalline structure and is not compatible with symmetry operations of the space group to which wurtzite structure belongs. Ultimately, two supercells were chosen, P4(16), and P48(192), representing Ir concentrations of 12.5% and 1.04%, respectively. These supercells correspond to the following transformation matrices applied to the primitive cell of wurtzite type: $\left(\begin{smallmatrix}2&0&0\\0&2&0\\0&0&1\end{smallmatrix}\right)$ for P4(16), and $\left(\begin{smallmatrix}4&0&0\\0&4&0\\0&0&3\end{smallmatrix}\right)$ for P48(192). Concentration in P4(16) supercell corresponds to the amorphization/conductivity threshold described in [190], whereas low concentration of P48(192) is chosen as a control sample for validating the model.

5.3 Computational details

5.3.1 Basis set

ZnO is a well-described, well-known material, with readily available, tested computational schemes. To reproduce band gap of ZnO it is necessary to use either a large +U correction, or a hybrid exchange-correlation functional. In this work, for the sake of comparing results to available computational data, it is practical to use a hybrid XC functional with a basis set of gaussian-type orbitals. Basis set for Ir and O was taken from Ping *et al.* [192]. This basis set was complimented by a basis set for Zn taken from Gryaznov *et al.* [193]. The latter was modified by optimizing exponent values of the two most diffuse orbitals: one from the *sp* series and one from the *d* series. These values were optimized with respect to the total electronic energy of the system with constant volume and atomic positions. The convergence limit of this procedure, based on the Powell's conjugate direction method

and used as implemented in the OPTBAS [134] interface to CRYSTAL, was set to 10^{-5} Hartree.

Final basis set is listed in table 5.1, and its performance in describing selected bulk properties of ZnO is summarised in table 5.2. In this table ΔX is the difference between an experimental and calculated value, and δX is the relative error:

$$\delta X = 100\% \times \frac{X_{exp} - X_{calc}}{X_{exp}} \tag{5.1}$$

5.3.2 DFT parameters

All calculations were made using public release of CRYSTAL17 ver. 1.0.2 [11]. Tolerance factors of 7, 7, 7, 9, and 30 for the Coulomb and exchange integrals were used. The SCF convergence threshold for the total electron energy was set to 10^{-7} Hartree, and the threshold for change in energy between consecutive geometry optimization steps was set to 10^{-7} Hartree. All calculations of defective structures in the neutral supercells were spin-polarized and did not include the spin–orbit effects; the use of symmetry operations was explicitly omitted.

PBE0 exchange-correlation functional was used, as the employed basis sets (table 5.1) were optimized for and have been used on the compounds of interest with this functional [192, 193]. For calculating vibrational frequencies the frozen phonon method (direct method) [127, 128] was used, and the SCF convergence threshold for the total electron energy was adjusted to 10^{-9} Hartree. In all calculations, reciprocal space was sampled with the following Monkhorst-Pack k-point grids: $4\times4\times4$ for P4(16) supercells, and $2 \times 2 \times 2$ for P48(192).

5.3.3 O incorporation

This study's principal object of interest is a six-coordinated Ir–O complex embedded in ZnO matrix. However, since it is impossible to obtain a six-coordinated Ir by simply placing it anywhere in ZnO structure, a presence of interstitial O atoms is necessary. Relaxation of atomic positions is highly sensitive to initial placement of atoms, and may lead to various stable solutions. To compare obtained configurations of interstitial O atoms around Ir, O incorporation energy $E_{inc}(O_i)$ is used:

$$E_{inc}(O_i) = E(O_i) - E(Ir) - E(O_2), \tag{5.2}$$

where $E(O_i)$ is the total electronic energy of the supercell with two O_i atoms and an Ir atom; $E(Ir)$ is the total electronic energy of the supercell with only $Ir^{+2}O_4$[1] without O_i; $E(O_2)$ is the total electronic energy of an oxygen molecule.

A negative value of $E_{inc}(O_i)$ means that incorporation is energetically favourable. All total electronic energies in equation 5.2 are calculated using the same basis set and exchange–correlation functional.

[1]Here, a 2+ oxidation state of Ir is set by definition: Ir is forced to substitute a 2+ Zn ion in a ZnO matrix, with the same surroundings as Zn ion. This oxidation state, while theoretically possible, is not an optimal OS of iridium.

Table 5.1: Final optimized basis sets. *Emphasized coefficients* have been optimized with the OPTBAS program

Ir	Zn	O
277 12	30 8	8 5
INPUT	0 0 8 2.0 1.0	0 0 7 2. 1.
17 5 6 5 5 5 0	417016.5 0.00023	7817.0000000 0.0011760
823.5880147 -0.1578014 -1	60504.2 0.00192	1176.0000000 0.0089680
364.6613336 -1517.5270446 0	12907.9 0.01101	273.2000000 0.0428680
55.7082801 -316.5306529 0	3375.74 0.04978	81.1700000 0.1439300
12.0464544 -91.8880941 0	1018.11 0.16918	27.1800000 0.3556300
3.5120610 -9.2241773 0	352.55 0.36771	9.5320000 0.4612480
188.0490770 3.1578014 -2	138.19 0.40244	3.4140000 0.1402060
340.4194712 26.8322577 -1	57.851 0.14386	0 0 2 2. 1.
128.2373673 800.4250007 0	0 1 6 8.0 1.0	9.5320000 -0.1541530
33.8644961 369.4050683 0	1079.2 -0.00620 0.00889	0.9398000 1.0569140
4.7560005 242.4171899 0	256.52 -0.07029 0.06384	0 0 1 0. 1.
3.9649974 -118.2173282 0	85.999 -0.13721 0.22039	0.2846000 1.0000000
289.7291139 2.1578014 -2	34.318 0.26987 0.40560	0 2 4 4. 1.
87.4633789 61.9678610 -1	14.348 0.59918 0.41370	35.1800000 0.0195800
30.4363766 269.0581986 0	4.7769 0.32239 0.34974	7.9040000 0.1242000
4.0553412 231.1654793 0	0 1 4 8.0 1.0	2.3050000 0.3947140
3.5525341 -133.6952667 0	60.891 0.00679 -0.00895	0.7171000 0.6273760
136.4017106 3.1578014 -2	25.082 -0.08468 -0.03333	0 2 1 0. 1.
95.0776925 45.9349803 -1	10.620 -0.34709 0.08119	0.2137000 1.0000000
49.2258410 359.0344668 0	4.3076 0.40633 0.56518	
15.0874145 176.4740119 0	0 1 1 2.0 1.0	
4.0405764 54.5155286 0	1.6868 1.0 1.0	
127.3507908 3.9546197 -2	0 1 1 0.0 1.0	
66.2364374 52.9773655 -1	0.62668 1.0 1.0	
34.4299229 274.8643383 0	0 1 1 0.0 1.0	
10.1995721 137.2047338 0	*0.12729378183255* 1.0 1.0	
2.5409702 14.8633305 0	0 3 4 10.0 1.0	
0 0 1 2. 1.	57.345 0.02857	
2.3500000 1.0000000	16.082 0.15686	
0 0 1 2. 1.	5.3493 0.38663	
1.5820000 1.0000000	1.7548 0.47766	
0 0 1 0. 1.	0 3 1 0.0 1.0	
0.5018000 1.0000000	*0.49499382987434* 1.0	
0 0 1 0. 1.		
0.2500000 1.0000000		
0 2 1 6. 1.		
2.7920000 1.0000000		
0 2 1 0. 1.		
1.5410000 1.0000000		
0 2 1 0. 1.		
0.5100000 1.0000000		
0 2 1 0. 1.		
0.0980000 1.0000000		
0 3 1 7. 1.		
1.2400000 1.0000000		
0 3 1 0. 1.		
0.4647000 1.0000000		
0 3 1 0. 1.		
0.1529000 1.0000000		
0 4 1 0. 1.		
0.9380000 1.0000000		

Table 5.2: Basic properties of ZnO obtained with different XC functionals and basis sets

	a, Å	Δa, Å	δa	c, Å	Δc, Å	δc	E_G, eV	ΔE_G, eV	δE_G
Exp. [74]	3.249			5.204			3.44		
HSE06 [194] pob-TZVP-r2	3.262	-0.013	-0.40%	5.115	0.089	1.71%	2.75	0.69	20.06%
PBE0 [194] pob-TZVP-r2	3.261	-0.012	-0.37%	5.114	0.09	1.73%	3.42	0.02	0.58%
PBE0 [193] 86-411d31G	3.26	-0.011	-0.34%	5.22	-0.016	-0.31%	3.56	-0.12	-3.49%
HSE PW [193]	3.25	-0.001	-0.03%	5.25	-0.046	-0.88%	2.5	0.94	27.33%
PBE0 [192] pob-DZVP	3.257	-0.008	-0.25%	5.1981	0.006	0.11%	3.46	-0.025	-0.73%

5.3.4 Thermoelectric parameters

This study's principal *quality* of interest is an alleged emergence of p-type conductivity in Ir-doped ZnO, observed as positive values of Seebeck coefficient [190]. In the original experiment performed by Zubkins *et al.* the electrical transport of the thin films was studied by measuring the DC electrical conductivity at room temperature and as a function of temperature between 90 K and 330 K. Seebeck coefficient was determined by controlling a temperature difference across the sample and measuring the resulting voltage [190].

In these calculations, $\tau = 10$ fs was used, which is a conservative estimate for a system leaning towards conductivity (see section 2.5.2 and eq. 2.6). Reported values of τ, obtained from charge carrier mobility data, range from 17 to 57.9 fs for carrier concentrations $\sim 10^{16}\text{cm}^{-3}$ [80, 195]. As a scalar positive pre-factor, precise value of τ does not affect behaviour of the transport distribution function, and only impacts the scale of values. For convenience, in analysing results, the Fermi level is shifted by the valence band maximum (E_{VBM}): $\mu_F = \mu - E_{VBM}$.

One can clearly see that the calculated conductivity and Seebeck coefficient are not strictly equivalent to experimentally obtained data. In an experimental setup the Seebeck coefficient S is calculated at zero current density from measured thermoelectric voltage ΔV and measured temperature difference ΔT:

$$S = -\frac{\Delta V}{\Delta T}. \tag{5.3}$$

When obtained from equations 2.9 and 2.8, S is a tensor. Its reduction to a scalar is described in section 5.4.3.

5.4 Validating the model and defining baselines

5.4.1 Oxidation state of iridium

Calculation parameters are validated by calculating parent structures, in this case, binary oxides of the constituent metal ions and zinc-iridium spinel-like compound. This analysis is used to establish model's response to different oxidation states of Ir. Reference materials are: ZnO, IrO_2 (formal oxidation state of Ir is 4+), Ir_2O_3 (Ir3+), and $ZnIr_2O_4$ (Ir3+). All these materials are modelled in their common reported structures: tetragonal (space group $P4_2/mn$, rutile structure) for IrO_2,

rhombohedral (space group $R\bar{3}c$, corundum structure) for Ir_2O_3, and cubic (space group $Fd\bar{3}m$, spinel structure) for $ZnIr_2O_4$. At the time of writing and to author's best knowledge, the preparation of single-crystal Ir_2O_3 is not yet reported. However, its presence in IrO_2 powders was discussed in refs. [196] and [197], and corundum $Ir_2O_3(001)$ surface oxide was synthesized at high oxygen pressure [198] in the oxidation of the Ir(111) surface. Besides, several papers describe and report measurements of properties of devices based on corundum-structured Ir_2O_3, although without discussing the actual structure of the material [199, 200].

Good agreement with available experimental data in tables 5.3 and 5.4 indicates that the model is able to reproduce main structural and electronic properties of these compounds, and is robust with respect to changes of the local structure of atoms. Another purpose of this comparison, besides establishing a correspondence between model and experiment, is to define a baseline for interpreting mixed cases of Ir–O complex embedded in ZnO. Experimental data on parent structures defines target values for parameters that are dependent on composition, or depend on structure, for instance, oxidation states (charges) of constituent atoms, and conductivity (resistivity).

Table 5.3: Calculated and experimental structural properties of parent compounds

	$a; c$, Å	$a; c$ exp, Å	d_{Me-O}, Å	d_{Me-O} exp, Å	Ref.
ZnO	3.257; 5.200	3.2494; 5.2054	short: 1.978 long: 1.986	short: 1.974 long: 1.990	[201]
IrO_2	4.471; 3.169	4.505; 3.159	short: 1.942 long: 1.999	short: 1.94-1.960 long: 1.999-2.00	[202, 203]
Ir_2O_3	5.213; 13.848	5.214-5.438; 13.846-14.737	short: 2.053 long: 2.085		[204]
$ZnIr_2O_4$	8.633	8.503-8.507	2.069		[205]

Table 5.4: Calculated and experimental electronic properties of parent compounds

	ΔE_G, eV	ΔE_G, exp, eV	q_{Ir}, e	μ_{Ir}, μ_B	q_O, e	μ_O, μ_B
ZnO	3.45	3.44 [206]				
IrO_2	None	None[192]	1.712	0.625	-0.856	0.171
Ir_2O_3	3.39		1.241	0.000	-0.824	0.000
$ZnIr_2O_4$	3.44	2.97[205][i] 3.30[205][i]	1.067	0.000	-0.824	0.000

i. Experimental optical band gap

5.4.2 Peroxide complexes of iridium

According to the original paper by Zubkins *et al.* [190], among other changes at the critical Ir concentration, there also appears an intense Raman band at 720 cm^{-1}, which the authors ascribe to peroxide moiety, a feature that is not yet discussed, and is absent from tables 5.3 and 5.4. It is difficult to gather information on metallic peroxides because they are elusive compounds that are difficult to make and characterize. They are reactive, unstable and dangerous to handle, containing vast amounts of potential energy in the form of O–O bonds. Luckily, some data exists for zinc peroxide, ZnO_2. Bulk iridium peroxide is absent from literature. However, there are some data on organic compounds that contain $Ir(O_2)$ fragment, summarised in table 5.5. This data enables differentiation of Ir–O bonds within the Ir–O complex, and provides a test for presence of peroxide in ZnO-embedded Ir–O complexes.

Table 5.5: Reported properties of O_2^{2-} fragment in select compounds

	d_{Ir-O}, Å	d_{O-O}, Å	νO–O, cm^{-1}	Ref.
ZnO_2	2.068–2.110	1.469–1.677	750–850, Raman	[207–209]
$[Ir(O_2)(PMe_3)_4]Cl$	2.056–2.073	1.475(3)–1.481(5)	—	[210]
$(^{t\mathrm{Bu}}\mathrm{PCP})\mathrm{Ir}(\eta^2\text{-}O_2)_2$	2.008–2.040	1.54(3)	893.5, IR	[211]
trans–$[Ir(4\text{-}C_5F_4N)(O_2)(CN\mathit{t}Bu)(P\mathit{i}Pr_3)_2]$	2.0508–2.0301	1.472(2)	833 (IR); 788 (Raman, ^{18}O)	[212]

5.4.3 Conductivity baselines

Whereas experimentally determined electrical conductivity and Seebeck coefficient are scalars, when calculated from first principles, they are tensors. Experimental values are measured for real samples, and are, effectively, averaged over many crystalline domains. Calculated thermoelectrical parameters are, effectively, expressed as functions of chemical potential and direction (section 5.3.4, equations 2.6–2.9). Here, to reduce dimensionality of these objects to a simple function of the $f(x)$ type, thermoelectric parameters are presented as their largest value (by absolute value) for a given value of chemical potential μ.

The results of calculations on ideal ZnO and ZnO with intrinsic defects (Zn vacancy for a p-type defect and O vacancy for a n-type defect) define a baseline for conductivity in this material. According to [46], within the selected computational scheme, the principal quality that determines reliability of theoretically estimated conductivity, is the band gap's value. Other computational parameters, such as the choice of exchange-correlational functional or basis set have little influence on the transport distribution function. Figure 5.1 shows thermoelectrical properties of several idealized systems: pure ZnO (a), ZnO with a neutral Zn vacancy – an idealized case of p-type defect (b), ZnO with O vacancy – an idealized case of n-type defect (c), a complex defect of an interstitial O coupled with a Zn-substituting O (d), and two systems representing iridium – Ir_2O_3(e) and IrO_2(f).

In intrinsic semiconductors the bands may conduct in parallel, and the observed value and sign of the Seebeck coefficient depends on the majority charge carrier: positive for hole-dominated conduction and negative for electron-dominated conduction. This results in a crossover behaviour seen in figure 5.1(a–d). The crossover is in the middle of band gap. Undoped ZnO is a typical wide-gap semiconductor, and as such its conductivity diagram is a classical "V" shape, and its Seebeck coefficient shows a mid-gap p-n switching pattern, as the chemical potential increases, figure 5.1(a).

A neutral zinc vacancy, by definition a p-type defect, establishes the baseline pattern for this type of conductivity: lower absolute values of Seebeck coefficient, an additional switching mode due to an acceptor level near the top of valence band, and a local maximum of conductivity corresponding to positive range of Seebeck coefficient, figure 5.1(b). On the other hand, n-type semiconductors, as in the case of interstitial O and a complex O–O defect, either exhibit intrinsic semiconductor behaviour, simultaneously narrowing the band gap, 5.1(c), or have a defect level close to the bottom of conduction band, with the conductivity maximum matching a negative Seebeck coefficient, figure 5.1(d). Finally, two iridium compounds, Ir_2O_3(e) and IrO_2(f), represent, respectively, a non-conductive and conductive Ir systems. A conductive system does not have a distinct conductivity well across the entire range of chemical potential, and is characterized by low values of Seebeck coefficient.

To interpret results obtained with this model, it is important to keep in mind that under real temperatures electrons in the valence band will be thermally excited, and as a result the potential will increase with respect to the level calculated at 0 K. In figure 5.1 this can be seen as, for instance, slower-than-exponential decay of conductivity in Ir_2O_3(e). A region of chemical potential where switch to pure exponential decay (transition from a curve to a straight line) may therefore be used to assess the position of Fermi level at a given temperature.

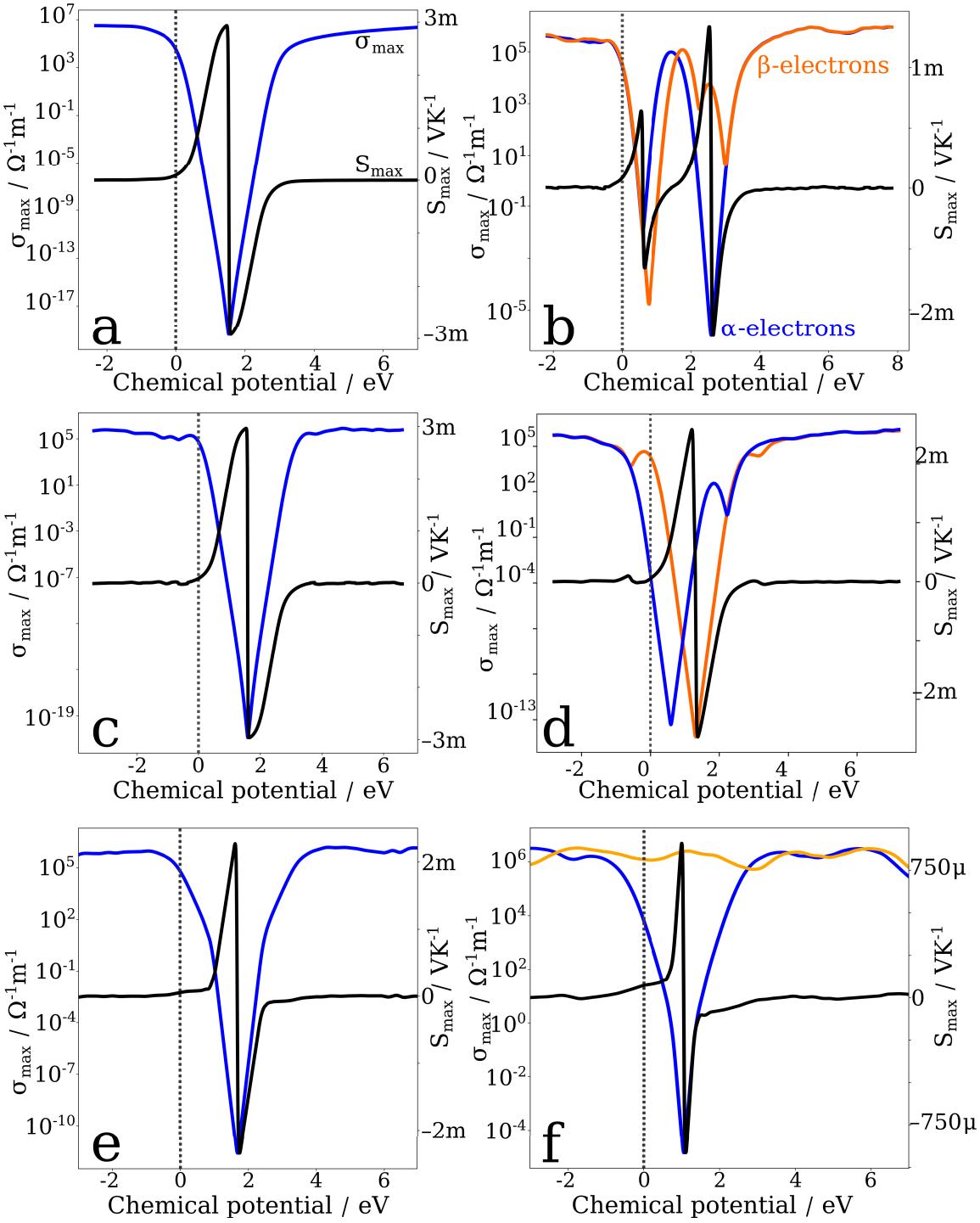

Figure 5.1: Conductivity and Seebeck coefficients of idealized systems at $T = 300$ K. Dashed grey line marks 0 eV = VB top = $E_{Fermi}(0\ K)$. Solid black lines are Seebeck coefficients $S_{max}(\mu)$.
a: pure ZnO;
b: ZnO with Zn vacancy, p-type conductivity pattern;
c: ZnO with O vacancy, semiconducting pattern;
d: ZnO with O–O defect, n-type conductivity pattern;
e: pure Ir_2O_3, a semiconductor;
f: pure IrO_2, electrically conductive

5.5 Structural description

5.5.1 Relaxation and Ir–O complexes

It was posed in section 5.2 that the ZnO-Ir-O system is very sensitive to the initial placement of interstitial oxygens. Table 5.6 sums up some of the possible solutions, all obtained for the same supercell, with the same number of atoms, with two interstitial oxygen atoms.

Table 5.6: Ir–O complexes in P4(16) supercell

Coordination number	d_{Ir-O}, Å	q_{Ir}, e	μ_{Ir}, μ_B	d_{O-O}, Å	νO–O, cm^{-1}	$E_{inc}(O_i)$, eV
6	1.893–1.972	1.325	0.514	—	—	-5.15
6	1.825–2.125	1.383	1.569	—	—	-4.95
6	1.844–2.051	1.415	1.542	—	—	-4.92
6	1.853–2.046	1.384	0.562	—	—	-4.84
6	1.850–2.085	1.366	-0.003	—	—	-4.82
5	1.828–2.024	1.095	0.695	1.540	810	-4.37
4	1.846–1.920	1.193	1.795	1.470	942	-3.77
5	1.854–2.186	1.282	2.236	—	—	-3.49
4	2.136–2.176	0.751	2.530	—	—	0[i]

i. This is $Ir^{2+}O_4$, or $E(Ir)$ from eq. 5.2, no interstitial oxygen atoms. Ir incorporation energy is ca. +6 eV w.r.t. pure ZnO.

This table shows the breadth of possibilities that Ir has in ZnO environment. First, negative incorporation energies show that Ir-doped ZnO requires interstitial oxygen atoms. Second, while 6-coordinated Ir–O complexes are energetically more favourable than lower-coordinated alternatives, these are not the guaranteed solution. Ir is able to change its oxidation state and its magnetic configuration, forming low-spin, high-spin, and intermediate-spin complexes. This is reflected in the first 6 rows of table 5.6, where the chief differences in $E_{inc}(O_i)$ are attributed to different spin-states of Ir, with another factor being other atoms' electronic localization: for instance, 6$^{\text{th}}$ row with $E_{inc}(O_i) = -4.82$ eV, while having unremarkable atomic charges, represents a completely delocalized solution.

Formation of peroxide moiety was not observed for 6-coordinated Ir–O complex (at a fixed concentration of interstitial oxygen atoms), but peroxide solutions, while energetically costly, are nonetheless possible. The costs associated with formation of this defect are both energetic and structural: presence of peroxide heavily distorts wurtzite lattice of ZnO, see figure 5.2. There, Ir-centred radial distribution functions are plotted for interstitial-oxygen-lacking $Ir^{2+}O_4$ (a), 4-coordinated peroxide-forming Ir–O (b), 5-coordinated Ir–O with peroxide (c), and lowest-energy 6-coordinated Ir–O (d).

It is apparent that among the 4 structures, solutions without peroxide, figure 5.2(a,d), are more ordered, with clear, sharp peaks. At the same time, 6-coordinated Ir–O, figure 5.2(d) shows clear signs of structural deterioration, with broader, less resolved and lower peaks. On the contrast, peroxide solutions, figure 5.2(b,c), already appear amorphous in the 3–6 Å region, with convoluted peaks in the 2–4 Å region, indicating that Ir's next-neighbouring Zn–O bonds have large variances.

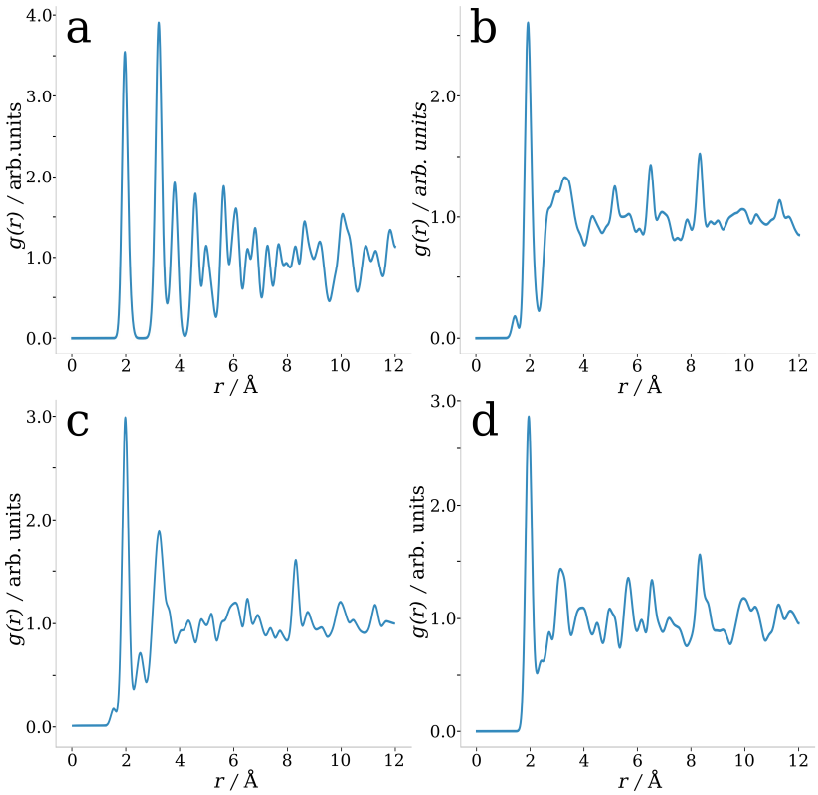

Figure 5.2: Ir-centred radial distribution functions of Ir–O complexes in ZnO
a: ZnO + $Ir^{2+}O_4$ [12.5%];
b: 4-coordinated Ir–O with peroxide
c: 5-coordinated Ir–O with peroxide
d: groundstate 6-coordinated Ir–O

Results presented in this section are well in line with experimentally observed behaviour of this system: not only is 6-coordinated Ir–O complex more likely to form in ZnO, the incorporation of additional oxygen atoms will also cause significant structural distortions, making the material appear amorphous in an XRD analysis. Four structures from this section have been selected for further analysis: a zero-interstitial system $Ir^{2+}O_4$, both peroxide solutions, and a groundstate 6-coordinated Ir–O.

5.5.2 Electronic structure

Even without interstitial oxygen atoms Ir produces significant changes in the electronic structure of its host material. Magnetic moment of its 4 oxygen neighbours varies in the range of 0.10–0.12 μ_B, same as for 6-coordinated Ir, regardless of Ir's concentration, see figure 5.3. Magnetic moments on oxygens hint at presence of partially filled electronic levels associated with Ir–O bonds. Figure 5.4 shows calculated density of states (DOS) for $Ir^{2+}O_4$ (a) and a 6-coordinated Ir–O (b).

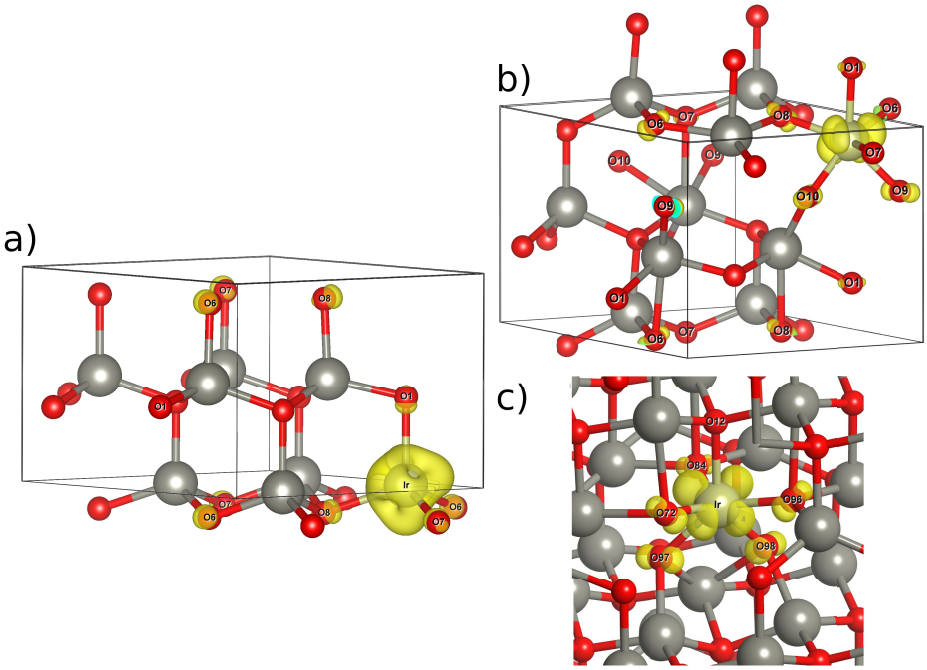

Figure 5.3: Magnetic moments of Ir–O complexes in ZnO. Yellow clouds represent charge density isosurfaces for orbitals with unpaired electrons. Teal clouds are the same surfaces sectioned by the periodic boundary.
a: ZnO + $Ir^{2+}O_4$ [12.5%];
b: ZnO + 6-coordinated Ir–O [12.5%]
c: ZnO + 6-coordinated Ir–O [1.04%], fragment

From figure 5.4 it can be seen that both complexes do have a region extending down to about 0.4 eV below Fermi level, consisting entirely of Ir and O states. Only below this region projections from other atoms appear. This confirms that the top of valence band is exclusively due to Ir–O levels, and from figure 5.3 it is known that they are only partially filled. Bottom of conduction band is also due to Ir–O, and is much closer than that of pure ZnO, narrowing the band gap down to 1.75–1.9 eV.

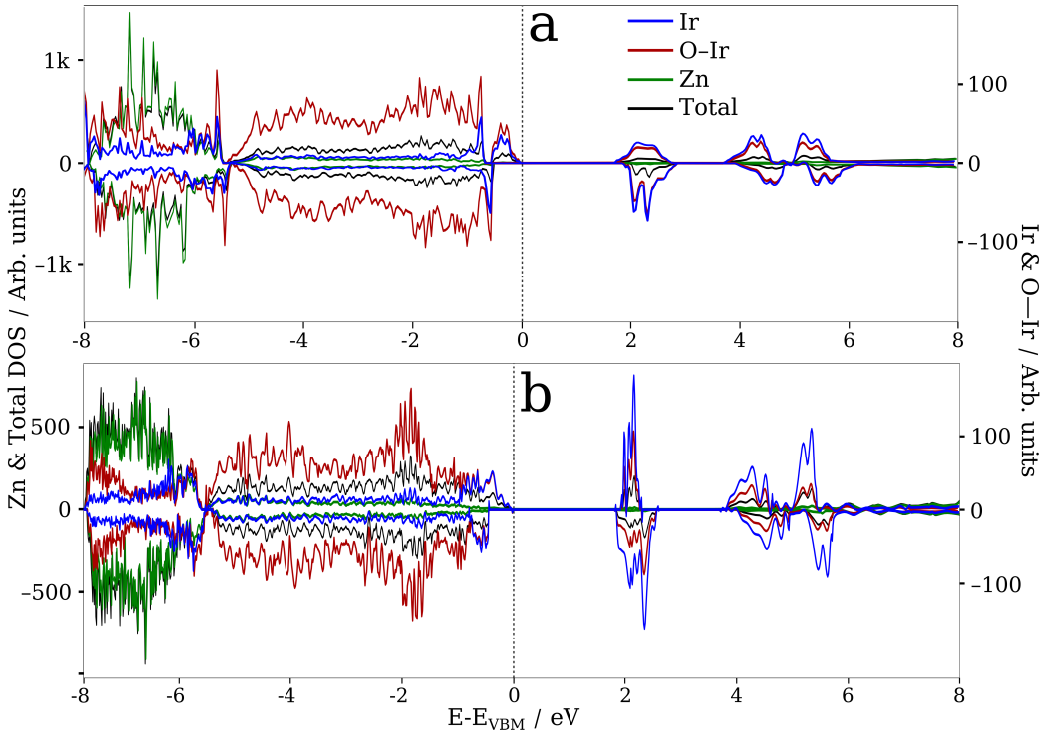

Figure 5.4: DOS of ZnO:Ir. Negative values correspond to spin-down channel.
a: ZnO + $Ir^{2+}O_4$ [12.5%];
b: ZnO + 6-coordinated Ir–O [12.5%]

Following data from tables 5.3, 5.4, and 5.6, these oxidation states were assigned to the selected Ir–O complexes: 3+ for a 4-coordinated solution with peroxide fragment ($Ir^{3+}O_4$); 4+ for 5-coordinated, peroxide-forming complex ($Ir^{4+}O_5$), and 4+ for the 6-coordinated complex ($Ir^{4+}O_6$). These oxidation states are also the most stable positive oxidation states of iridium, and are consistent with the ones found in amorphous IrO_x powders [213].

5.6 Thermoelectric properties

Electronic conductivities and Seebeck coefficients for selected systems are summarised in figure 5.5. Here, an idealised case of $ZnIr_2O_4$, fig.5.5(a), is given as a baseline, representing a 6-coordinated Ir in a system of Zn-O bonds. Zinc-iridium spinel is behaving like a semiconductor. When measured experimentally, at room temperature and in polycrystalline thin film samples [205], its Seebeck coefficient is reported as 53.9 μVK^{-1}, and its conductivity is 2.09×10^2 $\Omega^{-1}m^{-1}$.

Here, taking values at thermally-adjusted Fermi level (see end of section 5.4.3 for details), $ZnIr_2O_4$'s Seebeck coefficient is 92.3 μVK^{-1}, and its conductivity is 1.72×10^2 $\Omega^{-1}m^{-1}$, a good agreement with experimental results. See table 5.7 for the rest of numerical values. The importance of this result is in showing that on its own, 6-coordinated Ir, even when interacting with a system of Zn-O bonds, does not necessarily lead to emergence of p-type conductivity.

Figure 5.5(b) represents $Ir^{2+}O_4$, a 4-coordinated Ir in ZnO without interstitial oxygen atoms. The position of 0 K Fermi level and two regions of conduction mode switching indicate presence of a strong defect level in the electronic structure. According to DOS projections (fig. 5.4(a)), this level

is occupied and consists of Ir–O states. Non-zero spin on oxygen atoms (fig. 5.3(a)) suggests that this level is not fully occupied, and is therefore an acceptor level capable of p-type conductivity.

Results for $Ir^{3+}O_4$ and $Ir^{4+}O_5$ correspond to letters c and d on figure 5.5. These systems represent solutions with a peroxide complex. In comparison to other Ir-O complexes at the same concentration, fig.5.5(b,e), these are characterized with high values of Seebeck coefficient and lower conductivities, hinting that a peroxide complex is not the defect responsible for observed p-type conductivity, in contrast to a hypothesis put forward in [190].

Finally, 6-coordinated complex $Ir^{4+}O_6$ at target concentration [12.5%] and at a low concentration [1.04%], respectively, is shown in fig.5.5(e,f). Once again, it has a partially filled Ir-O level near the top of valence band (figs. 5.4(b) and 5.3(b,c)), its conductivity peaks correspond to positive values of Seebeck coefficient, and bottom of the conductivity well is at $\sim 10^2\ \Omega^{-1}\mathrm{m}^{-1}$, showing all signs of a p-type conductive material. Its low-concentration counterpart, while exhibiting the same qualitative traits, quantitatively behaves much closer to pure ZnO, but still has a potential for p-type conductivity.

Some solutions are very sensitive with respect to computational parameters, most importantly, the density of k-points, discrete step sizes for evaluating TDF (eq. 2.6), and for sampling chemical potential (section 5.3.4). In some cases, combination or mismatch of these parameters produce solutions with numerical uncertainties, – located inside the band gap, – where conductivities reach beyond infinitesimal values set in CRYSTAL code, and Seebeck coefficients are set to zero as a result. Such behaviour is present in $Ir^{3+}O_4$ and $Ir^{4+}O_6$ [1.04%], fig.5.5(c,f), marked by a split in y-axis for conductivity (σ).

In conclusion, it has been shown that Ir in ZnO creates a partially filled electronic acceptor level capable of producing measurable p-type conductivity, and that this Ir-O complex induces strong local structural changes by pulling in interstitial oxygen atoms (assuming oxygen-rich formation conditions) to make energetically favourable 6-coordinated Ir-O complexes.

Results presented in this section are published in ***[A4]*** . The author has conducted all calculations related to parametrisation and validation of the model, has conducted calculations of all systems and all properties, has gathered and interpreted all data, has prepared figures and the first draft of the paper.

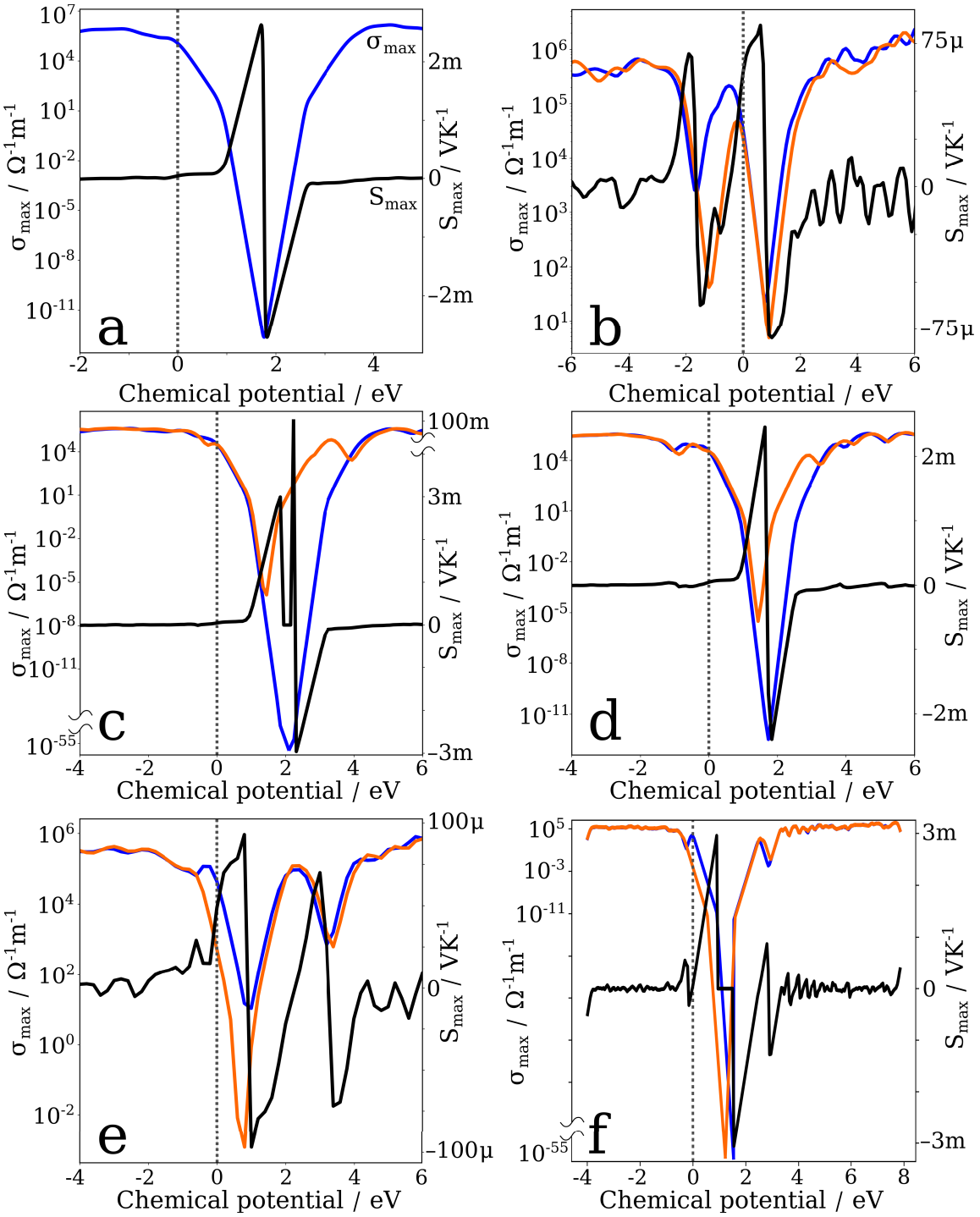

Figure 5.5: Conductivity and Seebeck coefficients of ZnO:Ir at $T = 300$ K. Dashed grey lines mark band edges, with 0 eV = VB top = $E_{Fermi}(0\ K)$
a: pure $ZnIr_2O_4$;
b: ZnO + $Ir^{2+}O_4$ [12.5%];
c: ZnO + $Ir^{3+}O_4$ [12.5%];
d: ZnO + $Ir^{4+}O_5$ [12.5%];
e: ZnO + $Ir^{4+}O_6$ [12.5 %];
f: ZnO + $Ir^{4+}O_6$ [1.04%]

Table 5.7: Calculated thermoelectric properties at temperature-adjusted Fermi levels

Compound	$S, \mu VK^{-1}$	$S_{exp}, \mu VK^{-1}$	$\sigma, \Omega^{-1}m^{-1}$	$\sigma, \Omega^{-1}_{exp}m^{-1}$
ZnO	2510	Non-conductive	6.05×10^{-8}	Non-conductive
$ZnIr_2O_4$	92.3	53.9[i] [205]	1.72×10^{2}	$2.09 \times 10^{2}, 3.39 \times 10^{2}$ [i] [205]
IrO_2	63.9	—	1.32×10^{6}	$1.15–2.90 \times 10^{6}$ [214, 215] $0.68–1.67 \times 10^{6}$ [ii] [216] 2.94×10^{6} [ii] [216]
Ir_2O_3	105	—	8.98×10^{1}	—
$Ir^{2+}O_4$	80.1	6.8 [iv] [190]	2.57×10^{2}	47.6 [iv] [190]
$Ir^{3+}O_4$	88.7		3.20×10^{1}	
$Ir^{4+}O_5$	89.4		4.13×10^{1}	
$Ir^{4+}O_6$ [12.5%]	83.8		1.62×10^{2}	
$Ir^{4+}O_6$ [1.04%]	2335		3.49×10^{-8}	

i. Measured at RT; two values for σ for polycrystalline and epitaxial thin films whereas the Seebeck coefficient was measured for polycrystalline films only; the thin films prepared by PLD between 773 and 973 K.
ii. The values are taken at RT for 100 nm films prepared by PLD and oxidized at 0.05-0.2 mBar and 500 °C
iii. The bulk value measured at RT
iv. Ir concentration is 16.4%

6.SUMMARY AND CONCLUSIONS

This thesis presents the results of density functional theory (DFT) calculations on cerium dioxide(CeO_2) and zinc oxide (ZnO) supercells using corrected generalized gradient approximation (GGA) and hybrid GGA functionals. The results were obtained using massively parallel calculations on high-performance computing systems.

Model formulation and selection of simulation cells is not a trivial task, and it was shown in this work that symmetry analysis of a simulated object can be crucial for obtaining all possible solutions for electron localization and defect distribution in the investigated system. Specifically, the site-symmetry approach, as used in this thesis, was applied to the problem of modelling small polarons in CeO_2, and it was shown that:

- certain supercells and certain atomic positions within these supercells will yield only high-symmetry, highly delocalized solutions;
- larger supercells are not necessarily better for modelling point defects, as they may lack diversity of symmetry orbits;
- localized electronic solutions require lowering or loss of symmetry.

Application of the concentration waves approach (a method of statistical thermodynamics that is also grounded in symmetry analysis) has shown that if a mixture of CeO_2 and TbO_2 were to have a fluorite structure in a temperature where either constituent also has the fluorite structure, an unlimited solubility of Tb in CeO_2 should be observed. This conclusion is good news for high-temperature applications of Tb-doped CeO_2, such as mixed-conductive membranes for oxygen separation, because it asserts that no phase separation should occur at the operating conditions.

The presence of Tb in membranes for oxygen separation has the added benefit of lowering the energy of oxygen vacancy formation even at high partial pressure – a key parameter that enables the transport of oxygen ions across the membrane. It has been demonstrated in this work that in Tb-doped CeO_2 the energy of oxygen vacancy formation is ca. 4 times lower when compared to an undoped system.

It was confirmed that Ir, when embedded in the ZnO matrix, is more likely to form a 6-coordinated complex in comparison to other coordination numbers. It was also shown that, while the formation of peroxide moiety in this system is not impossible, its formation is energetically more demanding in comparison to a peroxide-free system.

The formation of a 6-coordinated Ir-O complex in the ZnO lattice was shown to be a probable cause for the emergence of measurable p-type conductivity in this material. At the same time, peroxide-containing complexes exhibit lower conductivities with higher Seebeck coefficients. This work also shows that well-ordered 6-coordinated Ir on its own cannot be a p-type conductor, even in a system with Zn–O bonds: $ZnIr_2O_4$, a compound with 6-coordinated Ir in a system of Zn–O bonds is shown to exhibit a pure semiconductor-like behaviour. It must be concluded, then, that the emergence of p-type conductivity in Ir-doped ZnO is a combination of lattice distortion and

electronic acceptor levels introduced by Ir with interstitial oxygen atoms.

Main conclusions

1. The site-symmetry approach is a powerful instrument for modelling polaronic properties in crystalline structures.

2. In CeO_2 crystals (and in all materials that have the same crystalline structure) there are supercells with both high- and low-symmetry orbits, as well as supercells in which there are no symmetry orbits corresponding to primitive cell symmetries.

3. The mode of electronic localization can affect the formation energy of a point defect by up to *ca.* 1 eV in a simple binary configuration (such as CeO_2), and by up to *ca.* 3 eV in a more complex configuration when multiple oxidation states are possible (for instance, Tb-doped CeO_2).

4. The mode of electronic localization can be a more important factor affecting the energetics of a solution than the relative defect placement.

5. Ir, when embedded in ZnO under oxygen-rich conditions, creates a 6-coordinated Ir-O complex, which distorts the lattice of ZnO, and produces electronic acceptor levels. At high enough concentrations of Ir these effects compound to such a degree that the resultant structure becomes amorphous, and starts to exhibit a p-type conductivity.

7.MAIN THESES

The results obtained in the course of this work using DFT-based modelling techniques can be used to put forward and provide support for the following propositions:

1. It is possible to list all symmetry-allowed atomic and magnetic configurations of a system using the site-symmetry approach without performing an exhaustive search.
   Published in ***[A1, A3].***

2. In the CeO_2 crystals, both small- and large-radius polarons are able to form, with small polarons having lower energy of formation, and being accompanied by a decrease in local symmetry.
   Published in ***[A1].***

3. Tb ions have unlimited solubility in CeO_2 and may exist as both Tb^{3+} and Tb^{4+}. If an oxygen vacancy is formed alongside a Tb impurity, then Tb^{3+} is the most stable oxidation state.
   Published in ***[A2, A3].***

4. The addition of Tb ions to CeO_2 lowers the formation energy of oxygen vacancies in the material's crystalline structure.
   Published in ***[A3].***

5. In the ZnO crystal Ir ion is likely to create a 6-coordinated complex with the lattice and interstitial oxygen atoms. Such a complex has lower formation energy in comparison to other possible complexes with different coordination numbers.
   Published in ***[A4].***

6. ZnO-embedded Ir complex increases the material's electronic conductivity, lowers its Seebeck coefficient, and can be a cause for measurable p-type conductivity.
   Published in ***[A4].***

AUTHOR'S PUBLICATION LIST

Publications directly related to this thesis

[A1] R. A. Evarestov, D. Gryaznov, M. Arrigoni, E. A. Kotomin, A. Chesnokov, and J. Maier, "Use of site symmetry in supercell models of defective crystals: Polarons in CeO_2", Phys. Chem. Chem. Phys. **19**, 8340–8348 (2017).

[A2] D. Fuks, D. Gryaznov, E. Kotomin, A. Chesnokov, and J. Maier, "Dopant solubility in ceria: Alloy thermodynamics combined with the DFT+U calculations", Solid State Ion **325**, 258–264 (2018).

[A3] A. Chesnokov, D. Gryaznov, and E. Kotomin, "First principles calculations on CeO_2 doped with Tb^{3+} ions", Opt. Mater. **90**, 76–83 (2019).

[A4] A. Chesnokov, D. Gryaznov, N. V. Skorodumova, E. A. Kotomin, A. Zitolo, M. Zubkins, A. Kuzmin, A. Anspoks, and J. Purans, "The local atomic structure and thermoelectric properties of Ir-doped ZnO: Hybrid DFT calculations and XAS experiments", J. Mater. Chem. C **9**, 4948–4960 (2021).

Author's other contributions

[B1] M. F. Hoedl, A. Chesnokov, D. Gryaznov, R. Merkle, E. A. Kotomin, and J. Maier, "Proton migration barriers in $BaFeO_{3-\delta}$ – insights from DFT calculations", J. Mater. Chem. A **11**, 6336–6348 (2023).

[B2] D. Zavickis, G. Zvejnieks, A. Chesnokov, and D. Gryaznov, "Single oxygen vacancy in $BaCoO_3$: Hybrid DFT calculations and local site symmetry approach", Solid State Ion **375**, 115835 (2022).

[B3] D. Bocharov, A. Chesnokov, G. Chikvaidze, J. Gabrusenoks, R. Ignatans, R. Kalendarev, M. Krack, K. Kundzins, A. Kuzmin, N. Mironova-Ulmane, I. Pudza, L. Puust, I. Sildos, E. Vasil'chenko, M. Zubkins, and J. Purans, "A comprehensive study of structure and properties of nanocrystalline zinc peroxide", J. Phys. Chem. Solids, 110318 (2021).

[B4] A. Ivanova, A. Chesnokov, D. Bocharov, and K. S. Exner, "A Universal Approach to Quantify Overpotential-Dependent Selectivity Trends for the Competing Oxygen Evolution and Peroxide Formation Reactions: A Case Study on Graphene Model Electrodes", J. Phys. Chem. C **125**, 10413–10421 (2021).

[B5] O. Lisovski, A. Chesnokov, S. Piskunov, D. Bocharov, Y. F. Zhukovskii, M. Wessel, and E. Spohr, "Ab initio calculations of doped TiO_2 anatase (101) nanotubes for photocatalytical water splitting applications", Materials Science in Semiconductor Processing **42**, 138–141 (2016).

PARTICIPATION IN CONFERENCES

International conferences

1. 29.05.–02.06.2023, Spring meeting of the European Materials Research Society (Strasbourg, France),
   oral presentation "*Atomistic insight into proton migration barriers in* $BaFeO_{3-\delta}$" (A. Chesnokov, M. F. Hoedl, D. Gryaznov, R. Merkle, E. A. Kotomin, J. Maier)

2. 04.07.–06.07.2022, The joint Functional Materials and Nanotechnologies (FM&NT) and Nanotechnology and Innovation in the Baltic Sea region (NIBS) conference, (Riga, Latvia),
   oral presentation "*A first-principles study of point defects and electronic conductivity in ZnO*" (A. Chesnokov, D. Gryaznov, D. Bocharov, A. Kuzmin, J. Purans)

3. 31.05.–03.06.2021, Spring meeting of the European Materials Research Society (Online),
   oral presentation "*Thermoelectric properties of Ir-doped ZnO from hybrid DFT calculations*" (A. Chesnokov, D. Gryaznov, A. Kuzmin, J. Purans, E. A. Kotomin, N. V. Skorodumova)

4. 23.11.–26.11.2020, 11th International Scientific Conference "Functional Materials and Nanotechnologies" (Online),
   oral presentation "*Role of interstitial oxygens in Ir-doped ZnO*" (A. Chesnokov, D. Gryaznov, J. Purans, E. A. Kotomin, N. V. Skorodumova)

5. 16.09.–20.09.2019, Fall meeting of the European Materials Research Society (Warsaw, Poland),
   oral presentation "*Hybrid density functional calculations of Ir doped ZnO*" (A. Chesnokov, D. Gryaznov, J. Purans, E. A. Kotomin, N. V. Skorodumova);
   poster presentation "*Defects in* CeO_2*: DFT and site symmetry approach*" (A. Chesnokov, D. Gryaznov, E. A. Kotomin)

6. 30.05.–01.06.2019, 118th General Assembly of the German Bunsen Society for Physical Chemistry, Bunsentagung 2019 (Jena, Germany),
   poster presentation "*Calculating* Tb^{3+}*-doped* CeO_2 *from first principles*" (A. Chesnokov, D. Gryaznov, E. A. Kotomin)

7. 24.04.–27.04.2017, 11th International Scientific Conference "Functional Materials and Nanotechnologies" (Tartu, Estonia),
   poster presentation "*First principles calculations of defective* CeO_2*: use of site symmetry in a supercell model*" (A. Chesnokov, D. Gryaznov, R.A. Evarestov, E.A. Kotomin)

Local conferences

1. 28.02.–02.03.2023, 39th annual ISSP UL scientific conference (Riga),
   oral presentation "*Atomistic insight into proton migration barriers in* $BaFeO_{3-\delta}$" (A. Chesnokov, M. F. Hoedl, D. Gryaznov, R. Merkle, E. A. Kotomin, J. Maier)

2. 22.02.–24.02.2022, 38th annual ISSP UL scientific conference (online),

oral presentation "*First-principles description of ZnO_2: a comparative DFT study*" (A. Chesnokov, D. Gryaznov, D. Bocharov, J. Purans)

3. 23.02.–25.02.2021, 37th annual ISSP UL scientific conference (online),
   oral presentation "*Local atomic structure of Ir-doped ZnO: a comparison between experimental results and hybrid DFT calculations*" (A. Chesnokov, D. Gryaznov, J. Purans, A. Kuzmin, E. A. Kotomin, N. V. Skorodumova)

4. 11.02.–13.02.2020, 36th annual ISSP UL scientific conference (Riga),
   oral presentation "*ZnO-embedded IrO_2: a first-principles approach to electronic defects*" (A. Chesnokov, D. Gryaznov, J. Purans, A. Kuzmin, E. A. Kotomin, N. V. Skorodumova)

5. 29.03.2019, – The 77th conference of the University of Latvia (Riga),
   oral presentation "*First principles calculations on CeO_2 doped with Tb^{3+} ions*" (A. Chesnokov, D. Gryaznov, E. A. Kotomin)

6. 20.02.–22.02.2019, – 35th annual ISSP UL scientific conference (Riga),
   poster presentation "*First principles calculations on CeO_2 doped with Tb^{3+} ions*" (A. Chesnokov, D. Gryaznov, E. A. Kotomin);
   poster presentation "*Exploring structure of defective Zinc Oxide*" (A. Chesnokov, D. Gryaznov, N. V. Skorodumova)

7. 06.04.2018, The 76th conference of the University of Latvia (Riga),
   oral presentation "*Electron localization effects in Tb-doped CeO_2*" (A. Chesnokov, D. Gryaznov, E.A. Kotomin)

8. 20.02.–22.02.2018, 34th annual ISSP UL scientific conference (Riga),
   oral presentation "*Electron localization effects in Tb-doped CeO_2*" (A. Chesnokov, D. Gryaznov, E.A. Kotomin)

9. 22.02.–24.02.2017, 33rd annual ISSP UL scientific conference (Riga),
   poster presentation "*Use of site symmetry in supercell model of defective CeO_2*" (A. Chesnokov, D. Gryaznov, R.A. Evarestov, E.A. Kotomin)

10. 17.02.–19.02.2016, 32nd annual ISSP UL scientific conference (Riga),
    oral presentation "*Calculation of pure and doped cerium dioxide properties in bulk phase*" (A. Chesnokov, D. Gryaznov, M. Arrigoni, R. A. Evarestov)

PARTICIPATION IN INTERNATIONAL SCHOOLS

During the preparation of this Thesis, its Author has participated in the following international schools:

2021. Virtual school on electronic excitations in solids and nanostructures using the Yambo code, *Online*

2019. Advanced Electronic Structure Methods in Condensed Matter Physics, *Lausanne, Switzerland*, poster presentation "*Use of site symmetry in supercell model of defective* CeO_2", (A. Chesnokov, D. Gryaznov, R.A. Evarestov, E.A. Kotomin)

2018. PDC-PRACE workshop "HPC Tools for the Modern Era", *Stockholm, Sweden*

REFERENCES

[1]T. W. Ebbesen, H. J. Lezec, H. Hiura, J. W. Bennett, H. F. Ghaemi, and T. Thio, "Electrical conductivity of individual carbon nanotubes", Nature **382**, 54–56 (1996).

[2]C. Kittel, *Introduction to solid state physics*, 8th ed (Wiley, Hoboken, NJ, 2005), 680 pp.

[3]M. I. Aroyo, ed., *International Tables for Crystallography: Space-group symmetry*, 2nd ed., Vol. A (International Union of Crystallography, Chester, England, Dec. 31, 2016).

[4]S. F. A. Kettle and L. J. Norrby, "Really, your lattices are all primitive, Mr. Bravais!", J. Chem. Educ. **70**, 959 (1993).

[5]H. Wondratschek and U. Müller, eds., *International Tables for Crystallography: Symmetry relations between space groups*, 2nd ed., Vol. A1 (International Union of Crystallography, Chester, England, Dec. 15, 2011).

[6]A. M. Dobrotvorskii and E. A. Evarestov, "The Quasi-Molecular Large Unit Cell Model in the Theory of Deep Levels in Imperfect Crystals: Point Defects in Graphitic Boron Nitride", Phys. Stat. Sol. (b) **66**, 83–91 (1974).

[7]A. H. Harker and F. P. Larkins, "A large unit cell semiempirical molecular orbital approach to the properties of solids. I. General theory", J. Phys. C: Solid State Phys. **12**, 2487–2495 (1979).

[8]R. A. Evarestov and V. P. Smirnov, "Symmetrical transformation of basic translation vectors in the supercell model of imperfect crystals and in the theory of special points of the Brillouin zone", J. Phys. Condens. Matter **9**, 3023–3031 (1997).

[9]H. Wondratschek, "Splitting of Wyckoff positions (orbits)", Mineral Petrol. **48**, 87–96 (1993).

[10]H. Wondratschek, U. Mülller, M. I. Aroyo, and I. Sens, "Splitting of Wyckoff positions (orbits). II. Group-subgroup chains of index 6.1", Z. Kristallogr. Cryst. Mater. **210**, 567–573 (1995).

[11]R. Dovesi, V. R. Saunders, C. Roetti, R. Orlando, C. M. Zicovich-Wilson, F. Pascale, B. Civalleri, K. Doll, N. M. Harrison, I. J. Bush, P. D'Arco, M. Llunell, M. Causà, Y. Noël, L. Maschio, A. Erba, M. Rerat, and S. Casassa, *CRYSTAL17 User's Manual* (University of Torino, Torino, 2017).

[12]W. Kohn and L. J. Sham, "Self-Consistent Equations Including Exchange and Correlation Effects", Phys. Rev. **140**, A1133–A1138 (1965).

[13]J. P. Allen and G. W. Watson, "Occupation matrix control of d- and f-electron localisations using DFT + U", Phys. Chem. Chem. Phys. **16**, 21016–21031 (2014).

[14]F. Herman, J. P. Van Dyke, and I. B. Ortenburger, "Improved Statistical Exchange Approximation for Inhomogeneous Many-Electron Systems", Phys. Rev. Lett. **22**, 807–811 (1969).

[15]A. D. Becke, "Density-functional exchange-energy approximation with correct asymptotic behavior", Phys. Rev. A **38**, 3098–3100 (1988).

[16]J. P. Perdew and Y. Wang, "Accurate and simple analytic representation of the electron-gas correlation energy", Phys. Rev. B **45**, 13244–13249 (1992).

[17]J. P. Perdew, K. Burke, and M. Ernzerhof, "Generalized Gradient Approximation Made Simple", Phys. Rev. Lett. **77**, 3865–3868 (1996).

[18]E. R. Ylvisaker, W. E. Pickett, and K. Koepernik, "Anisotropy and magnetism in the LSDA + U method", Phys. Rev. B **79**, 035103 (2009).

[19]B. Himmetoglu, A. Floris, S. de Gironcoli, and M. Cococcioni, "Hubbard-corrected DFT energy functionals: The LDA+U description of correlated systems", Int. J. Quantum Chem. **114**, 14–49 (2014).

[20]S. L. Dudarev, D. N. Manh, and A. P. Sutton, "Effect of Mott-Hubbard correlations on the electronic structure and structural stability of uranium dioxide", Phil. Mag. B. **75**, 613–628 (1997).

[21]M. Cococcioni and S. de Gironcoli, "A linear response approach to the calculation of the effective interaction parameters in the LDA+U method", Phys Rev B **71**, 035105 (2005).

[22]A. D. Becke, "A new mixing of Hartree–Fock and local density-functional theories", J Chem Phys **98**, 1372–1377 (1993).

[23]J. P. Perdew, M. Ernzerhof, and K. Burke, "Rationale for mixing exact exchange with density functional approximations", J Chem Phys **105**, 9982–9985 (1996).

[24]C. Adamo and V. Barone, "Toward reliable density functional methods without adjustable parameters: The PBE0 model", J Chem Phys **110**, 6158–6170 (1999).

[25]A. D. Becke, "Density-functional thermochemistry. III. The role of exact exchange", J Chem Phys **98**, 5648–5652 (1993).

[26]D. I. Bilc, R. Orlando, R. Shaltaf, G.-M. Rignanese, J. Íñiguez, and P. Ghosez, "Hybrid exchange-correlation functional for accurate prediction of the electronic and structural properties of ferroelectric oxides", Phys. Rev. B **77**, 165107 (2008).

[27]R. Demichelis, B. Civalleri, M. Ferrabone, and R. Dovesi, "On the performance of eleven DFT functionals in the description of the vibrational properties of aluminosilicates: Performance of Eleven DFT Functionals", Int J Quantum Chem **110**, 406–415 (2010).

[28]J. Heyd, G. E. Scuseria, and M. Ernzerhof, "Hybrid functionals based on a screened Coulomb potential", J Chem Phys **118**, 8207–8215 (2003).

[29]A. V. Krukau, O. A. Vydrov, A. F. Izmaylov, and G. E. Scuseria, "Influence of the exchange screening parameter on the performance of screened hybrid functionals", J Chem Phys **125**, 224106 (2006).

[30]M. P. Teter, M. C. Payne, and D. C. Allan, "Solution of Schrödinger's equation for large systems", Phys. Rev. B **40**, 12255–12263 (1989).

[31]D. M. Bylander, L. Kleinman, and S. Lee, "Self-consistent calculations of the energy bands and bonding properties of $B_{12}C_3$", Phys. Rev. B **42**, 1394–1403 (1990).

[32]G. H. F. Diercksen and S. Wilson, eds., *Methods in Computational Molecular Physics*, 1st ed., Vol. 113, NATO Advanced Study Institute Series C (Plenum, New York, 1983), VII, 367.

[33]D. Wood and A. Zunger, "A new method for diagonalising large matrices", J. Phys. A **18**, 1343–1359 (1985).

[34]P. Pulay, "Convergence acceleration of iterative sequences. the case of scf iteration", Chem. Phys. Lett. **73**, 393–398 (1980).

[35]D. D. Johnson, "Modified Broyden's method for accelerating convergence in self-consistent calculations", Phys. Rev. B **38**, 12807–12813 (1988).

[36]F. Bloch, "Über die Quantenmechanik der Elektronen in Kristallgittern", Z. Physik **52**, 555–600 (1929).

[37]D. R. Hamann, M. Schlüter, and C. Chiang, "Norm-Conserving Pseudopotentials", Phys. Rev. Lett. **43**, 1494–1497 (1979).

[38]D. Vanderbilt, "Soft self-consistent pseudopotentials in a generalized eigenvalue formalism", Phys. Rev. B **41**, 7892–7895 (1990).

[39]P. E. Blöchl, "Projector augmented-wave method", Phys. Rev. B **50**, 17953–17979 (1994).

[40]G. Kresse and D. Joubert, "From ultrasoft pseudopotentials to the projector augmented-wave method", Phys. Rev. B **59**, 1758–1775 (1999).

[41]E. Besalú and R. Carbó-Dorca, "The general Gaussian product theorem", J Math Chem **49**, 1769–1784 (2011).

[42]C. M. Zicovich-Wilson and R. Dovesi, "On the use of symmetry-adapted crystalline orbitals in SCF-LCAO periodic calculations. I. The construction of the symmetrized orbitals", Int. J. Quant. Chem. **67**, 299–309 (1998).

[43]C. M. Zicovich-Wilson and R. Dovesi, "On the use of symmetry-adapted crystalline orbitals in SCF-LCAO periodic calculations. II. Implementation of the self-consistent-field scheme and examples", Int. J. Quant. Chem. **67**, 311–320 (1998).

[44]R. Dovesi, C. Ermondi, E. Ferrero, C. Pisani, and C. Roetti, "Hartree-Fock study of lithium hydride with the use of a polarizable basis set", Phys. Rev. B **29**, 3591–3600 (1984).

[45]M. Lundstrom, *Fundamentals of carrier transport*, 2nd ed (Cambridge University Press, Cambridge, U.K. ; New York, 2000), 418 pp.

[46]G. Sansone, A. Ferretti, and L. Maschio, "*Ab Initio* electronic transport and thermoelectric properties of solids from full and range-separated hybrid functionals", J Chem Phys **147**, 114101 (2017).

[47]T. Zacherle, A. Schriever, R. A. De Souza, and M. Martin, "*Ab Initio* analysis of the defect structure of ceria", Phys. Rev. B **87**, 134104 (2013).

[48]C. W. M. Castleton, A. L. Lee, J. Kullgren, and K. Hermansson, "Description of polarons in ceria using Density Functional Theory", J Phys Conf Ser **526**, 012002 (2014).

[49]J. J. Plata, A. M. Márquez, and J. F. Sanz, "Electron Mobility via Polaron Hopping in Bulk Ceria: A First-Principles Study", J. Phys. Chem. C **117**, 14502–14509 (2013).

[50]P. R. L. Keating, D. O. Scanlon, B. J. Morgan, N. M. Galea, and G. W. Watson, "Analysis of Intrinsic Defects in CeO_2 Using a Koopmans-Like GGA+U Approach", J. Phys. Chem. C **116**, 2443–2452 (2012).

[51]M. V. Ganduglia-Pirovano, A. Hofmann, and J. Sauer, "Oxygen vacancies in transition metal and rare earth oxides: Current state of understanding and remaining challenges", Surf Sci Rep **62**, 219–270 (2007).

[52]J. M. Serra, V. B. Vert, M. Betz, V. A. C. Haanappel, W. A. Meulenberg, and F. Tietz, "Screening of A-Substitution in the System $A_{0.68}Sr_{0.3}Fe_{0.8}Co_{0.2}O_{3-\delta}$ for SOFC Cathodes", J. Electrochem. Soc. **155**, B207–B214 (2008).

[53]J. Sunarso, S. Baumann, J. Serra, W. Meulenberg, S. Liu, Y. Lin, and J. Diniz da Costa, "Mixed Ionic–Electronic conducting (MIEC) ceramic-based membranes for oxygen separation", J. Memb. Sci. **320**, 13–41 (2008).

[54]D. R. Ou, T. Mori, F. Ye, J. Zou, G. Auchterlonie, and J. Drennan, "Oxygen-vacancy ordering in lanthanide-doped ceria: Dopant-type dependence and structure model", Phys. Rev. B **77**, 024108 (2008).

[55]P. Jasinski, T. Suzuki, and H. U. Anderson, "Nanocrystalline undoped ceria oxygen sensor", Sens. Actuators B Chem. **95**, 73–77 (2003).

[56]N. Yavo, O. Yeheskel, E. Wachtel, D. Ehre, A. I. Frenkel, and I. Lubomirsky, "Relaxation and saturation of electrostriction in 10 mol% Gd-doped ceria ceramics", Acta Mater. **144**, 411–418 (2018).

[57]R. Korobko, A. Patlolla, A. Kossoy, E. Wachtel, H. L. Tuller, A. I. Frenkel, and I. Lubomirsky, "Giant Electrostriction in Gd-Doped Ceria", Adv Mater **24**, 5857–5861 (2012).

[58]W. C. Chueh, C. Falter, M. Abbott, D. Scipio, P. Furler, S. M. Haile, and A. Steinfeld, "High-Flux Solar-Driven Thermochemical Dissociation of CO_2 and H_2O Using Nonstoichiometric Ceria", Science **330**, 1797 (2010).

[59]M. P. Lobera, J. M. Serra, S. P. Foghmoes, M. Søgaard, and A. Kaiser, "On the use of supported ceria membranes for oxyfuel process/syngas production", J. Memb. Sci. **385–386**, 154–161 (2011).

[60]Luo Huixia, Efimov Konstantin, Jiang Heqing, Feldhoff Armin, Wang Haihui, and Caro Jürgen, "CO_2-Stable and Cobalt-Free Dual-Phase Membrane for Oxygen Separation", Angew. Chem. Int. Ed. **50**, 759–763 (2010).

[61]I. Naik and T. Tien, "Small-polaron mobility in nonstoichiometric cerium dioxide", J Phys Chem Solids **39**, 311–315 (1978).

[62]S. Reis, E. Souza, and E. Muccillo, "Solid solution formation, densification and ionic conductivity of Gd- and Sm-doped ceria", Solid State Ion **192**, 172–175 (2011).

[63]H. Wang, A. Chroneos, and U. Schwingenschlögl, "Impact of doping on the ionic conductivity of ceria: A comprehensive model", J Chem Phys **138**, 224705 (2013).

[64]H. Yahiro, K. Eguchi, and H. Arai, "Electrical properties and reducibilities of ceria-rare earth oxide systems and their application to solid oxide fuel cell", Solid State Ion **36**, 71–75 (1989).

[65]S. R. Bishop, T. S. Stefanik, and H. L. Tuller, "Electrical conductivity and defect equilibria of $Pr_{0.1}Ce_{0.9}O_{2-\delta}$", Phys. Chem. Chem. Phys. **13**, 10165–10173 (2011).

[66]M. Alaydrus, M. Sakaue, S. M. Aspera, T. D. K. Wungu, T. P. T. Linh, H. Kasai, T. Ishihara, and T. Mohri, "A first-principles study on defect association and oxygen ion migration of Sm^{3+} and Gd^{3+} co-doped ceria", J Phys Condens Matter **25**, 225401 (2013).

[67]F. Giannici, G. Gregori, C. Aliotta, A. Longo, J. Maier, and A. Martorana, "Structure and Oxide Ion Conductivity: Local Order, Defect Interactions and Grain Boundary Effects in Acceptor-Doped Ceria", Chem. Mater. **26**, 5994–6006 (2014).

[68]V. Venckutė, S. Kazlauskas, E. Kazakevičius, A. Kežionis, R. Korobko, and T. Šalkus, "High frequency impedance spectroscopy study on Gd-doped CeO_2 thin films", Ionics **24**, 1153–1159 (2018).

[69]P. A. Žguns, A. V. Ruban, and N. V. Skorodumova, "Ordering and phase separation in Gd-doped ceria: A combined DFT, cluster expansion and Monte Carlo study", Phys. Chem. Chem. Phys. **19**, 26606–26620 (2017).

[70]H. J. Park and G. M. Choi, "Oxygen permeability of gadolinium-doped ceria at high temperature", J. Eur. Ceram. Soc. **24**, 1313–1317 (2004).

[71]P. Novák, T. Kozák, P. Šutta, M. Kolega, and O. Bláhová, "Influence of Oxygen on the Resistivity of Co-Sputtered Transparent AZO Films", Phys Status Solidi A Appl Mater Sci **215**, 1700951 (2018).

[72]P. Novák, J. Očenášek, T. Kozák, and J. Savková, "Identification of electrical properties in individual thickness layers in aluminium-doped zinc oxide films sputtered at 100 °C", Thin Solid Films **660**, 471–476 (2018).

[73]J. Rezek, P. Novák, J. Houška, A. Pajdarová, and T. Kozák, "High-rate reactive high-power impulse magnetron sputtering of transparent conductive Al-doped ZnO thin films prepared at ambient temperature", Thin Solid Films **679**, 35–41 (2019).

[74]A. Janotti and C. G. Van de Walle, "Fundamentals of zinc oxide as a semiconductor", Rep Prog Phys **72**, 126501 (2009).

[75]W. Jeong, S. Kim, and G. Park, "Preparation and characteristic of ZnO thin film with high and low resistivity for an application of solar cell", Thin Solid Films **506–507**, 180–183 (2006).

[76]J. Kennedy, P. Murmu, J. Leveneur, A. Markwitz, and J. Futter, "Controlling preferred orientation and electrical conductivity of zinc oxide thin films by post growth annealing treatment", Appl Surf Sci **367**, 52–58 (2016).

[77]V. Sahu, P. Misra, R. Ajimsha, A. K. Das, and B. Singh, "Effect of growth temperature on diode parameters of n-ZnO/p-Si heterojuction diodes grown by atomic layer deposition", Mater Sci Semicond Process **54**, 1–5 (2016).

[78]M. Ahmed, F. Taghizadeh, F. Auret, W. Meyer, and J. Nel, "The effect of alpha particle irradiation on electrical properties and defects of ZnO thin films prepared by sol-gel spin coating", Mater Sci Semicond Process **101**, 82–86 (2019).

[79]D. C. Look, B. Claflin, Y. I. Alivov, and S. J. Park, "The future of ZnO light emitters", Phys Status Solidi A **201**, 2203–2212 (2004).

[80]Ü. Özgür, Y. I. Alivov, C. Liu, A. Teke, M. A. Reshchikov, S. Doğan, V. Avrutin, S.-J. Cho, and H. Morkoç, "A comprehensive review of ZnO materials and devices", J Appl Phys **98**, 041301 (2005).

[81]Z. R. Tian, J. A. Voigt, J. Liu, B. Mckenzie, M. J. Mcdermott, M. A. Rodriguez, H. Konishi, and H. Xu, "Complex and oriented ZnO nanostructures", Nature Mater **2**, 821–826 (2003).

[82]L. K. Adams, D. Y. Lyon, and P. J. Alvarez, "Comparative eco-toxicity of nanoscale TiO_2, SiO_2, and ZnO water suspensions", Water Res **40**, 3527–3532 (2006).

[83]T. S. Bjørheim and E. Kotomin, "Ab Initio Thermodynamics of Oxygen Vacancies and Zinc Interstitials in ZnO", J. Phys. Chem. Lett. **5**, 4238–4242 (2014).

[84]S. Lany and A. Zunger, "Many-body GW calculation of the oxygen vacancy in ZnO", Phys Rev B **81**, 113201 (2010).

[85]H. Li, L. K. Schirra, J. Shim, H. Cheun, B. Kippelen, O. L. A. Monti, and J.-L. Bredas, "Zinc Oxide as a Model Transparent Conducting Oxide: A Theoretical and Experimental Study of the Impact of Hydroxylation, Vacancies, Interstitials, and Extrinsic Doping on the Electronic Properties of the Polar ZnO (0002) Surface", Chem Mater **24**, 3044–3055 (2012).

[86]J. Wang, R. Chen, L. Xiang, and S. Komarneni, "Synthesis, properties and applications of ZnO nanomaterials with oxygen vacancies: A review", Ceram. Int. **44**, 7357–7377 (2018).

[87]K. H. Kim, K. C. Park, and D. Y. Ma, "Structural, electrical and optical properties of aluminum doped zinc oxide films prepared by radio frequency magnetron sputtering", J Appl Phys **81**, 7764–7772 (1997).

[88]V. Assunção, E. Fortunato, A. Marques, H. Águas, I. Ferreira, M. Costa, and R. Martins, "Influence of the deposition pressure on the properties of transparent and conductive ZnO:Ga thin-film produced by r.f. sputtering at room temperature", Thin Solid Films **427**, 401–405 (2003).

[89]D. Caffrey, A. Zhussupbekova, R. Vijayaraghavan, A. Ainabayev, A. Kaisha, G. Sugurbekova, I. Shvets, and K. Fleischer, "Crystallographic characterisation of ultra-thin, or amorphous transparent conducting oxides-the case for Raman spectroscopy", Mater. **13**, 267 (2020).

[90]M. Joseph, H. Tabata, and T. Kawai, "P-Type Electrical Conduction in ZnO Thin Films by Ga and N Codoping", Jpn. J. Appl. Phys. **38**, L1205–L1207 (1999).

[91]S. Chu, J. H. Lim, L. J. Mandalapu, Z. Yang, L. Li, and J. L. Liu, "Sb-doped p-ZnO/Ga-doped n-ZnO homojunction ultraviolet light emitting diodes", Appl. Phys. Lett. **92**, 152103 (2008).

[92]D. Mora-Fonz and A. L. Shluger, "Making amorphous ZnO: Theoretical predictions of its structure and stability", Phys Rev B **99**, 014202 (2019).

[93]A. Djurišić, A. Ng, and X. Chen, "ZnO nanostructures for optoelectronics: Material properties and device applications", Prog Quant Electron **34**, 191–259 (2010).

[94]D. Look, "Recent advances in ZnO materials and devices", Mater. Sci. Eng. B **80**, 383–387 (2001).

[95]S. Limpijumnong, S. B. Zhang, S.-H. Wei, and C. H. Park, "Doping by Large-Size-Mismatched Impurities: The Microscopic Origin of Arsenic- or Antimony-Doped p -Type Zinc Oxide", Phys. Rev. Lett. **92**, 155504 (2004).

[96]F. Tuomisto, V. Ranki, K. Saarinen, and D. C. Look, "Evidence of the Zn Vacancy Acting as the Dominant Acceptor in *n*-Type ZnO", Phys. Rev. Lett. **91**, 205502 (2003).

[97]A. Janotti and C. G. Van de Walle, "Native point defects in ZnO", Phys. Rev. B **76**, 165202 (2007).

[98]S. Lany and A. Zunger, "Dopability, intrinsic conductivity, and nonstoichiometry of transparent conducting oxides", Phys Rev Lett **98**, 045501 (2007).

[99]J. Fan, K. Sreekanth, Z. Xie, S. Chang, and K. Rao, "P-Type ZnO materials: Theory, growth, properties and devices", Prog Mater Sci **58**, 874–985 (2013).

[100]L. Pan, S. Wang, W. Mi, J. Song, J.-J. Zou, L. Wang, and X. Zhang, "Undoped ZnO abundant with metal vacancies", Nano Energy **9**, 71–79 (2014).

[101]A. Renaud, L. Cario, X. Rocquefelte, P. Deniard, E. Gautron, E. Faulques, T. Das, F. Cheviré, F. Tessier, and S. Jobic, "Unravelling the origin of the giant Zn deficiency in wurtzite type ZnO nanoparticles", Sci Rep **5**, 12914 (2015).

[102]J. L. Lyons and A. Janotti, "Why nitrogen cannot lead to P-type conductivity in ZnO", Appl. Phys. Lett. **95**, 252105 (2009).

[103]S. Zhang, S.-H. Wei, and A. Zunger, "A phenomenological model for systematization and prediction of doping limits in II-VI and I-III-VI2 compounds", J Appl Phys **83**, 3192–3196 (1998).

[104]M. C. Tarun, M. Z. Iqbal, and M. D. McCluskey, "Nitrogen is a deep acceptor in ZnO", AIP Advances **1**, 022105 (2011).

[105]B. Chavillon, L. Cario, A. Renaud, F. Tessier, F. Cheviré, M. Boujtita, Y. Pellegrin, E. Blart, A. Smeigh, L. Hammarström, F. Odobel, and S. Jobic, "P-Type Nitrogen-Doped ZnO Nanoparticles Stable under Ambient Conditions", J. Am. Chem. Soc. **134**, 464–470 (2012).

[106]A. de Jamblinne de Meux, G. Pourtois, J. Genoe, and P. Heremans, "Effects of hole self-trapping by polarons on transport and negative bias illumination stress in amorphous-IGZO", J Appl Phys **123**, 161513 (2018).

[107]A. Hino, S. Kosaka, S. Morita, S. Yasuno, T. Kishi, K. Hayashi, and T. Kugimiya, "Direct Evaluation of Electron Traps in Amorphous In-Ga-Zn-O Thin Film Transistors Using Transient Capacitance Technique", ECS Solid State Lett **1**, Q51–Q53 (2012).

[108]S. Jeong, Y.-G. Ha, J. Moon, A. Facchetti, and T. J. Marks, "Role of Gallium Doping in Dramatically Lowering Amorphous-Oxide Processing Temperatures for Solution-Derived Indium Zinc Oxide Thin-Film Transistors", Adv Mater **22**, 1346–1350 (2010).

[109]H.-H. Nahm and Y.-S. Kim, "Undercoordinated indium as an intrinsic electron-trap center in amorphous $InGaZnO_4$", NPG Asia Mater **6**, e143–e143 (2014).

[110]A. de Jamblinne de Meux, G. Pourtois, J. Genoe, and P. Heremans, "Comparison of the electronic structure of amorphous versus crystalline indium gallium zinc oxide semiconductor: Structure, tail states and strain effects", J Phys D Appl Phys **48**, 435104 (2015).

[111]C. A. Hoel, S. Xie, C. Benmore, C. D. Malliakas, J.-F. Gaillard, and K. R. Poeppelmeier, "Evidence for Tetrahedral Zinc in Amorphous $In_{2-2x}Zn_xSn_xO_3$ (*a*-ZITO)", Z. anorg. allg. Chem **637**, 885–894 (2011).

[112]T. Kamiya, S. Narushima, H. Mizoguchi, K. Shimizu, K. Ueda, H. Ohta, M. Hirano, and H. Hosono, "Electrical Properties and Structure of P-Type Amorphous Oxide Semiconductor $\mathbf{x}ZnO{\cdot}Rh_2O_3$", Adv. Funct. Mater. **15**, 968–974 (2005).

[113]C. P. Liu, K. O. Egbo, C. Y. Ho, Y. Wang, C. K. Xu, and K. M. Yu, "Wide-Gap $Zn_{1-x}Ni_x$ O Alloy: A Transparent *p*-Type Oxide", Phys. Rev. Applied **13**, 024049 (2020).

[114]M. J. Wahila, Z. W. Lebens-Higgins, A. J. Jackson, D. O. Scanlon, T.-L. Lee, J. Zhang, K. H. L. Zhang, and L. F. J. Piper, "Band edge evolution of transparent $ZnM_2{}^{III}O_4$ (M^{III} = Co , Rh, Ir) spinels", Phys Rev B **100**, 085126 (2019).

[115]E. L. Mayes, J. G. Partridge, M. R. Field, D. G. McCulloch, S. M. Durbin, H.-S. Kim, and M. W. Allen, "The interface structure of high performance ZnO Schottky diodes", Physica B Condens **407**, 2867–2870 (2012).

[116]D. Muñoz Ramo and P. D. Bristowe, "Impact of amorphization on the electronic properties of Zn–Ir–O systems", J Phys Condens Matter **28**, 345502 (2016).

[117]D. Muñoz Ramo, A. Chroneos, M. Rushton, and P. Bristowe, "Effect of trivalent dopants on local coordination and electronic structure in crystalline and amorphous ZnO", Thin Solid Films **555**, 117–121 (2014).

[118]D. Schmeißer, J. Haeberle, P. Barquinha, D. Gaspar, L. Pereira, R. Martins, and E. Fortunato, "Electronic structure of amorphous ZnO films: Electronic structure of amorphous ZnO films", Phys Status Solidi C **11**, 1476–1480 (2014).

[119]H. Tuller and A. Nowick, "Small polaron electron transport in reduced CeO_2 single crystals", J. Phys. Chem. Solids **38**, 859–867 (1977).

[120]Y. Natanzon, A. Azulay, and Y. Amouyal, "Evaluation of Polaron Transport in Solids from First-principles", Isr. J. Chem. **60**, 768–786 (2020).

[121]D. Vollhardt, "Dynamical Mean-Field Approach for Strongly Correlated Materials", in *The LDA+DMFT approach to strongly correlated materials: lecture notes of the Autumn School 2011 Hands-on LDA+DMFT: at Forschungszentrum Jülich, 4-7 October 2011*, edited by E. Pavarini, E. Koch, A. I. Lichtenstein, and D. Vollhardt, Schriften Des Forschungszentrums Jülich. Reihe Modeling and Simulation (Forschungszentrum Jülich, Zentralbibliothek, Verlag, Jülich, 2011), pp. 1.1–1.29.

[122]L. H. Tjeng, "Challenges from Experiment", in *The LDA+DMFT approach to strongly correlated materials: lecture notes of the Autumn School 2011 Hands-on LDA+DMFT: at Forschungszentrum Jülich, 4-7 October 2011*, edited by E. Pavarini, E. Koch, A. I. Lichtenstein, and D. Vollhardt, Schriften Des Forschungszentrums Jülich. Reihe Modeling and Simulation (Forschungszentrum Jülich, Zentralbibliothek, Verlag, Jülich, 2011), pp. 14.1–14.21.

[123]T. Schäfer, N. Daelman, and N. López, "Cerium Oxides without U : The Role of Many-Electron Correlation", J. Phys. Chem. Lett. **12**, 6277–6283 (2021).

[124]E. Kroumova, J. M. Perez-Mato, and M. I. Aroyo, "WYCKSPLIT: A computer program for determination of the relations of Wyckoff positions for a group-subgroup pair", J Appl Crystallogr **31**, 646–646 (1998).

[125]M. I. Aroyo, J. M. Perez-Mato, D. Orobengoa, E. Tasci, G. De La Flor, and A. Kirov, "Crystallography online: Bilbao Crystallographic Server", Bulg. Chem. Commun. **43**, 183–197 (2011).

[126]H. J. Monkhorst and J. D. Pack, "Special points for Brillouin-zone integrations", Phys. Rev. B **13**, 5188–5192 (1976).

[127]F. Pascale, C. M. Zicovich-Wilson, F. López Gejo, B. Civalleri, R. Orlando, and R. Dovesi, "The calculation of the vibrational frequencies of crystalline compounds and its implementation in the CRYSTAL code: Crystalline Compounds and the CRYSTAL Code", J Comput Chem **25**, 888–897 (2004).

[128]C. M. Zicovich-Wilson, F. Pascale, C. Roetti, V. R. Saunders, R. Orlando, and R. Dovesi, "Calculation of the vibration frequencies of α-Quartz: The effect of Hamiltonian and basis set", J Comput Chem **25**, 1873–1881 (2004).

[129]M. Ferrero, M. Rérat, B. Kirtman, and R. Dovesi, "Calculation of first and second static hyperpolarizabilities of one- to three-dimensional periodic compounds. Implementation in the CRYSTAL code.", J Chem Phys **129**, 244110 (2008).

[130]M. Ferrero, M. Rérat, R. Orlando, and R. Dovesi, "The calculation of static polarizabilities of 1-3D periodic compounds. the implementation in the CRYSTAL code", J Comput Chem **29**, 1450–1459 (2008).

[131]M. Ferrero, M. Rérat, R. Orlando, and R. Dovesi, "Coupled perturbed Hartree-Fock for periodic systems: The role of symmetry and related computational aspects", J Chem Phys **128**, 014110 (2008).

[132]T. Bredow, K. Jug, and R. A. Evarestov, "Electronic and magnetic structure of $ScMnO_3$: Electronic and magnetic structure of $ScMnO_3$", Phys Status Solidi B **243**, R10–R12 (2006).

[133]J. Graciani, A. M. Márquez, J. J. Plata, Y. Ortega, N. C. Hernández, A. Meyer, C. M. Zicovich-Wilson, and J. F. Sanz, "Comparative Study on the Performance of Hybrid DFT Functionals in Highly Correlated Oxides: The Case of CeO_2 and Ce_2O_3", J. Chem. Theory Comput. **7**, 56–65 (2011).

[134]R. Evarestov, A. Panin, A. Bandura, and M. Losev, "Electronic structure of crystalline uranium nitrides UN, U_2N_3 and UN_2: LCAO calculations with the basis set optimization", in J. Phys. Conf. Ser. Vol. 117, 1 (2008), p. 012015.

[135]S. J. Duclos, Y. K. Vohra, A. L. Ruoff, A. Jayaraman, and G. P. Espinosa, "High-pressure x-ray diffraction study of CeO_2 to 70 GPa and pressure-induced phase transformation from the fluorite structure", Phys. Rev. B **38**, 7755–7758 (1988).

[136]L. Gerward, J. Staun Olsen, L. Petit, G. Vaitheeswaran, V. Kanchana, and A. Svane, "Bulk modulus of CeO_2 and PrO_2—An experimental and theoretical study", J. Alloys Compd. **400**, 56–61 (2005).

[137]M. Alaydrus, M. Sakaue, and H. Kasai, "A DFT+U study on the contribution of $4f$ electrons to oxygen vacancy formation and migration in Ln-doped CeO_2", Phys. Chem. Chem. Phys. **18**, 12938–12946 (2016).

[138]M. B. Kanoun, A. H. Reshak, N. Kanoun-Bouayed, and S. Goumri-Said, "Evidence of Coulomb correction and Spin–Orbit coupling in rare-earth dioxides CeO_2, PrO_2 and TbO_2: An ab initio study", J. Mag. Mag. Mater. **324**, 1397–1405 (2012).

[139]V. Kanchana, G. Vaitheeswaran, A. Svane, and A. Delin, "First-principles study of elastic properties of CeO_2 , ThO_2 and PoO_2", J. Phys.: Condens. Matter **18**, 9615–9624 (2006).

[140]T. Gürel and R. Eryiğit, "*Ab Initio* pressure-dependent vibrational and dielectric properties of CeO_2", Phys. Rev. B **74**, 014302 (2006).

[141]E. Wuilloud, B. Delley, W.-D. Schneider, and Y. Baer, "Spectroscopic Evidence for Localized and Extended f-Symmetry States in CeO_2", Phys. Rev. Lett. **53**, 202–205 (1984).

[142]A. Nakajima, A. Yoshihara, and M. Ishigame, "Defect-induced Raman spectra in doped CeO_2", Phys. Rev. B **50**, 13297–13307 (1994).

[143]E. Voloshina and B. Paulus, "Influence of electronic correlations on the ground-state properties of cerium dioxide", J Chem Phys **124**, 234711 (2006).

[144]Y. Wang, L. A. Zhang, S. Shang, Z.-K. Liu, and L.-Q. Chen, "Accurate calculations of phonon dispersion in CaF_2 and CeO_2", Phys Rev B **88**, 024304 (2013).

[145]N. I. Santha, M. T. Sebastian, P. Mohanan, N. M. Alford, K. Sarma, R. C. Pullar, S. Kamba, A. Pashkin, P. Samukhina, and J. Petzelt, "Effect of Doping on the Dielectric Properties of Cerium Oxide in the Microwave and Far-Infrared Frequency Range", J. Am. Ceram. Soc **87**, 1233–1237 (2004).

[146]S. Mochizuki, "Infrared optical properties of cerium dioxide", Phys. Stat. Sol. (b) **114**, 189–199 (1982).

[147]R. A. Evarestov, D. Gryaznov, M. Arrigoni, E. A. Kotomin, A. Chesnokov, and J. Maier, "Use of site symmetry in supercell models of defective crystals: Polarons in CeO_2", Phys. Chem. Chem. Phys. **19**, 8340–8348 (2017).

[148]D. Marrocchelli, S. R. Bishop, H. L. Tuller, G. W. Watson, and B. Yildiz, "Charge localization increases chemical expansion in cerium-based oxides", Phys. Chem. Chem. Phys. **14**, 12070 (2012).

[149]D. Marrocchelli, S. R. Bishop, H. L. Tuller, and B. Yildiz, "Understanding Chemical Expansion in Non-Stoichiometric Oxides: Ceria and Zirconia Case Studies", Adv. Funct. Mater. **22**, 1958–1965 (2012).

[150]P. A. Žguns, A. V. Ruban, and N. V. Skorodumova, "Phase diagram and oxygen-vacancy ordering in the CeO_2-Gd_2O_3 system: A theoretical study", Phys. Chem. Chem. Phys. **20**, 11805–11818 (2018).

[151]M. Balaguer, C.-Y. Yoo, H. J. M. Bouwmeester, and J. M. Serra, "Bulk transport and oxygen surface exchange of the mixed ionic-electronic conductor $Ce_{1-x}Tb_xO_{2-\delta}$ (x = 0.1, 0.2, 0.5)", J. Mater. Chem. A **1**, 10234–10242 (2013).

[152]F. Ye, T. Mori, D. R. Ou, J. Zou, G. Auchterlonie, and J. Drennan, "Compositional and valent state inhomogeneities and ordering of oxygen vacancies in terbium-doped ceria", J. Appl. Phys. **101**, 113528 (2007).

[153]F. Ye, T. Mori, D. R. Ou, M. Takahashi, J. Zou, and J. Drennan, "Compositional dependence of electrical conductivity of $Ce_{1-x}Tb_xO_{2-\delta}$ ($0 \leqslant x \leqslant 1$)", Renew. Energy **33**, 331–335 (2008).

[154]A. M. D'Angelo, A. C. Y. Liu, and A. L. Chaffee, "Oxygen Uptake of Tb–CeO_2: Analysis of Ce^{3+} and Oxygen Vacancies", J. Phys. Chem. C **120**, 14382–14389 (2016).

[155]D. Fuks, D. Gryaznov, E. Kotomin, A. Chesnokov, and J. Maier, "Dopant solubility in ceria: Alloy thermodynamics combined with the DFT+U calculations", Solid State Ion **325**, 258–264 (2018).

[156]A. G. Khachaturyan, *Theory of structural transformations in solids* (John Wiley & Sons, New York, Nov. 9, 1983), 574 pp.

[157]L. Shi, E. Vathonne, V. Oison, M. Freyss, and R. Hayn, "First-principles DFT+ U investigation of charged states of defects and fission gas atoms in CeO_2", Phys. Rev. B **94**, 115132 (2016).

[158]W. Tang, E. Sanville, and G. Henkelman, "A grid-based Bader analysis algorithm without lattice bias", J. Phys.: Condens. Matter **21**, 084204 (2009).

[159]M. Yu and D. R. Trinkle, "Accurate and efficient algorithm for Bader charge integration", J. Chem. Phys. **134**, 064111 (2011).

[160]A. Khachaturyan and B. Pokrovskii, "Concentration wave approach in structural and thermodynamic characterization of ceramic crystals", Prog Mater Sci **29**, 1–138 (1985).

[161]E. M. Lifshitz, "On the theory of phase transitions of the second order I.", J. Phys. (USSR) **VI**, 61–74 (1942).

[162]E. M. Lifshitz, "On the theory of phase transitions of the second order II.", J. Phys. (USSR) **VI**, 251–263 (1942).

[163]A. F. Jankowski and T. Tsakalakos, "Phase stability by the artificial concentration wave method", Metall Trans A **20**, 357–362 (1989).

[164]M. Finnis, A. Lozovoi, and A. Alavi, "The Oxidation of NiAl: What Can We Learn from Ab Initio Calculations?", Annu. Rev. Mater. **35**, 167–207 (2005).

[165]P. Linstrom, *NIST Chemistry WebBook, NIST Standard Reference Database 69* (National Institute of Standards and Technology, 1997).

[166]S. Grimme, J. Antony, S. Ehrlich, and H. Krieg, "A consistent and accurate ab initio parametrization of density functional dispersion correction (DFT-D) for the 94 elements H-Pu", J. Chem. Phys. **132**, 154104 (2010).

[167]E. Zintl, A. Harder, and B. Dauth, "Gitterstruktur der Oxyde, Sulfide, Selenide und Telluride des Lithiums, Natriums und Kaliums", Z. Elktrochem. Angew. P. **40**, 588–593 (1934).

[168]R. W. G. Wyckoff, "XXVII. Die Kristallstruktur von Silberphosphat und Silberarsenat (Ag_3XO_4)", Z. Kristallogr. Cryst. Mater. **62**, 529–539 (1925).

[169]M. C. Verbraeken, E. Suard, and J. T. S. Irvine, "Structural and electrical properties of calcium and strontium hydrides", J. Mater. Chem. **19**, 2766 (2009).

[170]R. W. G. Wyckoff, *Crystal Structures*, Second edition, Vol. 1 (Interscience Publishers, New York, 1963).

[171]J. A. Dean and N. A. Lange, eds., *Lange's handbook of chemistry*, 15. ed, McGraw-Hill Handbooks (McGraw-Hill, New York, NY, 1999), 1424 pp.

[172]W. Gerlach, "Die Gitterstruktur der Erdalkalioxyde", Z. Phys. **9**, 184–192 (1922).

[173]C. Artini, M. Pani, M. M. Carnasciali, M. T. Buscaglia, J. R. Plaisier, and G. A. Costa, "Structural Features of Sm- and Gd-Doped Ceria Studied by Synchrotron X-ray Diffraction and μ-Raman Spectroscopy", Inorg. Chem. **54**, 4126–4137 (2015).

[174]R. J. M. Konings, O. Beneš, A. Kovács, D. Manara, D. Sedmidubský, L. Gorokhov, V. S. Iorish, V. Yungman, E. Shenyavskaya, and E. Osina, "The Thermodynamic Properties of the f -Elements and their Compounds. Part 2. The Lanthanide and Actinide Oxides", J. Phys. Chem. Ref. Data **43**, 013101 (2014).

[175]P. Niggli, "Die Kristallstruktur einiger Oxyde I.", Z. Kristallogr. Krist. **57**, 253–299 (1922).

[176]P. W. Atkins and L. Jones, *Chemical principles: The quest for insight*, 2nd ed (W.H. Freeman, New York, 2002), 1024 pp.

[177]P. H. Wei, "Die Bindung im Quarz", Z. Kristallogr. Krist. **92**, 355–362 (1935).

[178]P. Villars and F. Hulliger, *TbO_2 Valence/Charge transfer: Datasheet from "PAULING FILE Multinaries Edition – 2012" in SpringerMaterials*, Springer-Verlag Berlin Heidelberg & Material Phases Data System (MPDS), Switzerland & National Institute for Materials Science (NIMS), Japan.

[179]L.-G. Liu, "High-pressure phase transformations of fluorite-type dioxides", Earth Planet. Sci. Lett. **49**, 166–172 (1980).

[180]D. M. Gruen, W. C. Koehler, and J. J. Katz, "Higher Oxides of the Lanthanide Elements. Terbium Dioxide[1]", Journal of the American Chemical Society **73**, 1475–1479 (1951).

[181]A. E. Curzon and H. G. Chlebek, "The observation of face centred cubic Gd, Tb, Dy, Ho, Er and Tm in the form of thin films and their oxidation", J Phys F: Met. Phys. **3**, 1–5 (1973).

[182]G. J. McCarthy, "Crystal data on *C*-type terbium sesquioxide (Tb_2O_3)", J Appl Crystallogr **4**, 399–400 (1971).

[183]N. C. Baenziger, H. A. Eick, H. S. Schuldt, and L. Eyring, "Terbium Oxides. III. X-Ray Diffraction Studies of Several Stable Phases", J. Am. Chem. Soc. **83**, 2219–2223 (1961).

[184]G.-y. Adachi and N. Imanaka, "The Binary Rare Earth Oxides", Chem. Rev. **98**, 1479–1514 (1998).

[185]L. Kaufman and H. Bernstein, *Computer Calculation of Phase Diagrams: With Special Reference to Refractory Metals*, Refractory Materials Monograph (Academic Press Inc, New York, May 1970), 334 pp.

[186]A. Chesnokov, D. Gryaznov, and E. Kotomin, "First principles calculations on CeO_2 doped with Tb^{3+} ions", Opt. Mater. **90**, 76–83 (2019).

[187]J. Malleshappa, H. Nagabhushana, S. Sharma, D. Sunitha, N. Dhananjaya, C. Shivakumara, and B. Nagabhushana, "Self-propagating combustion synthesis and luminescent properties of nanocrystalline CeO_2:Tb^{3+} (1–10mol%) phosphors", J. Alloys Compd. **590**, 131–139 (2014).

[188]Z. Wang, Z. Quan, and J. Lin, "Remarkable Changes in the Optical Properties of CeO_2 Nanocrystals Induced by Lanthanide Ions Doping", Inorg. Chem. **46**, 5237–5242 (2007).

[189]M. Zubkins, R. Kalendarev, J. Gabrusenoks, K. Smits, K. Kundzins, K. Vilnis, A. Azens, and J. Purans, "Raman, electron microscopy and electrical transport studies of x-Ray amorphous Zn-Ir-O thin films deposited by reactive DC magnetron sputtering", IOP Conf. Ser.: Mater. Sci. Eng. **77**, 012035 (2015).

[190]M. Zubkins, R. Kalendarev, J. Gabrusenoks, A. Plaude, A. Zitolo, A. Anspoks, K. Pudzs, K. Vilnis, A. Azens, and J. Purans, "Changes in structure and conduction type upon addition of Ir to ZnO thin films", Thin Solid Films **636**, 694–701 (2017).

[191]A. Chesnokov, D. Gryaznov, N. V. Skorodumova, E. A. Kotomin, A. Zitolo, M. Zubkins, A. Kuzmin, A. Anspoks, and J. Purans, "The local atomic structure and thermoelectric properties of Ir-doped ZnO: Hybrid DFT calculations and XAS experiments", J. Mater. Chem. C **9**, 4948–4960 (2021).

[192]Y. Ping, G. Galli, and W. A. Goddard, "Electronic Structure of IrO_2 : The Role of the Metal *d* Orbitals", J Phys Chem C **119**, 11570–11577 (2015).

[193]D. Gryaznov, E. Blokhin, A. Sorokine, E. A. Kotomin, R. A. Evarestov, A. Bussmann-Holder, and J. Maier, "A Comparative *Ab Initio* Thermodynamic Study of Oxygen Vacancies in ZnO and $SrTiO_3$: Emphasis on Phonon Contribution", J. Phys. Chem. C **117**, 13776–13784 (2013).

[194]D. Vilela Oliveira, J. Laun, M. F. Peintinger, and T. Bredow, "BSSE-correction scheme for consistent gaussian basis sets of double- and Triple-zeta valence with polarization quality for Solid-state calculations", J Comput Chem **40**, 2364–2376 (2019).

[195]S. Jantrasee, S. Pinitsoontorn, and P. Moontragoon, "First-Principles Study of the Electronic Structure and Thermoelectric Properties of Al-Doped ZnO", J Electron Mater **43**, 1689–1696 (2014).

[196]M. Peuckert, "XPS study on thermally and electrochemically prepared oxidic adlayers on iridium", Surf Sci **144**, 451–464 (1984).

[197]M. Hara, K. Asami, K. Hashimoto, and T. Masumoto, "An X-ray photoelectron spectroscopic study of electrocatalytic activity of platinum group metals for chlorine evolution", Electrochim Acta **28**, 1073–1081 (1983).

[198]W.-H. Chung, D.-S. Tsai, L.-J. Fan, Y.-W. Yang, and Y.-S. Huang, "Surface oxides of Ir(111) prepared by gas-phase oxygen atoms", Surf Sci **606**, 1965–1971 (2012).

[199]S.-i. Kan, S. Takemoto, K. Kaneko, I. Takahashi, M. Sugimoto, T. Shinohe, and S. Fujita, "Electrical properties of α-Ir_2O_3/α-Ga_2O_3 pn heterojunction diode and band alignment of the heterostructure", Appl Phys Lett **113**, 212104 (2018).

[200]S.-i. Kan, S. Takemoto, K. Kaneko, T. Shinohe, and S. Fujita, "Study on corundum-structured p-Type iridium oxide thin films and band alignment at iridium oxide /gallium oxide hetero-junction", in 2018 IEEE CPMT Symposium Japan (ICSJ) (Nov. 2018), pp. 95–98.

[201]H. Sowa and H. Ahsbahs, "High-pressure X-ray investigation of zincite ZnO single crystals using diamond anvils with an improved shape", J Appl Cryst **39**, 169–175 (2006).

[202]A. A. Bolzan, C. Fong, B. J. Kennedy, and C. J. Howard, "Structural Studies of Rutile-Type Metal Dioxides", Acta Crystallogr. Sect. B **53**, 373–380 (1997).

[203]T. Arikawa, Y. Takasu, Y. Murakami, K. Asakura, and Y. Iwasawa, "Characterization of the Structure of RuO_2-IrO_2/Ti Electrodes by EXAFS", J Phys Chem B **102**, 3736–3741 (1998).

[204]M.-S. Miao and R. Seshadri, "Rh_2O_3 versus IrO_2: Relativistic effects and the stability of Ir^{4+}", J Phys Condens Matter **24**, 215503 (2012).

[205]M. Dekkers, G. Rijnders, and D. H. A. Blank, "$ZnIr_2O_4$, a p-Type transparent oxide semiconductor in the class of spinel zinc-d^6-transition metal oxide", Appl. Phys. Lett. **90**, 021903 (2007).

[206]C. M. Bertoni, G. Cappellini, F. Finocchi, and P. Monachesi, "7.3.3 II-VI compound surfaces", in *Physics of Solid Surfaces*, Vol. 45A, edited by G. Chiarotti and P. Chiaradia, Landolt-Börnstein - Group III Condensed Matter (Springer Berlin Heidelberg, Berlin, Heidelberg, 2015), pp. 384–386.

[207]J. E. Morales-Mendoza, F. Paraguay-Delgado, J. D. Moller, G. Herrera-Pérez, and N. Pariona, "Structure and Optical Properties of ZnO and ZnO_2 Nanoparticles", J Nano R **56**, 49–62 (2019).

[208]W. Chen, Y. H. Lu, M. Wang, L. Kroner, H. Paul, H.-J. Fecht, J. Bednarcik, K. Stahl, Z. L. Zhang, U. Wiedwald, U. Kaiser, P. Ziemann, T. Kikegawa, C. D. Wu, and J. Z. Jiang, "Synthesis, Thermal Stability and Properties of ZnO_2 Nanoparticles", J Phys Chem C **113**, 1320–1324 (2009).

[209]A. Escobedo-Morales, R. Esparza, A. García-Ruiz, A. Aguilar, E. Rubio-Rosas, and R. Pérez, "Structural and vibrational properties of hydrothermally grown ZnO_2 nanoparticles", J Cryst Growth **316**, 37–41 (2011).

[210]M. G. Crestani, A. Steffen, A. M. Kenwright, A. S. Batsanov, J. A. K. Howard, and T. B. Marder, "Oxidative Addition of X-H (X = C, N, O) Bonds to $[Ir(PMe_3)_4]Cl$ and Catalytic Hydration of Acetonitrile Using its Peroxo Derivative, $[Ir(O_2)(PMe_3)_4]Cl$, as Catalyst Precursor", Organometallics **28**, 2904–2914 (2009).

[211]D. Bridget Williams, W. Kaminsky, J. M. Mayer, and K. I. Goldberg, "Reactions of iridium hydride pincer complexes with dioxygen: New dioxygen complexes and reversible O_2 binding", Chem. Commun., 4195 (2008).

[212]H. Baumgarth, T. Braun, B. Braun, R. Laubenstein, and R. Herrmann, "Synthesis of an Iridium Peroxido Complex and Its Reactivity Towards Brønsted Acids: Synthesis and Reactivity of an Iridium Peroxido Complex", Eur. J. Inorg. Chem. **2015**, 3157–3168 (2015).

[213]V. Pfeifer, T. E. Jones, J. J. Velasco Vélez, C. Massué, R. Arrigo, D. Teschner, F. Girgsdies, M. Scherzer, M. T. Greiner, J. Allan, M. Hashagen, G. Weinberg, S. Piccinin, M. Hävecker, A. Knop-Gericke, and R. Schlögl, "The electronic structure of iridium and its oxides: The electronic structure of iridium and its oxides", Surf Interface Anal. **48**, 261–273 (2016).

[214]Y. Liu, H. Masumoto, and T. Goto, "Electrical and Optical Properties of IrO_2 Thin Films Prepared by Laser-ablation", Mater. Trans. **45**, 3023–3027 (2004).

[215]W. D. Ryden, A. W. Lawson, and C. C. Sartain, "Electrical Transport Properties of IrO_2 and RuO_2", Phys Rev B **1**, 1494–1500 (1970).

[216]S. G. Bhat, A. M. Koshy, S. Pittala, and P. S. A. Kumar, "Tuning the growth of IrO_2 on $SrTiO_3$ (100) for spin-hall effect based oxide devices", in AIP Conf. Proc. Vol. 1859 (2017), p. 020007.

ACKNOWLEDGEMENTS

Having reached this milestone in my academic journey, I feel the need to express my gratitude to the numerous individuals, institutions, and organizations that have contributed their support and encouragement throughout my doctoral research.

First and foremost I would like to thank my supervisor Dr.rer.nat. Denis Grjaznov, who has guided and assisted me throughout the entire course of my doctoral research. Your mentorship has not only honed my scholarly skills but also instilled in me a passion for pushing the boundaries of knowledge.

My heartfelt appreciation extends to the members of the Laboratory of Kinetics in Self-Organizing Systems and the Laboratory of Computer Modeling of Electronic Structure of Solids at the Institute of Solid State Physics. I appreciate the leadership of Dr.habil.phys. Vladimir Kuzovkov, Dr.habil.phys. Eugene Kotomin, and Dr.rer.nat. Sergei Piskunov, who have maintained an atmosphere that fosters a collaborative spirit. Innovative insights that emerged from these environments have shaped my research experience.

I am thankful to all my colleagues, especially Dr.rer.nat. Yuri Mastrikov and Dr.phys. Alexander Platonenko, for their assistance in problem-solving. I am also thankful to people who have helped me bridge the gap between computational studies and experiments, most notably Dr.phys. Alexei Kuzmin of the EXAFS Spectroscopy laboratory, and Dr.habil.phys. Juris Purans of the Thin Films Laboratory.

I am thankful to grant agencies that support theoretical studies such as this one. In particular, I would like to thank projects, which have funded various parts of this work: Latvian Council of Science (projects LZP-2021/1-0203, and LZP-2018/1-0147), HPC-EUROPA3 initiative (project INFRAIA-2016-1-730897, with the support of the EC Research Innovation Action under the H2020 Programme), project 1.1.1.1/18/A/073 within the European Regional Development Fund, and European Council's Framework project EC 7FP GREEN-CC. Institute of Solid State Physics, University of Latvia as the Center of Excellence has received funding from the European Union's Horizon 2020 Framework Programme H2020-WIDESPREAD-01-2016-2017-TeamingPhase2 under grant agreement No. 739508, project CAMART^2.

I also want to thank the Faculty of Physics, Mathematics and Optometry of the University of Latvia for the support during studies and research. I am thankful for financial support from the University of Latvia Foundation: Arnis Riekstins's "MikroTik" donation and the project No. 8.2.2.0/20/I/006, "Strengthening of the capacity of doctoral studies at the University of Latvia within the framework of the new doctoral model", administrated by the University of Latvia Foundation.

None of this would be possible nor would ever come to fruition without the unwavering support of my family, friends, and loved ones. Your encouragement, understanding, and patience have been my pillars of strength throughout this arduous journey. I am forever thankful for each and every kind word and deed I have received over these years.